CIRCUMSTELLAR STRUCTURE PROPERTIES OF YOUNG STELLAR OBJECTS: ENVELOPES, BIPOLAR OUTFLOWS, AND DISKS

BY

WOOJIN KWON

DISSERTATION

Submitted in partial fulfillment of the requirements
for the degree of Doctor of Philosophy in Astronomy
in the Graduate College of the
University of Illinois at Urbana-Champaign, 2009

Urbana, Illinois

Doctoral Committee:

Associate Professor Leslie Looney, Chair
Professor Richard Crutcher
Professor Charles Gammie
Assistant Professor Benjamin McCall
Associate Professor Edmund Sutton

Abstract

Physical properties of the three main structures in young stellar objects (YSOs), envelopes, bipolar outflows, and circumstellar disks, have been studied using radio interferometers: the Berkeley-Illinois-Maryland Association (BIMA) array and the Combined Array for Research in Millimeter-wave Astronomy (CARMA).

(1) Envelopes: Three Class 0 YSOs (L1448 IRS 2, L1448 IRS 3, and L1157) have been observed by CARMA at $\lambda = 1.3$ mm and 2.7 mm continuum. Through visibility modeling to fit the two wavelength continuum data simultaneously, we found that the dust opacity spectral index β of Class 0 YSOs is around unity, which implies that dust grains have significantly grown already at the earliest stage. In addition, we discussed the radial dependence of β detected in L1448 IRS 3B and also estimated the density distribution of the three targets.

(2) Bipolar outflows: Polarimetric observations in the $\lambda = 1.3$ mm continuum and CO, as well as spectral line observations in ^{13}CO and C^{18}O have been carried out toward L1448 IRS 3, which has three Class 0 YSOs, using BIMA. We clearly identified two interacting bipolar outflows from the "binary system" of IRS 3A and 3B and estimated the velocity, inclination, and opening angle of the 3B bipolar outflow, using Bayesian inference. Also, we showed that the "binary system" can be bound gravitationally and we estimated the specific angular momentum, which is between those of binary stars and molecular cloud cores. In addition, we marginally detected linear polarizations at the center of IRS 3B (implying a toroidal magnetic field) in continuum and at the bipolar outflow region in CO.

(3) Circumstellar disks: We present the results of 6 objects (CI Tau, DL Tau, DO Tau, FT Tau, Haro 6-13, and HL Tau) in our T Tauri disk survey using CARMA. The data consist of $\lambda = 1.3$ mm and 2.7 mm continuum with an angular resolution up to $0.13''$. Through visibility modeling of two disk models (power-law disk with a Gaussian edge and viscous accretion disk) to fit the two wavelength data simultaneously in Bayesian inference, we constrained disk properties. In addition, we detected a dust lane at 100 AU radius of HL Tau, which is gravitationally unstable and can be fragmented. Besides, CI Tau and DL Tau appear to have a spiral pattern. Moreover, we found that more evolved disks have a shallower density gradient and that disks with a smaller β are less massive, which implies "hidden" masses in the cold midplane and/or in large grains. Finally, we found that the accretion disk model is preferred by HL Tau, which has a strong bipolar outflow and

accretion, while the power-law disk model is preferred by DL Tau, which has experienced dust settlement and has weak accretion. This implies that the accretion disk model could be applied to disks only in a limited age range.

To my family.

Acknowledgments

Finishing up this dissertation, it is a great pleasure to thank those who made this dissertation possible and who helped me increase my potential in the graduate program. First of all, I would like to thank Leslie Looney, my thesis adviser, for his dedicated guidance and support. He has never been too busy to give me comments on papers and proposals from the big picture to the detailed English expressions. He also encouraged me to try new ideas and enlarge my research area. In addition, the Thanksgiving dinner he hosted every year was wonderful and always fun. I also thank my dissertation committee for their insightful feedback: Richard Crutcher, Charles Gammie, Benjamin McCall, and Edmund Sutton. They were not just a dissertation committee, but also increased my potential. I am grateful to Richard Crutcher, as director of the Laboratory for Astronomical Imaging that is the Illinois group of the Combined Array for Research in Millimeter-wave Astronomy (CARMA), for supporting me to attend conferences and to carry out a relatively large project using CARMA. I thank Charles Gammie for his thoughtful discussion and comments not only for the dissertation but also other projects. I especially thank Benjamin McCall for introducing astrochemistry to me. Although this dissertation does not include much astrochemistry, the ability he brought to me will make my future research much richer. I thank Edmund Sutton for his discussion and sharp comments on the dissertation, particularly about Bayesian inference.

In addition to my dissertation committee, I would like to express my gratitude to Lee Mundy at the University of Maryland for his collaboration of multiple projects and contribution of CARMA observational time. Moreover, his insightful comments always made me think one more time deeper. I am also grateful to Jack Welch at the University of California at Berkeley for his collaboration of the disk project. I cannot skip to thank my office neighbor Lew Snyder. I have learned about endless passion toward research and nice personality from him. Also, he introduced Bourbon to me. I thank Athol Kemball for helpful comments and introduction of TeraGrid. The linux clusters of TeraGrid made the disk modeling feasible in a short time period. I would like to acknowledge Benjamin Wandelt for introducing Bayesian inference through a lecture. I admit that his introduction made me utilize Bayesian inference for my research. I am also grateful to Telemachos Mouschovias for his discussion and lectures on star formation.

It was wonderful to use CARMA for the studies. Without CARMA, I could not have

obtained these nice results. For the successful usage of CARMA and enjoyable and learnable frequent trips to CARMA, I am grateful to many people (CARMA staff and observers) including but not limited to: Dave Woody, James Lamb, Nikolaus Volgenau, John Carpenter, Jenny Patience, Dick Plambeck, etc. In addition, I would like to thank Mel Wright and Peter Teuben for their support and help to resolve MIRIAD issues. I also express my gratitude to Tony Wong and Douglas Friedel for helpful discussions about data reduction locally. Additionally, I thank Douglas Friedel for helping me quickly resolve various issues I have faced while writing programs and the dissertation.

I have been spending a great time here at Urbana in terms of life as well as study. It was possible due to nice colleagues. I am grateful to all the colleagues here including too-many-to-mention students, postdocs, faculty, and staff.

Finally, I would like to deeply thank my family for their steady support. In particular, this dissertation would not have been possible without my lovely wife, Kijeong Yim, who has been always next to me, supporting and encouraging me. I believe that my 10-day old daughter, Dyne Kwon, also helped and encouraged me to finish up all these things, waiting for more two weeks inside mom.

Table of Contents

List of Tables

List of Figures

1 Introduction

1.1 Circumstellar Structures of Protostars

Why are we here? Although all fields of astronomy (also other natural sciences and philosophy) contribute to address this question, everyone may agree that an understanding of star and planet formation is a main pillar for the answer. In a simple argument, stars are the unique sources of heavy atoms such as carbon, oxygen, nitrogen, etc., which are essential for living creatures, as well as the energy source for their existence. On the other hand, planets are the "ground" on which life emerges.

Stars form in molecular clouds by gravitational collapse. In the large picture of star formation that astronomers have drawn in the past few decades (e.g., McKee & Ostriker, 2007), once a protostar forms by gravitational collapse (dynamical contraction) at the center of a molecular cloud core, the protostellar system (often called a young stellar object, YSO) evolves, actively interacting with its environments. Dust and gas are inflowing from the prenatal molecular core (envelope) to the central protostar and outflowing to the interstellar medium (molecular cloud) through an energetic bipolar outflow/jet, which carries out angular momentum of the accreting material. In addition, presumably an accretion disk is also formed around a protostar at the earliest stage. As the protostellar system evolves, the envelope is dispersed by the bipolar outflow and/or accreted onto the central protostar. Finally, the circumstellar disk is left over, which likely forms a planetary system. These three structures: envelopes, bipolar outflows, and disks, are at the center of YSO evolution, i.e., star and planet formation. Thus, in this dissertation, the three circumstellar structures are investigated for a better understanding of star and planet formation. For example, envelopes can reveal the initial conditions of how stars form and circumstellar disks expose the conditions for planet formation.

Although we have a good, overall picture of star formation, the details are still under debate. For example, one of the key issues is the role of magnetic fields in star formation. Models on one side pose relatively strong magnetic fields to support molecular clouds from collapsing in a short time scale (e.g., a free-fall time scale) and so to control star formation (e.g., Mouschovias, 1991), while models on the other side propose that magnetic fields are negligible and instead turbulence plays the key role (e.g., Hartmann et al., 2001). In the former models, while charged particles (electrons, ions, and charged grains) are frozen

on magnetic fields, neutral particles move inward by gravity: ambipolar diffusion. The neutrals are partially affected by magnetic field pressure through collision with charged particles. When the central dense core overcomes the magnetic pressure by accumulating mass through ambipolar diffusion (mass-to-field flux ratio increases above the critical value), it dynamically contracts to form a protostar. During this phase, magnetic fields are dragged inward and have an hourglass morphology. In addition, molecular clouds are flattened during ambipolar diffusion, since moving along the magnetic field direction is easier due to the lack of magnetic field tension. As a result, the strong magnetic field models predict an hourglass morphology of magnetic fields perpendicular to the elongated cloud structure and the magnetic field strength proportional to the square root of density, $\rho^{1/2}$. In contrast, in the viewpoint of weak magnetic field models the morphology of magnetic fields is rather random and the strength is proportional to $\rho^{2/3}$ due to spherical contraction. Many observational studies have been tackling this problem, but a clear answer has not yet been found. For example, while the hourglass morphology of magnetic fields perpendicular to an elongated cloud has been detected (Girart et al., 2006) supporting the strong magnetic field models, recent observations to test the mass-to-flux ratio increase reported results against the "idealized" ambipolar diffusion model (Crutcher et al., 2009).

Magnetic field morphology and strength would be direct observables to constrain star formation models, but there are other properties of envelopes available for the purpose, such as the velocity field and density distribution. In addition, envelopes may also have other effects induced by magnetic fields such as dust segregation. Therefore, studying envelope properties is a reliable means to have insights about star formation.

Similarly, the properties of circumstellar disks will provide the initial conditions to form planets. For example, density and temperature distributions of circumstellar disks provide a means to examine whether planets can be formed by gravitational instability. If disks have a region gravitationally unstable and/or some structures induced by gravitational instability (e.g., a spiral pattern) are detected, planets can form in the region. In addition, dust grain properties will provide insights about the possibility of terrestrial planet formation. Accretion mechanism is also a key to understand planet formation in the basis of circumstellar disk evolution.

Earlier, YSOs have been classified depending on their spectral energy distribution (SED) index at $\lambda = 2$–10 μm (Lada & Wilking, 1984) and later the wavelength regime was extended to 25 μm by by the Infrared Astronomical Satellite (IRAS). By assigning evolutionary stages (Adams et al., 1987) and adding a new younger class (Andre et al., 1993) to the classification scheme, YSOs are finally summarized in four distinct classes (e.g. Andre & Montmerle, 1994). Class 0 YSOs have more massive envelopes than their central objects, and are thought to be newly formed protostars. In addition, they have well-developed bipolar outflows. They were considered to be invisible at $\lambda < 10$ μm but Spitzer Space Telescope

(SST) showed that scattered light on the bipolar outflow cavity can be detected even at short wavelengths (e.g., Tobin et al., 2007), which indicates that the near infrared emission largely depends on the inclination of bipolar outflows. Class I YSOs are characterized by $\alpha(\equiv d\log(\nu F_\nu)/d\log\nu) < 0$ at $\lambda = 2 - 25$ μm. At this stage, the bipolar outflows are dispersing the envelopes and accretion is diminishing. Class II YSOs have $0 < \alpha < 2$ at $\lambda = 2 - 25$ μm and they are visible at optical wavelengths with an infrared excess mainly due to optically thick circumstellar disks. YSOs of this stage are also called classical T Tauri stars (CTTs) (in the case of low mass systems) or Herbig Ae/Be stars (in the case of intermediate mass systems). Finally, Class III YSOs have $\alpha > 2$ at $\lambda = 2 - 25$ μm: a weak infrared excess due to the small amount of residual circumstellar material. This stage is right before the main sequence and the YSOs are also called weak-lined T Tauri stars (WTTs).

It is noteworthy that the classification has been supported by observational results to estimate the physical properties. For example, through optical and infrared photometry of YSOs in the Taurus-Auriga molecular cloud, Kenyon & Hartmann (1995) found that envelope emission decreases from Class I to Class II and accretion rate decreases from Class II to Class III. On the other hand, opening angle increases of bipolar outflows, suggesting envelope material dispersed by bipolar outflows and/or accreted onto protostellar disks, have been reported by molecular bipolar outflow observations (e.g., Arce & Sargent, 2006) and SST IRAC observations (Seale & Looney, 2008).

We employ this notation of Class 0–III. Note that the youngest YSOs and earliest protostellar systems indicate Class 0 YSOs. On the other hand, the circumstellar disks of Class II YSOs are also called T Tauri disks or protoplanetary disks depending on the main viewpoint of the structure.

In this dissertation, physical properties of circumstellar structures of YSOs such as envelopes, bipolar outflows, and disks are discussed using targets of nearby star formation regions. Following the evolutionary stages of YSOs, envelopes are studied first (Chapter 2). Density distribution and dust opacity spectral index of envelopes are focused on in order to address star formation theories and dust properties in three targets: L1448 IRS 2, L1448 IRS 3, and L1157. In Chapter 3, bipolar outflows of L1448 IRS 3 are presented with polarimetric observations to tackle the relationship between magnetic fields and the bipolar outflow, as well as to study the bipolar outflow properties. Finally, physical properties of circumstellar disks of T Tauri stars (Class II) are studied in Chapter 4 focusing on the physical properties such as density distribution, grain growth, disk mass, disk size, etc., toward 6 T Tauri disks in the Taurus molecular cloud (CI Tau, DL Tau, DO Tau, FT Tau, Haro 6-13, and HL Tau). Correlations between the physical properties and a protoplanet feature detected in HL Tau are also discussed. Conclusions of individual chapters are summarized and emphasized at the end (Chapter 5). In addition to the science results, radio interferometry and Bayesian

inference are briefly introduced beforehand, in Sections 1.2 and 1.3 of this chapter.

1.2 Interferometer and CARMA

The studies of this dissertation have been carried out with observational data taken by radio interferometers at millimeter wavelengths. In this section, we briefly introduce principles of radio interferometry (e.g., Rohlfs & Wilson, 2004; Thompson et al., 2001; Taylor et al., 1999).

Radio interferometers measure coherence of electromagnetic waves received by multiple antennas from a distant celestial source. For simplicity, consider a two-antenna interferometer. When orienting to a target off zenith, the electromagnetic wave arrives at the two antennas with a delay of τ_g, which stands for the geometrical delay,

$$\tau_g = \mathbf{b} \cdot \mathbf{s}/c, \tag{1.1}$$

where $\mathbf{b}$ is the baseline vector of the two antennas, $\mathbf{s}$ is the unit vector to the target, and c is the speed of light. Therefore, the induced voltages of the two antennas proportional to the electromagnetic wave are expressed as,

$$\begin{aligned} V_1(t) &\propto E_1(t) = Ee^{i\omega t} \\ V_2(t) &\propto E_2(t) = Ee^{i\omega(t-\tau_g)}. \end{aligned}$$

These voltages are multiplied and time-averaged in a correlator, so the output of the correlator is

$$\langle V_1(t)V_2(t)\rangle \propto \frac{1}{2}E^2 e^{i\omega\tau}. \tag{1.2}$$

The $\langle\ \rangle$ expresses a time average. Note that a total delay (τ) appears, since an additional instrumental delay (τ_i) can be introduced: $\tau = \tau_g - \tau_i$. Therefore, the output signal of the correlator presents an interference pattern over the sky depending on the geometrical delay, when the instrumental delay is fixed.

The power received by each antenna in a bandwidth $\Delta\nu$ from a source element $d\Omega$ is $A(\mathbf{s})I(\mathbf{s})\Delta\nu d\Omega$, when $I(\mathbf{s})$ and $A(\mathbf{s})$ are the radio brightness of the sky and the effective collecting area of antennas in the direction $\mathbf{s}$, respectively. It is assumed that antennas have the same effective collecting area. Therefore, in the case of interferometry, the output of the correlator is given by

$$P_{12} = \Delta\nu \int_S A(\mathbf{s})I(\mathbf{s})e^{i\omega\tau} d\Omega. \tag{1.3}$$

This equation can be expressed in terms of the baseline and the target position vector instead of the geometrical delay. In addition, the target position vector can be substituted

with the phase center vector ($\mathbf{s_0}$) and a displacement vector (σ) normal to the phase center vector, $\mathbf{s} = \mathbf{s_0} + \sigma$:

$$\begin{aligned} P_{12} &= \Delta\nu \int_S A(\mathbf{s}) I(\mathbf{s}) \exp\Big[i\omega\Big(\frac{\mathbf{b}\cdot\mathbf{s}}{c} - \tau_i\Big)\Big] d\Omega \\ &= \Delta\nu \exp\Big[i\omega\Big(\frac{\mathbf{b}\cdot\mathbf{s_0}}{c} - \tau_i\Big)\Big] \int_S A(\mathbf{s}) I(\mathbf{s}) \exp\Big[i\omega\frac{\mathbf{b}\cdot\sigma}{c}\Big] d\Omega. \end{aligned} \tag{1.4}$$

If we set the instrumental delay to the geometrical delay toward the phase center, then we have

$$\begin{aligned} P_{12} &= \Delta\nu \int_S A(\mathbf{s}) I(\mathbf{s}) \exp\Big[i\omega\frac{\mathbf{b}\cdot\sigma}{c}\Big] d\Omega \\ &= V(\mathbf{b}) A_0 \Delta\nu, \end{aligned} \tag{1.5}$$

where $V(\mathbf{b}) \equiv \int_S A_N(\mathbf{s}) I(\mathbf{s}) \exp[i\omega\mathbf{b}\cdot\sigma/c]$, the so-called visibility. Here A_N is the normalized antenna reception pattern, $A(\mathbf{s})/A_0$. Note that what we want is to obtain the sky brightness distribution $I(\mathbf{s})$ from the detected power. Therefore, the visibility has all the information we need.

In practice, we set a coordinate system to describe the baseline vector in units of the observational wavelength:

$$\omega\frac{\mathbf{b}}{c} = 2\pi\nu\frac{\mathbf{b}}{c} = 2\pi(u, v, w). \tag{1.6}$$

The coordinate system is oriented so that w is toward (parallel to) the phase center $\mathbf{s_0}$, u is toward east, and v is toward north. Note that $\sqrt{u^2+v^2}$ indicates the projected uv distance seen from the target. On the other hand, for the target position we employ direction cosines (l, m, n) of $\mathbf{s}$ with respect to (u, v, w). Therefore, using

$$d\Omega = \frac{dldm}{\sqrt{1-l^2-m^2}},$$

we have the visibility as:

$$V(u, v, w) = \int\int \Big[\frac{A_N(l, m) I(l, m)}{\sqrt{1-l^2-m^2}}\Big] e^{2\pi i(ul+vm+w\sqrt{1-l^2-m^2})} dldm. \tag{1.7}$$

Generally observations (i.e., antenna response patterns) are limited to a small region nearby the phase center, so $\sqrt{1-l^2-m^2} \approx 1$. Thus, we can obtain a simpler form:

$$V(u, v, w) e^{-2\pi w} \approx V(u, v) = \int\int \Big[\frac{A_N(l, m) I(l, m)}{\sqrt{1-l^2-m^2}}\Big] e^{2\pi i(ul+vm)} dldm. \tag{1.8}$$

The $V(u, v)$ is a visibility function on uv plane, which is the $w = 0$ plane. Note that this equation expresses a two-dimensional Fourier transform relation between the visibility

$V(u,v)$ and the function in the brackets. Applying the assumption $\sqrt{1-l^2-m^2} \approx 1$ further, simply we can see the Fourier transform relation (denoted by $\rightleftarrows$) as

$$V(u,v) \rightleftarrows A_N(l,m)I(l,m). \tag{1.9}$$

From the Fourier transform relation, u and v are "spatial frequencies", since l and m are values in a spatial coordinate system. It means that larger (u, v) values correspond to small scales in space.

Again, the purpose is to estimate the sky intensity distribution $I(l,m)$ from the observed visibility $V(u,v)$. If we would obtain visibilities in the whole uv space, then the intensity field would be achieved simply by inverse Fourier transform of the visibilities and division of the antenna response pattern. However, in practice we can just obtain a sample $S(u,v)$ of visibilities in a limited uv coverage. So, based on the convolution theorem, the practical relation is:

$$\begin{aligned} S(u,v)V(u,v) &\rightleftarrows FT^{-1}[S(u,v)] * FT^{-1}[V(u,v)] \\ S(u,v)V(u,v) &\rightleftarrows B_D(l,m) * [A_N(l,m)I(l,m)]. \end{aligned} \tag{1.10}$$

$FT^{-1}[f]$ represents the inverse Fourier transform of a function f and $*$ indicates convolution. Thus a deconvolution is involved in the data reduction of interferometric observations, which can cause a bias due to its non-linearity. Additionally, as the intensity is a real quantity, the visibility should be Hermitian, which means that $V(-u,-v) = V^*(u,v)$. Therefore, an observational visibility point is actually two data points in uv space mathematically.

The expression 1.10 clearly shows the procedures of visibility modeling as well as data reduction. Data reduction, from sampled visibilities to intensity distribution, includes inverse Fourier transform of the visibility data, deconvolution by the inverse Fourier transform of the sampling function (so-called dirty beam), and finally correction of the antenna response pattern (so-called the primary beam). On the other hand, visibility modeling, which compares data with models in the uv space, includes construction of a model image, correction of the primary beam, Fourier transform, and finally sampling along the observational uv coverage. The modeling we carry out in the studies for envelopes of Chapter 2 and for circumstellar disks of Chapter 4 follows the procedures. Visibility modeling is more reliable than image modeling (comparing a model with interferometric data in the image space), as it avoids the non-linear convolution step.

The main interferometer we use is the Combined Array for Research in Millimeter-wave Astronomy (CARMA), which is located in eastern California at an altitude of about 2200 m. As it is the first heterogeneous array (excluding long baseline interferometers), it consists of six 10.4-m, nine 6.1-m, and eight 3.5-m antennas, in total 23 antennas. This heterogeneity requires special care for modeling of CARMA data. Since all antennas are not the same, we

cannot use an identical antenna primary beam for all visibilities. Instead, as the antenna response pattern $A(\mathbf{s})$ is substituted with $\sqrt{A_1(\mathbf{s})A_2(\mathbf{s})}$, we need model images corrected by various primary beams. For example, three different combined-primary beams need to be considered for an array having two kinds of antennas. More introduction to CARMA will be found in Chapter 2 and 4. In particular, special features in the most compact E configuration and in the most extended A and B configurations are addressed in Chapter 2 and 4, respectively.

1.3 Bayesian Inference

We employ Bayesian inference for modeling, rather than the widely used least χ^2 method. Bayesian inference has been used in various fields of astronomy, e.g., imaging (Sutton & Wandelt, 2006) as well as modeling. This section is dedicated to introduce Bayesian inference, based mainly on MacKay (2003) and Gilks et al. (1996). In the frequentist's (non-Bayesian) point of view, it is examined how well a hypothesis (a given model) can produce the observables (data) with random effects. Probability is not allowed to describe inference but random variables. On the other hand, in the Bayesian point of view, it is of interest to obtain probabilities of model parameters based on assumptions (e.g., prior information, known noises etc.). In addition, Bayesians feel free to use the probabilities for describing inferences.

Bayes' theorem can be obtained from the product rule of probability theory:

$$P(m, D \mid H) = P(m \mid D, H)P(D \mid H) = P(D \mid m, H)P(m \mid H). \tag{1.11}$$

$P(x \mid y)$ indicates conditional probability of x on y and $P(x, y)$ presents joint probability. Here m, D, and H are model parameter sets, data, and hypothesis (i.e., a given model), respectively. It is noteworthy that m is used to denote *model parameter sets*, while H represents *a hypothesis model*. Therefore, all three sides of the equation describe the probability of m (the model is true) and D (the data are observed) given H (the hypothesis). From the middle and the right-hand sides of Equation 1.11, Bayes' theorem is expressed as:

$$P(m \mid D, H) = \frac{P(D \mid m, H)P(m \mid H)}{P(D \mid H)}. \tag{1.12}$$

Here $P(m \mid D, H)$ is called the posterior probability, $P(D \mid m, H)$ the likelihood, $P(m \mid H)$ the prior, and $P(D \mid H)$ the evidence. The evidence is also called the marginal likelihood, since $P(D \mid H) = \int dm P(D \mid m, H)P(m \mid H) \approx \Sigma\ P(D \mid m, H)P(m \mid H)$. This equation can be simplified, when only relative probabilities of model parameters are concerned within

a hypothesis:

$$P(m \mid D) = \frac{P(D \mid m)P(m)}{P(D)}. \tag{1.13}$$

Note that the denominator $P(D)$ acts just as a normalization factor in this case. The modeling of envelopes in Chapter 2 and of a bipolar outflow in Chapter 3 use this simple case. In the envelope studies, we assume a model with, for example its density distribution following a power law and temperature distribution in radiative equilibrium with the central radiation source, and we attempt to find the posterior probability distributions of the model parameters. Similarly, in the bipolar outflow studies, a specific geometry (a model) is assumed and the posterior probability distributions of the model parameters are searched.

On the other hand, the circumstellar disk studies in Chapter 4 are the case of Equation 1.12, as we consider two models: power law disk (H_1) and viscous accretion disk (H_2). Bayesian inferences also provide a pathway to compare models in such multiple model tests. The model comparison is done by the evidences, which are the integrations of likelihood times prior over the parameter space, as mentioned before. The evidence can also be approximated by the best-fit likelihood times the Occam factor, e.g., simply in the one dimensional case:

$$\begin{aligned} P(D \mid H_1) &= \int dm P(D \mid m, H_1) P(m \mid H_1) \\ &\approx P(D \mid m_{best}, H_1) \sigma_{m|D} P(m_{best} \mid H_1), \end{aligned} \tag{1.14}$$

where $\sigma_{m|D} P(m_{best} \mid H_1)$ is the Occam factor, which is equal to the ratio of the posterior accessible volume ($\sigma_{m|D}$) to the prior accessible volume (σ_m), since $P(m_{best} \mid H_1) = 1/\sigma_m$. Note that a sophisticated model with more parameters has a penalty in the Occam factor, so a better fit done by a more sophisticated model does not necessarily mean that the sophisticated model is better. Uniform priors in identical volumes are used in the disk model comparison for simplicity, so integrations of likelihood are compared.

For the Bayesian inference, the posterior needs to be calculated over the "whole" model parameter space. The key is how we can sample parameter sets to estimate the posterior probability distribution. Markov chain Monte Carlo (MCMC) methods offer a good, feasible way. MCMC samplings can start with either a randomly or intentionally chosen parameter set m_0. The next parameter set m_1 is drawn by a distribution $P(m_1 \mid m_0)$, which depends on only the current parameter set m_0. Generally, a new state m_{i+1} is selected by the probability $P(m_{i+1} \mid m_i)$ depending on only the current state m_i. This sampling chain is called the Markov chain (e.g., Gilks et al., 1996). As it goes, the chain gradually "forgets" the initial parameter set and converges to a unique stationary distribution. After throwing away the pre-converging sample (so-called "burning"), a new sample may be collected from the last parameter set of the pre-converging sample. This fresh sample can be used to

estimate the posterior probability distributions.

The Metropolis-Hastings algorithm provides an easy way to construct such a Markov chain. At a state m_i, a candidate of the next state m_{i+1} is drawn with a proposal distribution, which depends on the current state m_i, i.e., $Q(. \mid m_i)$. For example, a normal distribution with its mean of the current state m_i and a fixed standard deviation can be a proposal distribution. The candidate of m_{i+1} is accepted at a rate,

$$\alpha(m_i, m_{i+1}) = \min\Big[1, \frac{P(m_{i+1})\, Q(m_i \mid m_{i+1})}{P(m_i)\, Q(m_{i+1} \mid m_i)}\Big]. \tag{1.15}$$

Note that any functional form is possible for the proposals. In particular, when a symmetric function is used for the proposal distribution, the acceptance rate is simply described as $\min[1, P(m_{i+1})/P(m_i)]$ and this special case is also called the Metropolis method. Regardless of the proposal functional forms, the distribution of the sample drawn by a stationary proposal distribution provides the posterior distribution of parameters, after converging. The studies of bipolar outflows in Chapter 3 and circumstellar disks in Chapter 4 utilize the Metropolis-Hastings algorithm, while the envelope studies obtain the distribution of parameters by estimating the likelihood in a parameter grid space.

Multiple parameters are used for the modelings of this dissertation: 5 parameters for bipolar outflow studies and 8 parameters for circumstellar disk studies. To deal with the multi-dimensional parameter space, Gibbs sampling is employed. Individual parameters are drawn based on the Metropolis-Hastings algorithm one by one, with the other parameters fixed: the Gibbs sampling.

For circumstellar disk studies, a couple of techniques to improve the efficiency of MCMC are also adopted: annealing and multiple runs. The simulated annealing is one of techniques accelerating convergence; others are Hamiltonian Monte Carlo, overrelaxation, and so on. The idea of simulated annealing is to use more "mobile" proposal distributions (e.g., Gaussian function with a broader standard deviation). In order words, a more energetic (higher temperature) "ball" moves in the parameter space at the beginning and the ball temperature decreases down to a specified level. For example, we use $\sigma' = \sigma/f_a$ with an annealing factor $f_a = 0.1 + 0.005i$ for the circumstellar disk modelings. The annealing technique improves the convergence speed and help avoid being stuck in a local minimum. Note that the annealing should be limited in the burning-in stage (before converging), because the sample to be used for estimating posterior distributions of parameters should be obtained by a stationary proposal distribution with a fixed σ (e.g., Gilks et al., 1996).

In addition to the annealing, we improve the efficiency of MCMC by running multiple runs. It is one of the issues being still debated; which strategies are better: a long chain, a small number of intermediate chains, or many short chains (e.g., MacKay, 2003; Gilks et al., 1996). To use computer resources of the TeraGrid Linux clusters wisely as well as to

improve the convergence of MCMC, we run multiple chains with randomly generated initial parameters. After checking convergence by comparing the results of the multiple runs, we obtain a long chain to estimate the parameter posterior distributions.

2 Envelopes

This chapter was published in Kwon et al. (2009).

2.1 Introduction

Although dust grains are only about one hundredth of the interstellar medium by mass, they play crucial roles for star formation, planet formation, and furthermore the origin of life. They are essential places to form and store molecules, and they are the main ingredient to form terrestrial planets, as well as playing a role in the heating and cooling mechanisms during star and planet formation.

The dust opacity[1] spectral index (β) is related to dust properties. It depends on dust grain sizes, compositions, and shapes (e.g., Pollack et al., 1994; Draine, 2006). In particular, it is largely sensitive to grain sizes; larger grains give smaller β (e.g., Draine, 2006). Many observational studies at infrared and millimeter wavelengths toward T Tauri circumstellar disks have reported smaller values of β (~ 1.0) (e.g., Andrews & Williams, 2007) compared to that of the interstellar medium (~ 1.7) (Finkbeiner et al., 1999; Li & Draine, 2001). In the sense that dust grains may develop terrestrial planets, it is very encouraging to see signatures of larger dust grains in T Tauri disks, evolved young stellar objects (YSOs), compared to grains in the interstellar medium.

However, it is not clear when the dust grain growth responsible for the opacity spectral index $\beta \sim 1$ mainly occurs. For example, while Andrews & Williams (2005) reported grain growth along the YSO evolution from Class I to Class II, using spectral energy distributions over $\lambda = 1.3$ mm and submillimeter data, Natta et al. (2007) did not find such a tendency (a systematic variation of β). To distinguish when dust grains mainly grow up to the sizes for $\beta \sim 1$, Class 0 YSOs are the best targets to examine. Class 0 YSOs are at the starting point of low-mass star formation and they are well defined. They have more massive envelopes than or comparably massive envelopes to their central compact objects (e.g., Andre et al., 1993). They are also characterized with well-developed bipolar outflows. Earlier stages such as starless cores might be another good target but they are hardly confined. Their physical conditions including age have a much larger scatter than Class 0 sources. In addition, they are not all expected to form stars.

[1]Dust "emissivity" has also been used in literatures from the viewpoint of dust thermal "emission".

In fact, no definitive answer has been given to the opacity spectral index β of Class 0 sources so far. It is another reason that this study is needed beyond the grain growth point of view. There are some previous studies about the flux density spectral indexes of Class 0 sources, which are related to the dust opacity spectral indexes, although they have not focused on dust properties (e.g., Hogerheijde & Sandell, 2000; Shirley et al., 2000). However, these studies used submillimeter to 1.3 mm wavelengths, which is near the range of peak intensities at envelope temperatures ($\sim$ 30 K), so the Rayleigh-Jeans approximation is invalid. In that case, the estimate of β is sensitive to the envelope temperature, which causes relatively large uncertainties in the β estimate. In addition, optical thickness can cause another uncertainty, since Class 0 YSO envelopes can be optically thick at submillimeter wavelengths. On the other hand, Harvey et al. (2003) obtained $\beta \sim 0.8$ toward the Class 0 YSO B335 using $\lambda = 1.2$ mm and 3 mm interferometric data, while carrying out modeling to test density distribution models of star formation. However, they did not have a good data set with comparable *uv* coverage at both wavelengths to discuss the β in detail. In other words, there are no reliable β estimates of Class 0 YSOs. As a result, many studies to estimate masses from spectral energy distributions (SEDs) and/or to constrain density distributions have assumed $\beta \sim 1$ (e.g., Looney et al., 2003) or considered a possible range of β (e.g., $\beta = 1 - 2$, Chandler & Richer, 2000).

Radio interferometry at millimeter wavelengths is the best means to investigate the β of Class 0 YSOs. As mentioned, optical thickness and dust temperature issues cause large uncertainties at shorter wavelengths. On the other hand, contamination of non-thermal continuum increases with wavelength, so it is not negligible at longer centimeter wavelengths. In addition, considering envelope sizes of Class 0 YSOs and their environments (normally they are within extended molecular clouds), single dish observations are not appropriate due to their lack of angular resolution and the contamination of molecular clouds. In contrast, interferometers provide high angular resolution and resolve out the emission from the large-scale molecular cloud. However, they may also resolve out emission from the Class 0 envelopes. This is caused by limited *uv* coverage, particularly due to the absence of short baselines and zero-spacing. For these reasons, interferometers with good *uv* coverage are required. The recently commissioned Combined Array for Research in Millimeter-wave Astronomy (CARMA) provides the best opportunity with its unprecedented compact configuration and image fidelity (Woody et al., 2004).

In this chapter, we present dust opacity spectral indexes β of Class 0 sources (L1448 IRS 2, L1448 IRS 3, and L1157) in order to tackle when the dust grain growth responsible for $\beta \sim 1$ mainly occurs: before or after the Class 0 stage. We do a parametric modeling in *uv* space to address the β values, as well as image and visibility comparisons. In addition, we examine power-law density indexes via modeling. First, we discuss our observations and data reduction, focusing on how well our CARMA data incorporate with this study.

Afterward, we show our results in images, *uv* visibilities, and visibility modelings. At the end, we discuss the implications of our results.

2.2 Target YSOs

We have carried out observations of three Class 0 YSO regions (L1448 IRS 2, L1448 IRS 3, and L1157) using CARMA in the $\lambda = 1.3$ mm and 2.7 mm continuum. These three targets are well defined as Class 0 YSOs by previous studies (e.g., Shirley et al., 2000; O'Linger et al., 1999). L1448 IRS 2 and IRS 3 are located in the dark cloud L1448 of the Perseus molecular cloud complex at a distance of 250 pc. They were first revealed by IRAS observations (Bachiller & Cernicharo, 1986). L1448 IRS 3 is the brightest infrared source in the dark cloud and has three Class 0 sources (3A, 3B, and 3C), revealed by radio interferometric observations (Curiel et al., 1990; Terebey & Padgett, 1997; Looney et al., 2000). Kwon et al. (2006) also studied the binary system of 3A and 3B, the two interacting bipolar outflows, and the magnetic field in the region, using polarimetric observations of the Berkeley Illinois Maryland Association (BIMA) array in the $\lambda = 1.3$ mm continuum and CO $J = 2 \rightarrow 1$ transition line.

On the other hand, L1448 IRS 2 at $\sim 3'$ west of IRS 3 has not been focused on very much due to its weaker brightness. However, O'Linger et al. (1999) identified it as a Class 0 YSO, using far-infrared up to millimeter continuum observations. In addition, recent deep Spitzer Space Telescope (SST) IRAC observations have shown a large bipolar outflow spanning over $5'$ (Tobin et al., 2007). CARMA observations in CO $J = 2 \rightarrow 1$ and $J = 1 \rightarrow 0$ transitions also show a well-developed bipolar outflow (Kwon et al. in preparation).

L1157 is a dark cloud in Cepheus. The distance is not well known but it is arguably about 250 pc (Looney et al., 2007). Its envelope and large bipolar outflow have been studied by radio single dish and interferometric observations (e.g., Bachiller et al., 2001; Gueth et al., 2003; Beltrán et al., 2004). The bipolar outflow is known as chemically active, since various molecules have been detected and interestingly there is an abundance gradient that cannot be explained purely by excitation temperature differences (Bachiller et al., 2001). Recently, a flattened envelope has been detected in absorption against polycyclic aromatic hydrocarbon (PAH) background emission by deep SST IRAC observations (Looney et al., 2007).

2.3 Observations and Data Reduction

We have carried out $\lambda = 1.3$ mm and 2.7 mm continuum observations towards three Class 0 sources, L1448 IRS 2, L1448 IRS 3, and L1157, using CARMA (Woody et al., 2004), which is a recently commissioned millimeter array, combining the BIMA and OVRO (Owens Valley

Radio Observatory). It consists of 6 elements of 10.4 m antennas and 9 elements of 6.1 m antennas.[2] In order to achieve a similar synthesized beam at the two wavelengths, the $\lambda =$ 1.3 mm and 2.7 mm continuum data have been taken in the most compact E configuration and the D configuration, respectively. These two combinations of wavelengths and array configurations provide well matched synthesized beams, about $5'' \times 5''$.

This moderately matched beam size at these two wavelengths has not been achievable before CARMA. In interferometric observations, while high angular resolution can be obtained via increasing baselines of antenna elements, there is the usual missing flux problem. This is because interferometric observations are only sensitive to size scales corresponding to the *uv* coverage. To mitigate the missing flux issue, we need either an additive single dish observation or well-defined *uv* coverage with short baselines. From this point of view, the most compact CARMA E configuration is just right to study Class 0 envelope structures, since the canonical size of Class 0 source envelopes is several thousands of AU corresponding to a few tens of arc-seconds in most nearby star forming regions (e.g., the Perseus molecular cloud at a distance of 250 pc). The E configuration provides baselines from ~ 6 m to ~ 60 m ($\sim 4.6 - 46$ kλ at $\lambda = 1.3$ mm), which result in a synthesized beam (angular resolution) of about $5'' \times 5''$. A simulation shows that our data *uv* coverage recovers fluxes well ($> 50\%$) towards extended features about up to 4 times the synthesized beam size.

CARMA has a couple of special features to realize the most compact E configuration. One is an anti-collision system installed on the 6.1 m antennas, which are located in the inner region of the configuration. Antennas stop whenever they are in a danger of collision. The other feature is the coordinated movement. In larger configurations, D, C, and B configurations, antennas simultaneously in azimuth and elevation to reach a target. However, in E configuration they first go to a high elevation, then move in azimuth followed by a movement to arrive at a designated elevation, to reduce the collisional likelihood.

The $\lambda = 2.7$ mm continuum was observed in the D-like commissioning configuration of 2006 fall and winter and D configuration of 2007 summer, while the $\lambda = 1.3$ mm continuum was obtained in the E configuration of 2007 summer. Each data set was taken with one or two double-side bands of a 500 MHz bandwidth in each side band for the continuum observations. Two or one extra bands were assigned to a CO rotational transition ($J = 2 \rightarrow 1$ or $J = 1 \rightarrow 0$). The CO rotational transition data are presented in another paper with other molecular transition data. The details of each observation are listed in Table 2.1. Two and three pointing mosaics have been done to better cover the larger bipolar outflow regions for the CO $J = 2 \rightarrow 1$ transition towards L1448 IRS 3 and L1157, respectively, at $\lambda = 1.3$ mm. For this study, the northwest pointing data of L1448 IRS 3 and the central pointing data of L1157 were used.

The Multichannel Image Reconstruction, Image Analysis, and Display (MIRIAD, Sault

[2]Recently 8 elements of 3.5 m antennas (the Sunyaev-Zel′dovich Array) have been merged as well.

et al., 1995) tools have been employed to reduce and analyze data. In addition to normal procedures (linelength, bandpass, flux, and gain calibrations), shadow-defective data have been flagged in the E configuration data. Shadowing indicates cases of an antenna's line-of-sight interrupted by other antennas and usually appears in low elevation observations of compact configurations. The normal effects of shadowing are reduction and distortion of incident antenna power and abnormal gain jumps. Therefore, to obtain reliable results the shadow-defected data were flagged in the compact E configuration.

Further special attention needs to be given on flux calibration for studies involving flux comparison between different wavelengths like this study. To minimize errors caused by primary flux calibrators, we used the same primary flux calibrator (Uranus) at both wavelengths except L1157, which used MWC349 at $\lambda = 1.3$ mm and Mars at $\lambda = 2.7$ mm. We expect 15% and 10% uncertainties of flux calibrations at $\lambda = 1.3$ mm and 2.7 mm, respectively, based on the CARMA commissioning task of flux calibration. During a commissioning period extending to longer than 4 months, 12 calibrator (quasar) fluxes had been monitored by CARMA. As a result, the least varying case showed about 13% deviation in flux. When considering the intrinsic variability of quasars, it is expected that CARMA flux calibrations have about $10 - 15$% uncertainties. As a result, we consider 15% and 10% uncertainties at $\lambda = 1.3$ mm and 2.7 mm, respectively.

In addition, we make synthesized beam sizes the same as possible at both wavelengths, using weighting and tapering schemes, in order to minimize the beam size effect on the flux comparison. After proper weighting and tapering schemes, we could match the beam sizes to within 1%. The details of applied weighting and tapering schemes are listed in Table 2.2 with final synthesized beams. Briggs' robust parameter is used (Briggs, 1995), which is a knob to provide intermediate weighting between natural and uniform weighting. The parameter of 2 gives a weighting close to natural weighting and -2 close to uniform weighting.

2.4 Observation Results

2.4.1 Dust Opacity Spectral Index Maps

Total flux (F_ν) of the thermal dust continuum emission represents the total mass (M_T) of the source, if the source is optically thin at the observational frequencies,

$$F_\nu \approx \kappa_\nu \, B_\nu(T_d) \, \frac{M_T}{D^2}, \tag{2.1}$$

where κ_ν, $B_\nu(T_d)$, M_T, and D are opacity (mass absorption coefficient) of the dust grains, blackbody radiation intensity of a dust temperature T_d, total mass, and distance to the source, respectively. The opacity of dust grains (κ_ν) depends on dust properties such as

sizes, components, and shapes. If the dependence is simple, for example a power law ($\kappa_\nu \propto \nu^\beta$), the dust grain properties can be studied by observations at two frequencies. In addition, in the case that the Rayleigh-Jeans approximation of blackbody radiation is applicable ($h\nu \ll kT$), the relationship between spectral indexes of the observed flux densities (α) and spectral indexes of the dust grain opacity (β) is simply,

$$\begin{aligned} F_\nu &\approx F_{\nu_0}\left(\frac{\nu}{\nu_0}\right)^\alpha \\ F_\nu &\approx \kappa_\nu\, B_\nu(T_d)\,\frac{M_T}{D^2} \\ &\approx \kappa_{\nu_0}\left(\frac{\nu}{\nu_0}\right)^\beta \frac{2kT_d}{c^2}\,\nu^2\,\frac{M_T}{D^2} \\ \text{therefore} \quad \alpha &\approx \beta + 2. \end{aligned} \tag{2.2}$$

Note that this relation is valid only in the optically thin assumption and the Rayleigh-Jeans approximation.

Draine (2006) showed that β mainly depends on the size distribution of dust grains rather than their components and shapes; small β (~ 1) is likely indicating dust grain size distribution up to 3λ. Since our observations are up to 3 mm, $\beta \sim 1$ would suggest a grain size distribution up to about 1 cm.

Figure 2.1 presents maps of L1448 IRS 2, L1448 IRS 3, and L1157. Dust continuum maps at $\lambda = 1.3$ mm and $\lambda = 2.7$ mm have been separately constructed using different weightings and taperings as described in Section 3.2 and Table 2.2 in order to have as similar synthesized beams as possible at the two wavelengths. Afterwards β values of each source have been calculated using the two continuum images. Only regions above three signal-to-noise ratio (SNR) levels on the both maps have been used to derive β assuming

$$\beta = \frac{\log(F(\nu_1)/F(\nu_0))}{\log(\nu_1/\nu_0)} - 2, \tag{2.3}$$

where ν_1 and ν_0 are frequencies corresponding to $\lambda = 1.3$ mm and $\lambda = 2.7$ mm data, as listed in Table 2.2. Note that the Rayleigh-Jeans approximation and the optically thin assumption are used. In the case of an average dust temperature of about 30 K, the upper limit of frequencies to which the Rayleigh-Jeans approximation can be applied is about 625 GHz. Since the higher frequency of our data is about 230 GHz, the assumption is valid for this study. However, caution should be taken in β comparison at submillimeter wavelengths for cold objects such as the Class 0 YSO envelopes.

As shown in Figure 2.1, most β values in the three targets are less than 1. For a convenient comparison, the same gray scales have been adopted for all three maps. The actual ranges of β values are in Table 2.3 with the averages. As listed in the table, the maximum values are larger than 1.0. However, those large β values appear only on a few

pixels of source boundaries, which may be due to contamination from ambient clouds. β and its averages in most regions of the three sources are similar to or less than 1. In the case of L1448 IRS 3, in which three Class 0 sources (3A, 3B, and 3C) exist, β values corresponding to the three sources are separately listed in Table 2.3. Like the other targets, these three sources of L1448 IRS 3 have β around 1 or less. The L1448 IRS 3A and 3B fluxes are obtained simply by cutting the protuberance in Figure 2.1. Table 2.3 also has β values obtained from the total fluxes at the two wavelengths, which have been estimated in source regions limited by the SNR threshold of 3 at both wavelengths. All sources except L1448 IRS 3B have β values comparable to the mean values of the β maps.

Another feature to note is that there are β gradients with radius in all sources. L1157 has a smaller β in the northeast-to-southwest direction, roughly consistent with the $\lambda = 1.3$ mm and 2.7 mm results of Beltrán et al. (2004). However, it is noteworthy that they restored their two images with an identical beam size without any weighting schemes, which could cause a biased result due to different *uv* coverage of the two wavelength data. The radial dependence of β is better shown in Section 2.4.2 and is discussed in detail for the L1448 IRS 3B case via modeling in Section 2.6

2.4.2 Visibility Data Comparison

We have also examined β values in *uv* space, which is the Fourier transformed space of an image. Data of interferometric observations are obtained in *uv* space and called *uv* visibilities or just visibilities. To obtain a sky intensity distribution, inverse Fourier transformation and deconvolution (e.g., CLEANING algorithm) are employed (e.g., Thompson et al., 2001). However, limited *uv* coverage causes difficulties, i.e., the deconvolution introduces systematic biases, especially for non-point, extended sources. One of the best ways to overcome this difficulty is to investigate the visibility data in *uv* space instead.

The results of β calculated in *uv* space are displayed in Figure 2.2. Visibilities have been vector-averaged in annuli. Since the envelope structures from our observations are spherical, the annulus averaging is valid. The annulus bin sizes are ~ 3.1 kλ except when the SNR is too low, usually at the relatively longer baselines. This is most noticeable in L1157 at $\lambda = 2.7$ mm. Although the *uv* coverage is comparable at both wavelengths, the lower SNR at $\lambda = 2.7$ mm requires larger bins. The β values are calculated at the $\lambda = 1.3$ mm bins with $\lambda = 2.7$ mm visibilities linearly interpolated using the nearest bin values. When the $\lambda = 1.3$ mm bin center is beyond last $\lambda = 2.7$ mm bin center (extrapolation case), then the nearest bin value for $\lambda = 2.7$ mm is used.

In the case of L1448 IRS 3, only 3B is considered for the β calculation in *uv* space. The other two objects, 3A and 3C, are too small and weak to carry out the calculation. On the other hand, 3A and 3C should be removed from the visibilities to obtain the 3B data. Using the MIRIAD task UVMODEL and image models excluding the two components, we

subtracted the 3A and 3C visibilities at both $\lambda = 1.3$ mm and $\lambda = 2.7$ mm separately. In addition, since the $\lambda = 1.3$ mm data set has been taken with two pointings offset from the center, we compensated the primary beam sensitivity loss using a UVMODEL multiplication.

In Figure 2.2, the upper panels show amplitudes of $\lambda = 1.3$ mm (open squares) and $\lambda = 2.7$ mm cases (open triangles). The error bars represent the statistical standard errors in each bin. The solid and dashed lines present the best fit models described in Section 2.5 and Figure 2.3. The lower panels show β values with uv distance, calculated by equation (2.3). The open circles indicate β values calculated from the uv visibilities shown on the upper panels. The error bars with caps on the open circles represent β value ranges corresponding to the statistical amplitude errors of the upper panels. The filled circles and error bars without caps show the effect that the absolute flux calibration uncertainty has on the calculation of β. We adopt 15% flux calibration uncertainties for $\lambda = 1.3$ mm data and 10% for $\lambda = 2.7$ mm data, as discussed in Section 3.2. The larger β points indicate the case in which 15% higher fluxes at $\lambda = 1.3$ mm and 10% lower fluxes at $\lambda = 2.7$ mm are considered and vise verse for the lower β points. The β ranges are around ± 0.35, as $\log(1.15/0.90)/\log(\nu_1/\nu_0) \approx 0.35$ where $\nu_1/\nu_0 \approx 2$ (refer to Equation 2.3).

Two main features should be noted in Figure 2.2. One point is that the β values are around 1 or less than 1 in all three objects. It is arguably true even when considering the absolute flux calibration uncertainties. The other point is the radial dependences of β. In L1448 IRS 2 and L1157, β arguably decreases on smaller scales (larger uv distances). L1448 IRS 3B, however, distinctly presents a radial dependence. The β variation is fit with the logarithmic function of $\beta(\zeta) = 1.0 - 0.57 \log(\zeta)$, where ζ is the uv distance in units of kλ. When assuming power-law distributions of density and temperature of envelopes as discussed in Section 2.5, the distributions of the intensity integrated along line-of-sight as well as the radial intensity follow a power-law under the optically thin assumption and Rayleigh-Jeans approximation (Adams, 1991). When ignoring primary beam effects of interferometers and assuming infinite size envelopes, the visibilities are also in a power-law (e.g. Harvey et al., 2003; Looney et al., 2003). As β is obtained from equation (2.3) here, we assume a logarithmic function of $\beta(\zeta)$. There are a few possible interpretations to explain this radial dependence of β. It could be caused by increasing the fraction of optically thick emission on smaller scales due to the denser central region. Beckwith et al. (1990) discussed that the optically thick emission fraction (Δ) decreases β by a factor of $(1 + \Delta)$, i.e., $\beta \simeq \beta_0/(1 + \Delta)$. Similarly, it could be due to an optically thick, unresolved, deeply embedded disk structure at the center. Otherwise, it could indicate a faster grain growth in the denser central region or dust grain segregation suggested by some star formation theories, for example, ambipolar diffusion in magnetically supported molecular cloud (Ciolek & Mouschovias, 1996). The radial dependence is discussed in more detail in Section 2.6.

2.5 Modeling in uv space

As mentioned in Section 2.4.2, images of extended features constructed from interferometric observations may be biased due to limited uv coverage. In contrast, comparing visibility data against source models transformed to the visibility plane (including the primary beam modification, Fourier transformation, and visibility sampling), is not prone to these imaging deconvolution biases. Therefore, we carry out envelope modeling in uv space rather than in image space. In other words, we compare observation visibilities with model visibilities sampled over the observation uv coverage, after obtaining uv models by the Fourier-transformation of image models.

We assume that the temperature distribution of dust grains is in radiative equilibrium with the central protostar, ignoring heating by gas and cosmic rays (Spitzer, 1978, p 193):

$$c \int_0^\infty Q_a(\nu)\, u_\nu \, d\nu = 4\pi \int_0^\infty Q_a(\nu)\, B_\nu(T_d)\, d\nu, \tag{2.4}$$

where $Q_a(\nu)$, u_ν, $B_\nu(T_d)$, and c are absorption efficiency factor, radiation energy density, black body radiation intensity of temperature T_d, and speed of light, respectively. The radiation energy density (u_ν) at a distance r from the center can be expressed as $\pi B_\nu(T_*)\, R_*^2/r^2$, where T_* and R_* are an effective temperature and a radius of a central protostar. Assuming $Q_a(\nu) \propto \nu^\beta$, equation (2.4) gives a temperature distribution of dust grains (Beckwith et al., 1990),

$$T_d(r) = T_* \left(\frac{1}{2}\frac{R_*}{r}\right)^{2/(4+\beta)}. \tag{2.5}$$

Again, β is the dust grain opacity spectral index ($\kappa_\nu = \kappa_0(\nu/\nu_0)^\beta$). This equation can also be formulated with a grain temperature T_0 at a distance R_0 from the central protostellar luminosity L_0, as (e.g., Looney et al., 2003)

$$T_d(r) = T_0 \left(\frac{R_0}{r}\right)^{2/(4+\beta)} \left(\frac{L_*}{L_0}\right)^{1/(4+\beta)}. \tag{2.6}$$

Although the inner region, which might be optically thick, could have a sharper temperature gradient than this relation (e.g., Wolfire & Cassinelli, 1986; Looney et al., 2003), it is limited at the very central region, and our results are not sensitive to the possibility, as further discussed in Section 2.6.

Some previous studies (e.g., Harvey et al., 2003) considered the external heating by the interstellar radiation field, using a temperature lower limit of 10 K. However, we do not explicitly include this effect, since the temperature lower limit is uncertain and the lowest temperature of our modeling is comparable, about 7.3 K at $r = 7000$ AU when adopting $T_0 = 100$ K at $r = 10$ AU. In addition, tests show that the temperature lower limit does not change our results, as previous studies also reported (e.g., Harvey et al., 2003). The outer

envelope heated externally by the interstellar radiation field would be the main intensity component in sources without any central heating objects, but in Class 0 YSOs the central high temperature region drives the emission. Besides, interferometric observations are not so sensitive to the outer envelope, where the effect of the temperature lower limit is largest.

The power-law density distribution is assumed for envelopes, $\rho(r) = \rho_0(r/r_0)^{-p}$. Therefore, the intensity of envelopes on the plane of the sky is calculated as

$$I_\nu = \int B_\nu(T_d(r))\ e^{-\tau_\nu}\ d\tau_\nu = \int B_\nu(T_d(r))\ e^{-\tau_\nu}\ \rho(r)\ \kappa_\nu\ dL, \tag{2.7}$$

where L indicates the line-of-sight from the observer and the optical depth $\tau_\nu = \int_0^L \kappa_\nu\ \rho(r)\ dL'$. Spherical envelopes with an outer radius of R_{out} and with an inner hole of a radius of R_{in} are assumed. Therefore, the density distribution can be expressed with the total envelope mass M_T (when $p \neq 3$) as

$$M_T = \int_{R_{in}}^{R_{out}} \rho(r)\ 4\pi r^2\ dr = \frac{4\pi}{3-p}({R_{out}}^{3-p} - {R_{in}}^{3-p})\ \rho_0\, {r_0}^p \tag{2.8}$$

$$\rho(r) = \rho_0\, {r_0}^p\ r^{-p} = M_T\ \frac{3-p}{4\pi}({R_{out}}^{3-p} - {R_{in}}^{3-p})^{-1}\ r^{-p}. \tag{2.9}$$

Substituting the density expression with the total envelope mass into the optical depth of equation (2.7) shows a coupling of M_T and κ_0 — in the case that the envelope is optically thin and the Rayleigh-Jeans approximation ($B_\nu(T_d(r)) \approx 2kT_d(r)/\lambda^2$) is valid, T_0 is also coupled. Normally the envelopes of this stage YSO are optically thin in the $\lambda = 1.3$ mm and 2.7 mm continua except the very central regions (within a few tens of AU) and the Rayleigh-Jeans approximation is applicable, which means that the M_T, κ_0, and T_0 are all likely coupled. However, note that the optically thin assumption and Rayleigh-Jeans approximation, which are assumed in β calculations of observational data in Section 2.4.1 and 2.4.2, are not assumed in the modeling to avoid biases. Here we just intend to point out that the three parameters are likely to be coupled.

After constructing intensity image models, they are corrected by three different CARMA primary beams, which correspond to baselines of two 10.4 m antennas, two 6.1 m antennas, and 10.4 m and 6.1 m antennas. The three primary-beam corrected images are Fourier-transformed into *uv* space and model visibilities are sampled over the actual observational *uv* coverage of the three different baselines. Comparison between model and observation visibilities is done by vector averaged values in annulus bins. Although bipolar outflows at this stage carve a cavity (e.g., Seale & Looney, 2008), the effect is minor (Chandler & Richer, 2000), especially at our intermediate angular resolution. In addition to the bipolar outflow effect, envelopes might be clumpy. However, the effect on our modeling is also insignificant, since the angular resolution of our data is intermediate and annulus-averaged

values are used for the comparison of models and data.

Parameters involved in our modeling are p (power-law density index), β (opacity spectral index), M_T (envelope total mass), κ_0 (opacity coefficient at ν_0), T_0 (grain temperature at R_0), R_{in} and R_{out} (inner and outer radii of envelopes), and F_{pt} (a central point source flux at $\lambda = 2.7$ mm). Among these, two parameters are fixed: $\kappa_0 = 0.0114$ cm^2 g^{-1} at $\nu_0 = 230$ GHz and $T_0 = 100$ K at $R_0 = 10$ AU. As discussed, the κ_0 and M_T are coupled (and so T_0 is mostly), so we cannot well constrain these parameters simultaneously. The T_0 at R_0 corresponds to a central object luminosity of 1.67 $L_\odot$ and the κ_0 at $\nu = 230$ GHz is the average of $\beta = 1$ and 2 cases in $\kappa_\nu = 0.1\,(\nu/1200\ \mathrm{GHz})^\beta$, assuming a gas-to-dust mass ratio of 100 (e.g., Hildebrand, 1983; Beckwith et al., 1990). Ossenkopf & Henning (1994) also reported $\kappa \approx 0.01$ cm^2 g^{-1} at $\lambda = 1.3$ mm for dense protostellar cores via dust coagulation model calculation, when using a gas-to-dust mass ratio of 100. Note that κ_0 is not very well known and has a large uncertainty (e.g., Hildebrand, 1983; Beckwith & Sargent, 1991) so we need to pay attention to the fact that the total mass M_T could have a large uncertainty. M_T can also be scaled by the presumed T_0.

The central point source flux (F_{pt}) is designed to simulate an unresolved central disk structure. We assumed that the point sources are optically thick so that the flux density spectral index is 2 under the Rayleigh-Jeans approximation, meaning $\beta = 0$. In the case of L1448 IRS 2 there is no point source required, since there is no flat visibility amplitude on the small scales, particularly at $\lambda = 1.3$ mm in Figure 2.2. It may indicate that the central disk structure of the source is not so significant. In contrast, L1157 has a flat profile on the small scales, which means a compact structure at the center. Therefore, a point source is adopted to fit the data. Indeed, Beltrán et al. (2004) reported a compact component (size $< 1''$) of 25 mJy and 78 mJy at $\lambda = 2.7$ mm and 1.3 mm, respectively. On the other hand, the point source of L1448 IRS 3B was applied for a different reason: to simulate a radial dependence of β. As shown in Figure 2.2, there is a clear radial dependence of β, which results in no good fits with a constant β over all scales. It is why an optically thick point source is considered, although there is no flat feature on the small scales. Note that even higher angular resolution observations have not detected such a point source signature (Looney et al., 2003). We further discuss the β radial dependence of L1448 IRS 3B in Section 2.6.

In order to find good fit models, we search grids of parameters, p, β, M_T, R_{in}, R_{out}, and F_{pt}. Parameter set information of the three sources is listed in Table 2.4. On each grid point of parameters, the reduced χ^2 (χ^2_ν) has been calculated. The two wavelength data were used simultaneously for fitting. Note that the absolute χ^2_ν values particularly in L1448 IRS 3B (~ 8.7) are large, compared to L1448 IRS 2 (~ 1.6) and L1157 (~ 1.5). This is because the relatively small standard errors due to the high brightness of L1448 IRS 3B make fitting very difficult. The L1448 IRS 3B data may have imperfect exclusion

of the companion L1448 IRS 3A, which might cause a difficulty in fitting. However, it is unlikely to be the main effect, since the companion is relatively weak and we subtracted the component as mentioned in Section 2.4.2. In addition, the vector averaging in annuli minimizes the effect. On the other hand, it may indicate that the simple power-law model is not appropriate to explain high SNR observations (e.g., Chiang et al., 2008).

We adopt a likelihood calculation to constrain p and β, instead of reporting large ranges of each parameter to fit the data. Reporting good fit parameter ranges could bias the impression of the results, since each parameter value in the range comes from different combinations of the other parameters. The likelihood function we adopt is $\exp(-\chi^2_\nu/2)$, since the annulus averaged visibilities have a Gaussian distribution based on the central limit theorem. As we want to constrain p and β, the likelihoods of all grid points with common p and β are summed. The sum now indicates the likelihood of a set of p and β. Finally, it is normalized by the total sum of the likelihoods in each plot of Figure 2.3, which means that the plots are comparable to probability density distributions of p and β. Note that we do not consider the absolute flux calibration uncertainties for fitting. In other words, we use data points marked with open symbols in Figure 2.2. Note that while systematic changes of absolute fluxes in the same direction at both $\lambda = 1.3$ mm and 2.7 mm affect the total mass M_T, the opposite direction changes mainly influence β. We estimate that the maximum β ranges caused by the absolute flux calibration uncertainties are ± 0.35, as mentioned in Section 2.4.2.

We present the most likely β and p in Figure 2.3. As clearly shown in the figure, β of the three sources are most likely to be around 1 even in the modeling without the optically thin assumption and Rayleigh-Jeans approximation. These are the first clear modeling results showing the β of Class 0 YSOs. The contours in Figure 2.3 indicate likelihood levels of 90% down to 10% of the peak in steps of 10% and the triangles and circles mark the p and β pairs of the best fit models and likelihood weighted averages of individual parameters, respectively. Note that, therefore, the combinations of the weighted averages are not necessarily the best fit. Since a model with a point source is not the best one for L1448 IRS 3B, its contours are drawn in dashed lines. (The best model is discussed in Section 2.6 and displayed in Figure 2.6.) The broader distribution in p of L1157 is due to the adopted point sources. As having a point source implies a density gradient, it lowers the density index. The two dotted contours in the L1157 plot present 90% and 80% of the peak likelihood based on all models in the whole range of the point source fluxes F_{pt} ($0.000-0.035$ Jy at $\lambda = 2.7$ mm) listed in Table 2.4. In contrast, the solid contours of L1157 in Figure 2.3 show the likelihood distribution obtained from models in a limited range of F_{pt} ($0.015-0.025$ Jy) around the likelihood weighted average (0.019 Jy at $\lambda = 2.7$ mm and 0.078 Jy at $\lambda = 1.3$ mm), which is consistent with the compact component flux measured by Beltrán et al. (2004).

While the power-law density indexes of L1448 IRS 2 and L1157 are around 1.8 and 1.7, respectively, that of L1448 IRS 3B is around 2.1. The density index of L1448 IRS 3B is consistent with the lower limit of Looney et al. (2003) using BIMA data and the L1157 result is consistent with that of Looney et al. (2007) using Spitzer IRAC absorption features. The density distribution of L1448 IRS 2 has not been studied. It is interesting to note that star formation theories have suggested density indexes between 1.5 and 2.0; "inside-out" collapse models (Shu, 1977) suggested 1.5 for the inside free-fall region and 2.0 for the outside isothermal envelope, where the expansion wave does not reach yet, and ambipolar diffusion models (e.g., Mouschovias, 1991; Tassis & Mouschovias, 2005) suggested around 1.7 but with the very inner regions dependent on magnetically controlled accretion bursts. Although we do not attempt to constrain the star formation theories in this paper, the difference in density indexes between L1448 IRS 3B and the others is noteworthy. The difference even increases in the better model of L1448 IRS 3B in Section 2.6.

It is important to note that the constraints on the inner and outer radii are not very strong. While the inner radius of L1448 IRS 3B is likely to be 10 AU rather than 20 AU, there is no likely inner radius for L1448 IRS 2 and L1157 in the parameter search space. In addition, while the outer radius of L1157 is likely around $2000-2500$ AU, the outer radii of L1448 IRS 2 and L1448 IRS 3B cannot be constrained well due to lack of sensitivity of the data toward large scales. We can only say that the preferred fits for these two sources have a larger outer radius. The values given in Table 2.4 are limited by our parameter search space.

2.6 Radial Dependence of β

We verify the radial dependence of β that is shown in L1448 IRS 3B and attempt a modeling with β as a function of radius in this section. This result is the first evidence to clearly show a radial dependence of β in Class 0 YSOs via *uv* modeling. Some previous studies have suggested a radial dependence of β, for example, in dust cores of NGC 2024 (Visser et al., 1998), the Class 0 source HH211-mm (Chandler & Richer, 2000), and four Class I sources (Hogerheijde & Sandell, 2000). However, the results are not clear and it could be due to other effects such as an optical thickness effect or an improper consideration of temperature effects, since their results are based on submillimeter wavelength observations, in which the β evaluation is more sensitive to the temperature.

As mentioned in Section 2.5, an optically thick point source has been adopted to fit L1448 IRS 3B data. First, to verify that the point source should be optically thick to imply a radial variation of β, we tested the case of a point source with the same β to that of its envelope. As expected, a point source with the same β as the envelope requires a smaller β to fit the data (Figure 2.4). The dashed contours in Figure 2.4 are 80%, 60%, and 40%

of the peak value in the likelihood distribution of the same models in Figure 2.3 and the dotted contours are 80%, 60%, and 40% of the likelihood peak in the new models with a point source having the same β to the envelope. A parameter space of $p : 1.9 - 2.4$ and $\beta : 0.4 - 0.9$ with the other parameter ranges the same as the optically thick point source models, except R_{in} which was fixed at 10 AU, has been searched. In addition to the smaller β, it is noteworthy that there is no "good" fit. The "best fit" gives $\chi^2_\nu \sim 11$, which is much worse than the case of the optically thick point source case ($\chi^2_\nu \sim 8.7$). This is expected as there is no good way to well fit the two wavelength data simultaneously without a variable β along radius. Note that the differences between the two wavelength amplitudes are only sensitive to β. Since we assume a constant β for the point source and the envelope in the new model, the differences between the two wavelength amplitudes along radius can be caused only by the optically thick emission due to the density increase of the inner envelope. As the new model is worse than the optically thick point source model, this test also implies that the optically thick emission, purely due to the density increase of the inner envelope of L1448 IRS 3B, is not significant enough to explain the β variation in the data.

Similarly, better (probably more "realistic", a sharper temperature gradient in inner regions) temperature distributions such as of Looney et al. (2003) and Chiang et al. (2008) cannot fit the data either. We tested simulated temperature distributions similar to those studies and verified that they do not provide radially variable differences between the two wavelengths. The dotted line in Figure 2.5 is an example of fitting models with the better temperature distribution but with a constant β over radius. As shown, it does not produce the variable amplitude differences with radius between the two wavelengths. It is understandable since the inner regions are hotter resulting in a valid Rayleigh-Jeans approximation, i.e. no slope change between the two wavelengths due to temperature variation.

Finally, we construct a model to simulate the variable β as a function of radius, based on grain growth. A point source of L1448 IRS 3B seems to be weaker than 20 mJy if it existed, according to Looney et al. (2003), whose data went to ~ 400 kλ at $\lambda = 2.7$ mm. Therefore, modeling with an optically thick point source is not the best way, although it provides a relatively "good" fit for our intermediate angular resolution data. For this reason, we do not consider a point source in the following model.

We assume grain growth by gas accretion onto grain surfaces. Grains can grow by gas accretion and coagulation and can be destroyed or denuded by grain-grain collisions and heating mechanisms such as cosmic rays, central protostellar radiation, and bipolar outflow shock waves (e.g., Draine, 1985). To address grain growth fully, these growth and destruction mechanisms may need to be taken into account together. However, we presume only grain growth by gas accretion without considering any destruction mechanisms for simplicity. Coagulation might contribute significantly in the dense envelopes but its efficiency is uncertain (e.g., Flower et al., 2005). Grain growth by coagulation requires relative grain mo-

tion, which can be introduced by various mechanisms. Relative velocities caused by thermal movement, ambipolar diffusion, and radiation pressure lead to grain coagulation rather than grain shattering; the velocities are smaller than the critical velocities, which are the upper limits of velocity for grain coagulation depending on grain properties such as size, composition, and shape. The critical velocities have been studied theoretically (e.g., Chokshi et al., 1993) and experimentally (e.g., Blum, 2000; Poppe et al., 2000). However, the velocity is too small to consider coagulation as an efficient mechanism for grain growth (Draine, 1985). Alternatively, hydrodynamically or magneto-hydrodynamically induced turbulence (e.g., Yan et al., 2004) could bring a faster relative velocity of grains. However, it depends on the maximum velocity at the incident scale, which is highly uncertain, and it may also lead to grain destruction due to high velocities. In addition, even when considering the fastest relative velocity of grains for coagulation (the critical velocity), coagulation may not be as efficient as gas accretion (Flower et al., 2005).

The grain growth rate by gas accretion has a relationship with density and temperature distributions, $da/dt \propto w\rho \propto T^{1/2}\rho$, where a and w indicate a grain size and a colliding gas velocity (Spitzer, 1978, p 208). Note that although we assume only grain growth by gas accretion, grain growth rate by coagulation has a similar relationship with the density and relative velocity of grains instead of gas density and velocity. Overall, this formulation is arguably valid for a general description of grain growth, in a well-mixed gas and dust region. In addition to the grain growth rate, we simply assume that β is inversely proportional to the maximum grain size (Draine, 2006). Therefore, after some time period, $\beta(r)$ is inversely proportional to the product of the density distribution and the square root of the temperature distribution,

$$\beta(r) = \begin{cases} \beta_{out}(r/R_\beta)^p \left(T_d(R_\beta)/T_d(r)\right)^{1/2} & \text{where } r \leq R_\beta \\ \beta_{out} & \text{where } r > R_\beta. \end{cases}$$

We fix $\beta_{out} = 1.7$ (e.g, Draine, 2006) and instead introduce R_β for an adjustment of the radial dependence. In addition, we allow the temperature distribution to change along $\beta(r)$. However, $T_d(r) = T_0(R_0/r)^{2/(4+\beta(r))}$ is not a monotonic function, i.e., presumably not realistic. Therefore, we design a temperature distribution smoothly changing from a case of $\beta = 0$ to a case of $\beta = \beta_{out}$ around R_β,

$$T_d(r) = \frac{W_1(r)\,T_1(r) + W_2(r)\,T_2(r)}{W_1(r) + W_2(r)}, \tag{2.10}$$

where $W_1(r) = R_\beta/r$, $W_2(r) = r/R_\beta$, $T_1(r) = T_0(R_0/r)^{2/4}$, and $T_2(r) = T_0(R_0/r)^{2/(4+\beta_{out})}$. We recognize that the temperature distribution might not be the best one corresponding to the variable β. However, we point out that the temperature distribution mainly changes

the flux density profiles, not the differences between flux densities of the two wavelengths (Figure 2.5). Therefore, the modeling here focusing on the variable β, which is implied for the variable differences of the flux densities along radius, is not sensitive to the temperature distribution. We searched a parameter space of p, M_T, R_{out}, and R_β with the other fixed parameters ($\beta_{out} = 1.7$, $R_{in} = 10$ AU, $F_{pt} = 0.0$ Jy, $T_0 = 100$ K at $R_0 = 10$ AU) as listed in Table 2.5. Figure 2.6 shows the result, a likelihood distribution on p vs. R_β. The p and R_β are most likely to be about 2.6 and 400 AU, respectively. The parameter set of the best fit model ($\chi^2_\nu \sim 7.1$) is $p = 2.6$, $M_T = 2.20$ $M_\odot$, $R_\beta = 400$ AU, and $R_{out} = 4500$ AU and the averages weighted by the likelihood are $p = 2.59$, $M_T = 2.51$ $M_\odot$, $R_\beta = 420$ AU, and $R_{out} = 5900$ AU. The best fit model is plotted in Figure 2.5 overlaid with the observational data.

In this model, the best fit suggests an envelope that is mostly "interstellar medium grains" (small grains with $\beta \sim 1.7$), with grain growth at the very center, $R_\beta \lesssim 400$ AU, which is approximately the smallest structure sensitivity of these observations. It is important to note that this is not equivalent to models of an "interstellar medium grain" envelope with a point source of a smaller β value, as those models do not fit (Figure 2.4), and in addition, such a bright point source at $\lambda = 2.7$ mm is not consistent with the results of Looney et al. (2003).

The p value (~ 2.6) is larger than the value (~ 2.1) obtained in Section 2.5 assuming an optically thick point source. This is understandable because applying a point source itself causes a density gradient, as mentioned in Section 2.5 for L1157. Actually, this p value is more consistent with the results of Looney et al. (2003) using larger uv coverage data and a higher angular resolution at $\lambda = 2.7$ mm. Based on the facts that the data of L1448 IRS 3B do not have a point source feature and that this model has a smaller $\chi^2_\nu \approx 7.1$, we argue that the larger p from this model is more reliable.

To understand the large difference between p values of L1448 IRS 3B and the other two sources, we focus on the differences of the apparent properties. While L1448 IRS 2 and L1157 are isolated and have a very large bipolar outflow ($\sim 5'$), L1448 IRS 3B is in a "binary system" and its bipolar outflow is not so extended (e.g., Kwon et al., 2006). These facts imply that the density distribution could be steeper in binary and/or younger (based on the kinematic time scales of bipolar outflows) YSOs such as L1448 IRS 3B. Looney et al. (2003), who have carried out uv modeling towards 6 sources, have also reported relatively steeper density distributions for bright YSOs of "binary systems" such as NGC 1333 IRAS 4B and L1448 IRS 3B. However, density indexes larger than 2 are somewhat puzzling, since they indicate expansion rather than collapse, i.e., the thermal pressure gradient exceeds the gravitational force. However, we might be able to connect this aspect to their binarity, in which the outer envelope is affected by the companion, or their youngness, in which the envelope is affected by the bipolar outflow momentum. Detailed theoretical studies are

needed to understand this.

The R_β value indicates an outer limit where grain growth mainly occurs. According to Spitzer (1978), the grain growth rate by gas accretion in the diffuse interstellar medium ($T = 80$ K, $n_H = 20$ cm^{-3}) is given by,

$$\frac{da}{dt} = 2 \times 10^{-12}\, \xi_a \left(\frac{T}{80\ \mathrm{K}}\,\frac{1}{\mu}\right)^{1/2} \left(\frac{n_H}{20\ \mathrm{cm}^{-3}}\right) \frac{\mathrm{mm}}{\mathrm{year}}, \tag{2.11}$$

assuming a typical dielectric grain density and a cosmic composition gas. The ξ_a is a sticking probability, and the μ is the mean gas particle weight. Although grain growth in dense regions such as the central regions of Class 0 YSO envelopes could be different, it is applicable as discussed before. Simply compensating for our temperature (~ 40 K), the mean gas particle weight increase (two-atomic molecular gas rather than atomic gas), and density ($n_H \sim 10^9$ cm^{-3} at 200 AU), we can obtain $da/dt = 5 \times 10^{-5} \xi_a$ (mm/year). When accepting $\xi_a = 1$,[3] this implies that a time scale of 10^4 years, comparable to the kinematic time scales of bipolar outflows of Class 0 YSOs (e.g., Bachiller et al., 2001), can result in about mm-size grains. Although grain growth could also occur in previous stages, it is much more efficient in the higher densities of the Class 0 stage. Another interesting point is that less massive (i.e., less bright) and less steep density distribution envelopes such as those of L1448 IRS 2 and L1157 would have smaller radial regions for the grain growth within the same time scale. Then, in such sources, the variation of β may not be distinct nor distinguishable from a point source, as shown in Section 2.4.2.

We interpreted the radial dependence of β based on grain growth above. However, there could be another effect, grain segregation. Ciolek & Mouschovias (1996) showed that magnetic fields in protostellar cores reduce abundances of small grains in the cores by a factor of its initial mass-to-magnetic field flux ratio. In other words, a stronger magnetic field with respect to the mass of a core causes more effective segregation. Although this segregation occurs while the ambipolar diffusion appears, before dynamical collapse, the signature footprint could remain in the envelopes of Class 0 YSOs. On the other hand, although this effect would be minor to the features we have discussed because the segregation is effective to relatively small grains ($a \lesssim 10^{-4}$ cm), it is noteworthy that it would set the initial grain distribution of Class 0 YSO envelopes for more efficient growth in the central region.

[3] Although Spitzer (1978) assumed $\xi_a = 0.1$ for the diffuse interstellar medium, $\xi_a = 1$ is arguably a better assumption for the cold and dense inner envelope regions (e.g., Flower et al., 2005).

2.7 Conclusion

We carried out interferometric observations towards three Class 0 YSOs (L1448 IRS 2, L1448 IRS 3, and L1157) at $\lambda = 1.3$ mm and 2.7 mm continuum using CARMA. The continuum at these millimeter wavelengths is mainly thermal dust emission of their envelopes. Our observations have been designed particularly to cover comparable uv ranges at the two wavelengths, which allowed us to tackle dust grain opacity spectral indexes (β) of Class 0 YSOs, using unprecedented compact configuration and high image fidelity. Through simultaneous modeling of the two wavelength visibilities as well as comparisons of the images and visibilities for the first time, we found not only the β of Class 0 YSOs but also its radial dependence. In addition, we addressed the single power-law density index p of Class 0 YSO envelopes.

1. We found that the dust opacity spectral index β of the earliest YSOs, so-called Class 0, is around 1. This implies that dust grains have significantly grown already at the earliest stage.

2. We obtained the power-law density index p of ~ 1.8, ~ 2.6, and ~ 1.7 for L1448 IRS 2, L1448 IRS 3B, and L1157, respectively. Although we did not attempt to constrain star formation theories, we pointed out the difference between that of L1448 IRS 3B and those of the other two. Based on different properties of L1448 IRS 3B from the other two sources, we suggested that "binary system" YSOs and/or younger YSOs in terms of kinematic time scales of their bipolar outflows would have steeper density distributions.

3. We found radial dependences of β. In particular, the dependence is distinct in L1448 IRS 3B. We verified it by models employing β as a function of radius. In addition, we discussed that the grain growth causing the dependence can be achieved in a time scale of 10^4 years, corresponding to the kinematic time scale of bipolar outflows of Class 0 YSOs.

Table 2.1 Targets and observations

Source	α (J2000.0)	δ (J2000.0)				
Wavelength	Date	Flux cal.	Gain cal.	Flux	Array	Beam size (PA)[a]
L1448 IRS 2	03 25 22.346	+30 45 13.30				
1.3 mm	2007 Aug. 21	Uranus	3C84	4.0	E	$5\farcs3 \times 4\farcs4$ (-72°)
			0237+288	1.2		
2.7 mm	2006 Sep. 02	Uranus	0237+288	1.6	Comm.[b]	$4\farcs8 \times 4\farcs3$ (-74°)
	2006 Sep. 12	Uranus	0237+288	1.6	Comm.	
L1448 IRS 3	03 25 36.339	+30 45 14.94				
1.3 mm	2007 Aug. 19	Uranus	3C84	3.9	E	$5\farcs0 \times 4\farcs3$ (71°)
			0237+288	1.2		
2.7 mm	2006 Dec. 03	Uranus	0237+288	1.88	Comm.	$5\farcs0 \times 4\farcs5$ (43°)
L1157	20 39 06.200	+68 02 15.90				
1.3 mm	2007 Aug. 20	MWC349[c]	1927+739	0.95	E	$4\farcs6 \times 3\farcs8$ (24°)
2.7 mm	2007 Jul. 12	Mars	1927+739	1.6	D	$7\farcs0 \times 5\farcs6$ (7°)

[a] The synthesized beam in the case of natural weighting.

[b] An array configuration for commissioning tasks, similar to D. Note that only part of the array was available in some cases.

[c] The flux is assumed as 1.8 Jy, based on periodic CARMA flux calibrator measurements.

Table 2.2 Weighting and tapering schemes and final synthesized beams

Source	Frequency [a] (GHz)	Weighting (Robust)[b]	Tapering	Beam Size (PA)[c]	Beam Ratio (1 mm / 3 mm)
L1448 IRS 2	228.60	0.8		$4\farcs986 \times 4\farcs168$ (-78.91°)	
	112.94	natural		$4\farcs826 \times 4\farcs277$ (-74.06°)	1.007
L1448 IRS 3	228.60	natural		$5\farcs049 \times 4\farcs299$ (70.87°)	
	112.84	1.1		$4\farcs951 \times 4\farcs412$ (43.29°)	0.994
L1157	228.60	natural	$5\farcs6 \times 6\farcs1$	$5\farcs597 \times 5\farcs026$ (-10.95°)	
	113.00	0.0		$5\farcs644 \times 5\farcs015$ (-3.850°)	0.994

[a] The frequencies used for β calculation. Refer to Equation (2.3).

[b] Briggs' robust weighting factor (Briggs, 1995).

[c] Beam size uncertainties are order of $0.1''$, and the values shown are to illustrate the beam size ratios.

Table 2.3 β values of the sources

	Fluxes (Jy)			β maps		
Sources	1.3 mm	2.7 mm	β	Minimum	Maximum	Average
L1448 IRS 2	0.20	0.025	0.95	0.70	1.6	1.0
L1448 IRS 3						0.60
L1448 IRS 3A	0.090	0.012	0.85	0.32	1.7	0.90
L1448 IRS 3B	1.0	0.19	0.35	-0.14[a]	1.7	0.53
L1448 IRS 3C	0.15	0.026	0.48	0.12	2.1	0.59
L1157	0.29	0.050	0.49	-0.008[a]	1.3	0.47

[a] The negative β values are due to a bias introduced in deconvolution.

Table 2.4 Model parameter sets for the three sources

Targets		p	β	M_T ($M_\odot$)	R_{in} (AU)	R_{out} (AU)	F_{pt}[a] (Jy)	T_0[b] (K)
L1448 IRS 2	Δ[c]	1.5–2.0	0.5–1.5	1.00–2.00	10–30	4000–6000	0	100
	δ[d]	0.1	0.1	0.05	10	500	–[e]	–
	best[f]	1.8	0.9	1.35	10	5500	0	100
	mean[g]	1.79	0.88	1.36	20	5300	0	100
L1448 IRS 3B	Δ	1.8–2.4	0.7–1.3	3.25–4.35	10–20	4000–7000	0.06–0.12	100
	δ	0.1	0.1	0.05	10	500	0.01	–
	best	2.2	1.1	3.25	10	6500	0.120	100
	mean	2.14	0.96	3.68	14	6300	0.099	100
L1157	Δ	1.5–2.0	0.5–1.5	0.30–1.00	10–30	1000–3000	0.000–0.035	100
	δ	0.1	0.1	0.05	10	500	0.005	–
	best	1.8	0.8	0.55	30	2000	0.015	100
	mean	1.73	0.91	0.59	20	2300	0.019	100
	Δ[h]	1.5–2.0	0.5–1.5	0.30–1.00	10–30	1000–3000	0.015–0.025	100
	mean[h]	1.72	0.91	0.59	20	2300	0.020	100

[a] A central point source flux at $\lambda = 2.7$ mm. Here the point sources are assumed as optically thick indicating $\beta = 0$.

[b] Temperature at $R_0 = 10$ AU

[c] Parameter range searched

[d] Parameter steps

[e] Fixed parameter

[f] Best fitting parameter set with the smallest χ^2_ν

[g] Mean of parameters weighted by the likelihood, $\exp(-\chi^2_\nu/2)$

[h] These two lines present the cases of models with a limited point source flux range. Refer to the text.

Table 2.5 Model parameter sets with β as a function of radius for L1448 IRS 3B.

Targets		p	R_β (AU)	M_T ($M_\odot$)	R_{in} (AU)	R_{out} (AU)	F_{pt} (Jy)	T_0 (K)
L1448 IRS 3B	Δ	2.4–2.8	250–550	2.20–3.20	10	4000–7000	0.00	100
	δ	0.1	50	0.05	–	500	–	–
	best	2.6	400	2.20	10	4500	0.000	100
	mean	2.59	420	2.51	10	5900	0.000	100

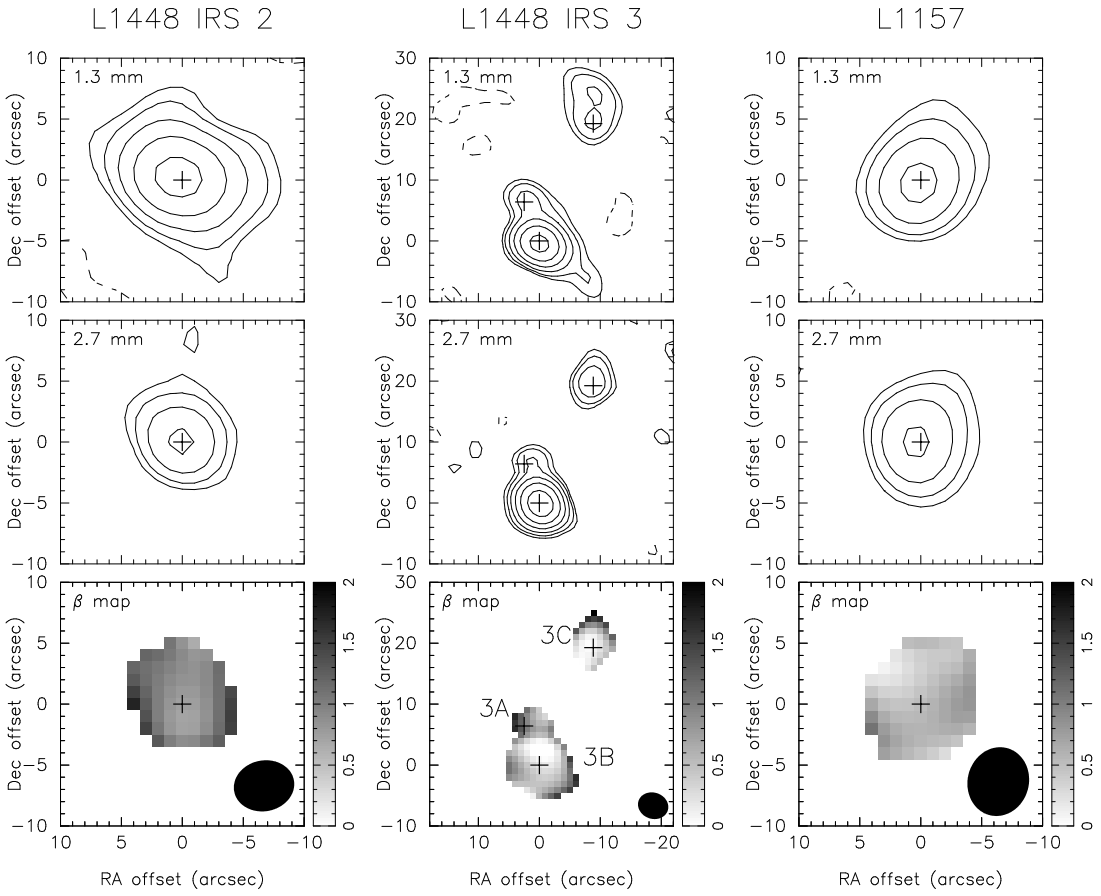

Figure 2.1 Dust continuum in $\lambda = 1.3$ mm and 2.7 mm and dust opacity spectral index (β) maps of L1448 IRS 2, L1448 IRS 3, and L1157. Note that most β values are less than 1. The gray scales are the same in all three maps, although the values are distributed in different ranges. The statistics of the values are in Table 2.3. Synthesized beams are the same in all three maps towards each target (Table 2.2) and plotted on the bottom right of the β maps. The L1448 IRS 3A, 3B, and 3C positions came from Looney et al. (2000) and the $\lambda = 1.3$ mm map of L1448 IRS 3 was re-centered; the pointing center was (RA, Dec) $\approx (-4'', 8'')$. The contours of dust continuum maps are 3, 5, 9, 17, 33, and 65 times $\sigma = 3.4$ and 1.1 mJy beam^{-1} ($\lambda = 1.3$ mm and 2.7 mm maps of L1448 IRS 2), 10 and 1.6 mJy beam^{-1} ($\lambda = 1.3$ mm and 2.7 mm maps of L1448 IRS 3), and 13 and 2.4 mJy beam^{-1} ($\lambda = 1.3$ mm and 2.7 mm maps of L1157).

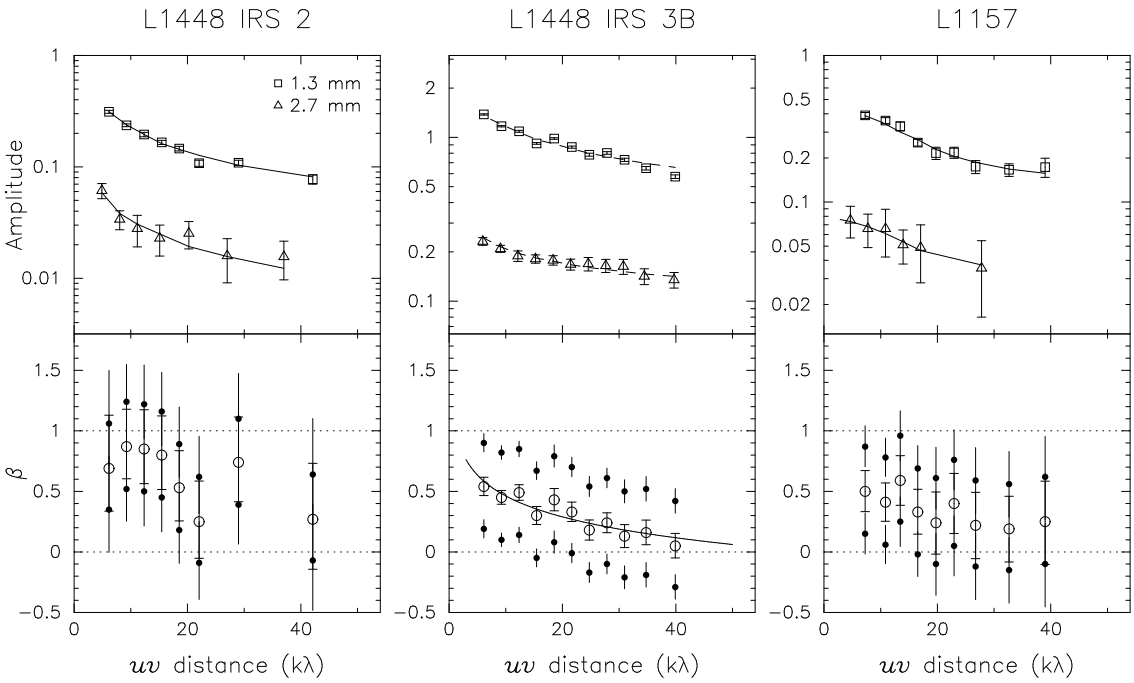

Figure 2.2 Amplitude (upper panels) and dust opacity spectral index β plots (lower panels) of the three targets, L1448 IRS 2, L1448 IRS 3B, and L1157, along uv distance. The open squares present $\lambda = 1.3$ mm data and the open triangles are for $\lambda = 2.7$ mm data. The error bars in the amplitude plots are statistical standard errors of visibilities in each bin. The solid and dashed lines present the best fit models described in Section 2.5 and Figure 2.3. The open circles and error bars with caps in the β plots indicate β values and distribution regions corresponding to the amplitude statistical errors. The filled circles and error bars without caps present cases assuming 15% higher amplitudes at $\lambda = 1.3$ mm and 10% lower amplitudes at $\lambda = 2.7$ mm (resulting in the largest β case within absolute flux calibration uncertainty) and 15% lower at $\lambda = 1.3$ mm and 10% higher at $\lambda = 2.7$ mm (resulting in the smallest β case). The β values are calculated at the uv distance bin centers of the $\lambda = 1.3$ mm data. The visibilities of $\lambda = 2.7$ mm at the positions are interpolated linearly using nearest bin values and in the case of extrapolation the nearest bin values are assumed. The solid line in the β plot of L1448 IRS 3B is a logarithmic fit to the data. Refer to the text for further details.

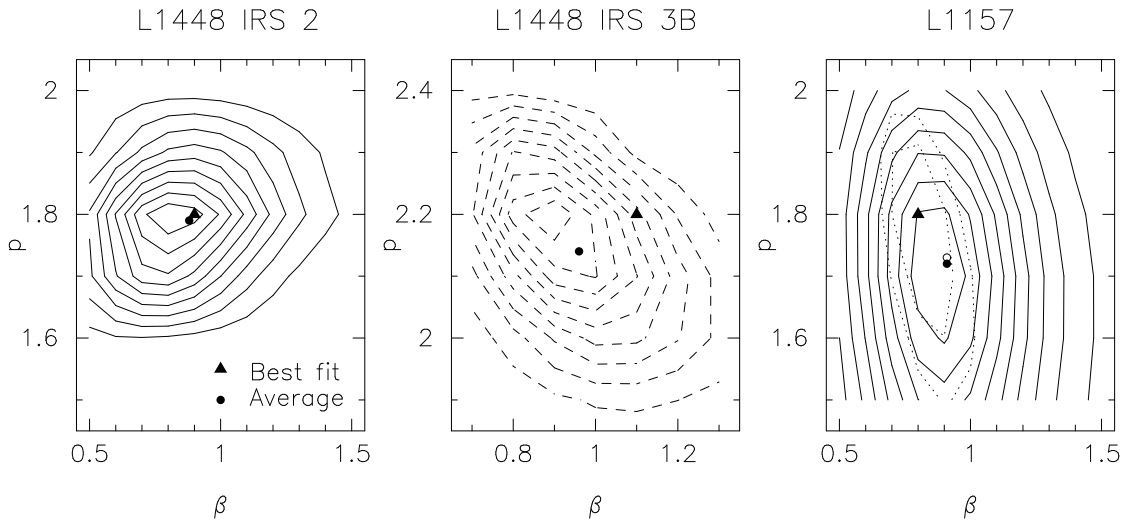

Figure 2.3 Model fitting results of three Class 0 sources in likelihood. The contour levels are from 90% of the peak value with steps of 10%. The triangles mark best fit p and β pairs and circles indicate likelihood weighted averages of p and β, i.e., marginalized p and β. To indicate that the model of L1448 IRS 3B is not the most reliable one in this paper (refer to Section 2.6), its contours are presented by dashed lines. The two dotted contours of L1157 indicate 90% and 80% of the peak likelihood based on all models in the parameter ranges of Table 2.4 and the solid contours are the likelihood distribution obtained from better limited models. Refer to the text for details. In the two cases, the best fit model is identical and the likelihood weighted averages are slightly different.

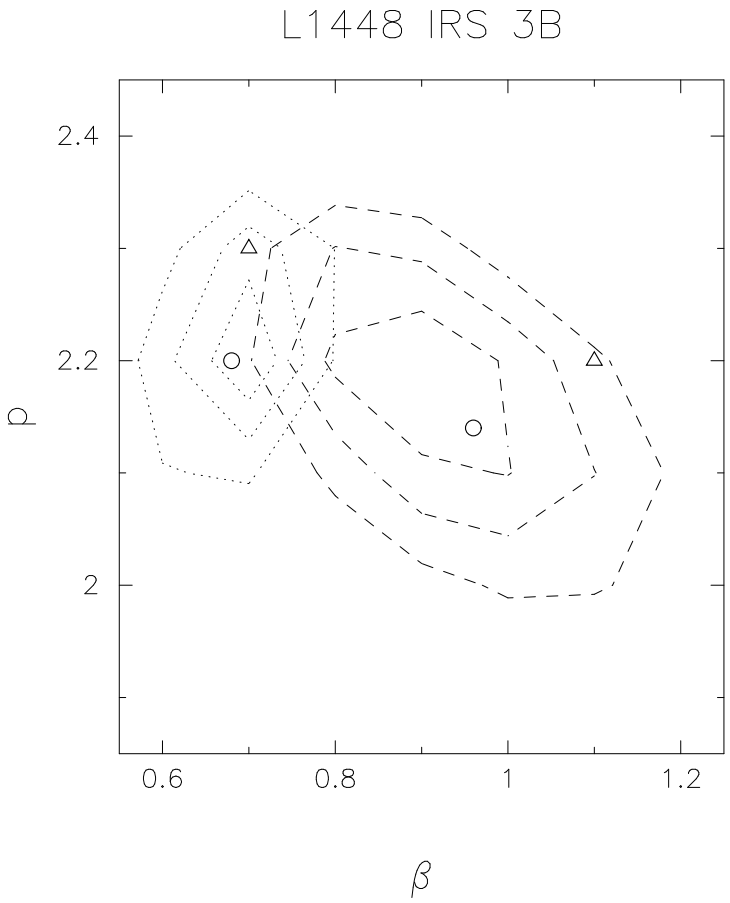

Figure 2.4 Likelihood plots of two cases, (a) dashed contours: model of a black body (optically thick) central point source same in Figure 2.3 and (b) dotted contours: model of a central point source with a β same as the envelope. Triangles presents best fit values and circles indicate likelihood weighted average values. Note that the best model of case (b) gives a worse fit ($\chi^2_\nu \sim 11$) than case (a) ($\chi^2_\nu \sim 8.7$). The contour levels are 80%, 60%, and 40% of each likelihood peak value.

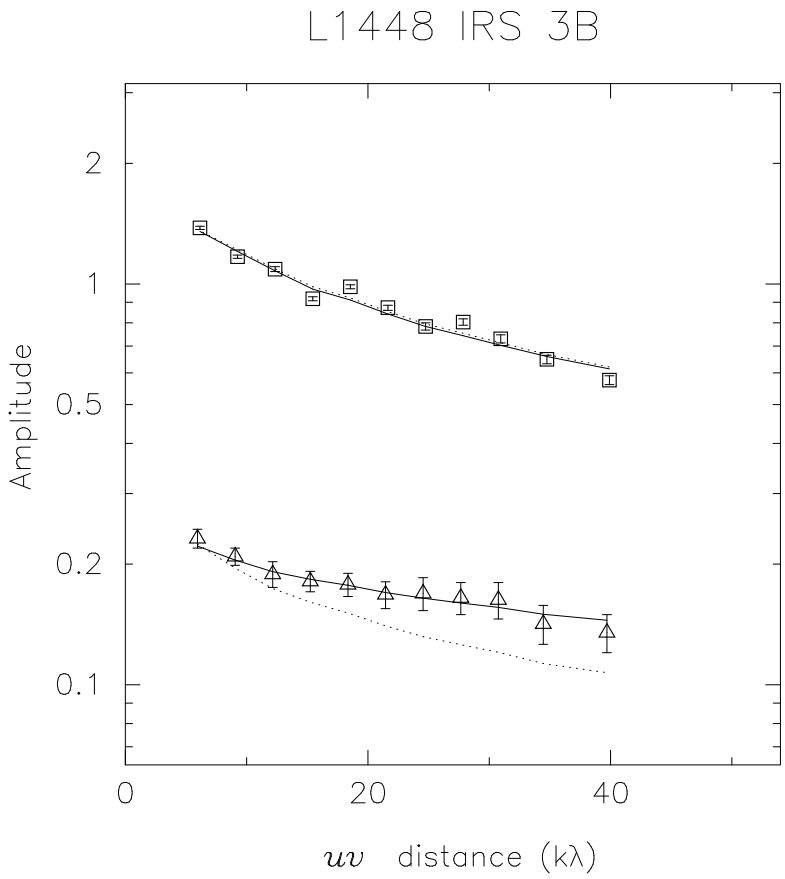

Figure 2.5 Examples of fitting models to emphasize a radial dependence of β. The solid lines are the best fit model with β as a function of radius ($\chi^2_\nu \sim 7.1$) and the dotted lines present an example of fitting models with a constant β. Parameter sets for the best fit model (solid line): $p = 2.6$, $M_T = 2.20$ $M_\odot$, $\beta_{out} = 1.7$, $R_\beta = 400$ AU, $R_{in} = 10$ AU, $R_{out} = 4500$ AU, $F_{pt} = 0.0$ Jy, $T_0 = 100$ K at $R_0 = 10$ AU and for the other one of a constant β (dotted line): $p = 2.5$, $M_T = 2.80$ $M_\odot$, $\beta = 1.0$, $R_{in} = 10$ AU, $R_{out} = 4500$ AU, $F_{pt} = 0.0$ Jy, $T_0 = 100$ K at $R_0 = 10$ AU. Note that the data points are the same as in Figure 2.2 and the error bars are statistical standard errors. No absolute flux calibration uncertainties are shown.

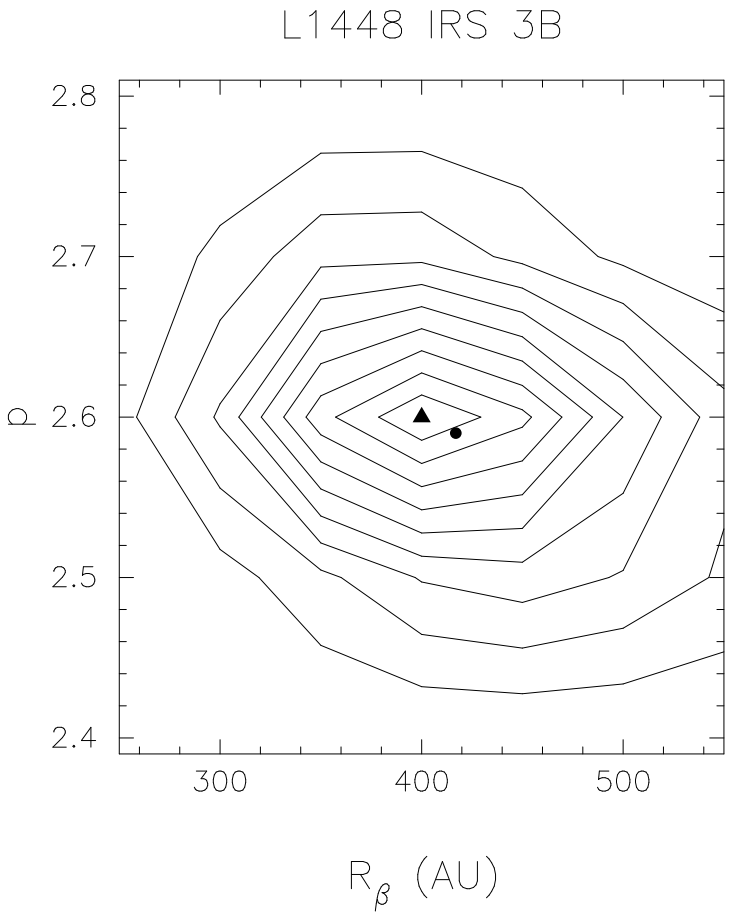

Figure 2.6 Likelihood plot for models with variable β along the envelope radius. R_β is the radius where $\beta = 1.7$ outward. Refer to the text for detailed discussions.

3 Bipolar Outflows

This chapter was published in Kwon et al. (2006).

3.1 Introduction

L1448 is a dark cloud located approximately one degree southwest from NGC 1333 in the Perseus cloud complex at a distance of $\sim$ 250 pc (e.g. Enoch et al., 2006). Three infrared sources were observed by the Infrared Astronomical Satellite (IRAS) and denoted as IRS 1, IRS 2, and IRS 3 by Bachiller & Cernicharo (1986). Due to its brightness in the IRAS bands, IRS 3 has been focused on more than the others. Meanwhile, Bachiller et al. (1990, 1995) revealed a well-collimated, large outflow originating from L1448-mm, located $70''$ southeast of L1448 IRS 3. In fact, IRS 3 is overlapped with the blueshifted lobe of the outflow. Curiel et al. (1990) detected the L1448-mm continuum source and two sources separated by $7''$ in the L1448 IRS 3 region, using the Very Large Array (VLA) at $\lambda = 6$ and 2 cm wavelengths. They named the sources L1448 C (for Center) and L1448 N(A) and N(B) (for North) for L1448-mm and the two sources in IRS 3, respectively. Terebey & Padgett (1997) detected another source $20''$ northwest of the two IRS 3 sources at $\lambda = 2.7$ mm continuum, using the Owens Valley Radio Observatory (OVRO) millimeter interferometer. Looney et al. (2000) resolved all three sources in IRS 3 with high resolution Berkeley Illinois Maryland Association (BIMA) observations at $\lambda = 2.7$ mm continuum. In this paper, we call these sources L1448-mm and L1448 IRS 3A, 3B, and 3C, using IAU nomenclature.

In addition to the multiplicity of young sources in L1448 IRS 3, multiple outflows in the region have been suggested in previous studies. Bachiller et al. (1990, 1995) suggested an outflow originating from IRS 3B, since they detected a redshifted component in the blueshifted lobe of the mm-source outflow and since IRS 3B is the brightest source at mm wavelengths. In contrast, Curiel et al. (1990) suggested that the outflow was driven by IRS 3A, based on a spectral index of 0.2, similar to thermal jet models (e.g. Reynolds, 1986), and coincident H_2O maser observations. Davis & Smith (1995) and Eislöffel (2000) presented H_2 emission images showing shocked regions. They suggested up to three outflows in the IRS 3 region from collimated features in the images. Several Herbig-Haro objects were also detected and explained as outflows driven by the three IRS 3 sources (Bally et al., 1997). Wolf-Chase et al. (2000) suggested two outflows from IRS 3A and 3B, based on previous

studies and their large-scale maps of CO $J = 1 \rightarrow 0$ emission. Moreover, Girart & Acord (2001) reported a well collimated redshifted component detected along a line of position angle 110° from IRS 3B in SiO $J = 2 \rightarrow 1$ emission. These previous studies, however, could not clearly show the outflow features relative to the sources due to a lack of angular resolution and the inherent complexity of the region.

Theoretical studies have suggested that magnetic fields play key roles in the outflows of protostars as well as star formation itself. Observations of magnetic morphology and strength are possible using the Zeeman effect (e.g. Crutcher, 1999) and linear polarization of dust emission and spectral lines (e.g. Girart et al., 1999). Crutcher et al. (2004) recently estimated the magnetic strength as well as morphology, from linear polarization of dust emission in three prestellar cores (starless cores) using the Chandrasekhar-Fermi method (Chandrasekhar & Fermi, 1953). In the case of magnetic fields related to protostars (Class 0 sources) with outflows, Girart et al. (1999) detected linear polarization in the $\lambda = 1.3$ mm dust emission and CO $J = 2 \rightarrow 1$ spectral line. Their study was unique for low mass protostars with outflows.

In this paper, we present polarimetric observations in the $\lambda = 1.3$ mm continuum and CO $J = 2 \rightarrow 1$ showing two outflows and magnetic fields in the L1448 IRS 3 region, using the BIMA array. Moreover, ^{13}CO $J = 1 \rightarrow 0$ and C^{18}O $J = 1 \rightarrow 0$ observation results are presented. We argue that the binary system of L1448 IRS 3A and 3B is gravitationally bound, using these ^{13}CO and C^{18}O observations.

3.2 Observation and Data Reduction

We performed $\lambda = 1.3$ mm continuum and CO $J = 2 \rightarrow 1$ polarimetric observations toward L1448 IRS 3, using nine of the 10 antennas in the BIMA array[1] (Welch et al., 1996). The data were obtained on 2003 October 17, 25, 26, and November 13 in C configuration and integrated for 9 hours except October 17, which was 3 hours due to weather. To get $\lambda = 1.3$ mm continuum data as well as CO $J = 2 \rightarrow 1$ spectral line, a correlator mode with 4 windows of 100 MHz bandwidth each in both sidebands was used. This mode gives ~ 4 km s^{-1} channel width for the CO $J = 2 \rightarrow 1$ spectral line. The first window of the upper side band was centered at the rest frequency of CO $J = 2 \rightarrow 1$, 230.538 GHz. The synthesized beam, obtained through natural weighting, is around $2\farcs5 \times 4\farcs5$.

0237+288 was used as a secondary flux calibrator as well as a phase calibrator; Uranus was the primary flux calibrator. We set the flux of 0237+288 of all data on the value determined from Uranus observed October 25, the best data set. As the 0237+288 flux is

[1]The BIMA Array was operated by the Berkeley Illinois Maryland Association under funding from the National Science Foundation. BIMA has since combined with the Owens Valley Radio Observatory millimeter interferometer, moved to a new higher site, and was recommissioned as the Combined Array for Research in Millimeter-wave Astronomy (CARMA) in 2006.

not variable in such a short period (40 days), it is arguably the most consistent combination of the data. The flux of 0237+288 estimated by the primary flux calibrator is 1.33 Jy; our flux calibration is estimated at a 20% absolute uncertainty.

Each antenna of the BIMA array has a quarter-wave plate in the front of the linearly polarized feed for polarimetric observations. The quarter-wave plate gives left (L) or right (R) circular polarizations and the cross correlations (LL, RR, LR, RL) enable the calculation of the Stokes parameters. To obtain quasi-simultaneous measurements of dual polarizations, antennas switch to measure L or R circular polarization following a fast Walsh function. The data are averaged over the Walsh cycle. The details on the BIMA polarimetric instrument can be found in Rao (1999). In the polarimetry observations, instrumental leakage must be compensated. The leakage terms are $\sim 5\%$ at $\lambda \sim 1$ mm and constant until quarter-wave plates are reinstalled (Rao, 1999; Rao et al., 1998). In addition, they are strongly dependent on frequency. We used 3C279 data observed on 2003 March 4 at the same frequency (230.538 GHz) to get the leakage terms.

MIRIAD (Sault et al., 1995) was used to reduce our data. First, we applied gains obtained from calibrators and constructed models for each observation date. Data of each observation date were self-calibrated with the model constructed from their own data. After combining the individually self-calibrated data, we constructed a combined model. Finally, all data were individually self-calibrated again with this model and combined to the final result.

^{13}CO $J = 1 \rightarrow 0$ ($\nu_{rest} = 110.201$ GHz) and C^{18}O $J = 1 \rightarrow 0$ ($\nu_{rest} = 109.782$ GHz) data were obtained on 2004 April in C configuration of the BIMA array. These two spectral lines were observed simultaneously with a channel width of ~ 1 km s^{-1} and synthesized beam size of $\sim 8'' \times 7''$. Uranus was used as a primary flux calibrator and 0336+323 as a phase calibrator and a secondary flux calibrator. The estimated 0336+323 flux was 1.65 Jy. Again, this flux calibration is estimated at a 20% absolute uncertainty.

Submillimeter continuum observations of L1448 IRS 3 at 850 μm were accessed from the JCMT data archive. They had originally been observed with SCUBA (Holland et al., 1999) on the JCMT on Mauna Kea, during the evenings of 1999 August 28 (6 pointings), 2000 January 3 (7 pointings), and 2000 February 24 (2 pointings). SCUBA was used with the SCUBAPOL (Greaves et al., 2003) polarimeter, which uses a rotating half-wave plate and fixed analyzer. The wave plate is stepped through sixteen positions (each offset from the last by 22.5°) and a Nyquist-sampled image (using a 16-point jiggle pattern) is taken at each wave plate position (Greaves et al., 2003). The observations were carried out while chopping the secondary mirror 120 arcsec in azimuth at 7 Hz and synchronously detecting the signal, thus rejecting sky emission. The integration time per point in the jiggle cycle was 1 second, in each of the left and right telescope beams of the dual-beam chop. The total on-source integration time per complete cycle was 512 seconds. The instrumental polarization

(IP) of each bolometer was measured on the planets Mars and Uranus. This was subtracted from the data before calculating the true source polarization. The mean IP was found to be 0.93±0.27%. The submillimeter zenith opacity for atmospheric extinction removal was determined by comparison with the 1.3-mm sky opacity (Archibald et al., 2002).

3.3 Dust Continuum Emission

Looney et al. (2000) revealed three Class 0 sources in this region in the $\lambda = 2.7$ mm continuum with high resolution BIMA observation and denominated as L1448 IRS 3A, 3B, and 3C (hereafter IRS 3A, 3B, and 3C). Note that some authors used L1448 N(A), N(B), and NW, respectively (Terebey & Padgett, 1997; Barsony et al., 1998). Ciardi et al. (2003) reported a mid-infrared ($10 \sim 25$ μm) observation of IRS 3A and 3B. They suggested that IRS 3A and 3B are Class I and Class 0 sources respectively, based on a comparison of the envelope and central source masses. On one hand, IRS 3A and 3B could be a "coeval" binary system with different central masses and so be evolving at different rates. On the other, they may be evolving at a same rate under different environments due to interaction, a mass flow from one to the other. Although we do not focus on distinguishing the two cases, we discuss the binarity (i.e. if the two sources are gravitationally bound) later, which is a basis for the two ideas.

Figure 3.1 shows the observed $\lambda = 1.3$ mm continuum image. IRS 3A and 3B are distinct, but IRS 3C is marginally detected. The vectors in Figure 3.1 indicate the linear polarization direction, which will be discussed in Section 3.7. The locations of IRS 3A, 3B, and 3C in Figure 3.1 are from Looney et al. (2000). Table 3.1 summarizes locations, fluxes, and estimated masses of the three sources. To estimate the mass of the circumstellar material (envelopes and disks), we assume optically thin dust emission and a uniform envelope dust temperature of 35 K,

$$F_\nu = B_\nu(T_{dust})\ \kappa_\nu\ M_{tot}\ D^{-2} \tag{3.1}$$

where B_ν is a black-body intensity of a temperature T_{dust}, κ_ν is a mass absorption coefficient, M_{tot} is the total mass of gas and dust, and D is the source distance. We assume a mass absorption coefficient, $\kappa_\nu = 0.005$ cm^2 g^{-1} at $\lambda = 1.3$ mm. The mass absorption coefficient was acquired following a dust emissivity model of a power law ($\kappa_\nu \sim \lambda^{-\beta}$) with $\beta = 1$. Dust emissivity studies of submillimeter wavelengths suggested λ^{-1} dependence in circumstellar disks and dense cores rather than λ^{-2} (Weintraub et al., 1989; Beckwith et al., 1990; Beckwith & Sargent, 1991; Looney et al., 2003).

3.4 ^{13}CO $J = 1 \rightarrow 0$ and C^{18}O $J = 1 \rightarrow 0$ Observation

We detect all three sources (IRS 3A, 3B, and 3C) in ^{13}CO and C^{18}O. Figures 3.2 and 3.3 show the ^{13}CO $J = 1 \rightarrow 0$ and C^{18}O $J = 1 \rightarrow 0$ channel maps, respectively. IRS 3C peaks are in the 3.8 km s^{-1} channel of ^{13}CO and 3.7 km s^{-1} channel of C^{18}O. The emission from IRS 3A and 3B is distributed over different velocity channels; IRS 3A is around the 5 and 6 km s^{-1} channels in the two spectral lines, while IRS 3B is around the 4 and 5 km s^{-1} channels. This implies that the envelopes of IRS 3A and 3B have a velocity difference less than 1 km s^{-1}. Terebey & Padgett (1997) have reported a velocity-position diagram of C^{18}O $J = 1 \rightarrow 0$ with a comparable angular and spectral resolution to ours, showing these velocity differences between IRS 3A, 3B, and 3C. They suggested kinematics of the binary system IRS 3A and 3B, as well as a rotating system consisting of IRS 3C and the common envelope of IRS 3A and 3B. However, they did not discuss the physical conditions of the presumed binary system. We discuss the binary system of IRS 3A and 3B in Section 3.6, based on their velocity difference and the two outflows shown in the following section. Moreover, we estimate the specific angular momentum of the binary system.

Isotopic observations such as ^{13}CO and C^{18}O are used to trace denser regions and to verify their optical depth. However, we do not follow the standard procedure because the masses of envelopes are better estimated using our dust emission data, especially in the case of complicated regions like IRS 3. Also, these isotopes may not trace outflows. Instead, we use the optical depth results of Bachiller et al. (1990), deduced from CO $J = 1 \rightarrow 0$ and CO $J = 2 \rightarrow 1$, and follow their procedures to estimate the outflow masses in Section 3.5.2.

3.5 CO $J = 2 \rightarrow 1$ Observation

3.5.1 Bipolar Outflows

As introduced in Section 3.1, one, two, or up to three outflows have been suggested for this region. Bachiller et al. (1990) proposed that an outflow in the east-west direction originates from IRS 3, based on a redshifted component that was detected in the region of the blueshifted lobe of the mm source outflow. Recently Wolf-Chase et al. (2000) suggested outflows of position angle 150° and 129° from IRS 3A and 3B respectively, using their large-scale CO $J = 1 \rightarrow 0$ observation as well as previous studies of H_2 observations and Herbig-Haro objects. In addition, Girart & Acord (2001) presented a redshifted SiO component along a line of position angle of 110° from IRS 3B. However, to date there were no observations with enough angular resolution to clearly identify outflows with sources. Here we present high angular resolution BIMA observations to illustrate outflows in IRS 3. We reveal two outflows from IRS 3A and 3B but no outflow from IRS 3C, based on channel maps and integrated intensity maps.

Figure 3.4 shows the CO $J = 2 \rightarrow 1$ channel maps with a velocity range from +29 to −36 km s^{-1}. The values in the upper left of each panel indicate the channel central velocities in units of km s^{-1} and the two lines in each panel show our determined directions of the two outflows originating from IRS 3A and 3B. As introduced in Section 3.4, the V_{LSR} of these sources is around 5 km s^{-1}, which is located at the boundary between the +7 and +3 km s^{-1} channels.

The outflow of IRS 3A is mainly shown in two channels around V_{LSR}, +7 and +3 km s^{-1} channels, with symmetric features cross the central source. Some redshifted components of the IRS 3A outflow also appear in the +15 and +11 km s^{-1} channels. The feature might be just an elongated cloud. However, the ^{13}CO and C^{18}O maps indicating ambient clouds do not show such features. In addition, the facts that two channels of +7 and +3 km s^{-1} show a very similar shape to each other, that two redshifted channels of +15 and +11 km s^{-1} have blobs on both sides of IRS 3A, and that H_2 emission observations reveal a string of H_2 knots in a consistent direction (Davis & Smith, 1995; Eislöffel, 2000), strongly suggest that it is an outflow nearly perpendicular to the line of sight, originating from IRS 3A. The position angle of the IRS 3A outflow is 155°.

As shown in Figure 3.4, the outflow from IRS 3B appears from the +23 km s^{-1} channel, an end channel of a redshifted lobe, along the position angle of 105°. This position angle is consistent with the Girart & Acord (2001) estimate of 110°. The redshifted lobe is clearly seen from the +23 to +11 km s^{-1} channels and overlaps with the southern lobe originating from IRS 3A in the +7 and +3 km s^{-1} channels. Note that the blueshifted channels after +3 km s^{-1} look complicated with many blobs. This can be explained by the overlap with the blueshifted lobe of the mm source outflow, located 70″ southeast. Indeed, the velocity range of the mm source's blueshifted outflow lobe is consistent with these channels (see Figure 10 in Bachiller et al., 1990). Due to the complexity in blueshifted channels, the outflow direction is deduced from the redshifted channels first. However, we can still see the blueshifted components of the IRS 3B outflow up to −30 km s^{-1} along the 105° position angle. In addition, a string of three blobs along the outflow direction is shown in the −5.2 km s^{-1} channel. The blobs in the +15 and +11 km s^{-1} channels can be the opposite components of these three blobs.

Figure 3.5 is an integrated intensity map of CO $J = 2 \rightarrow 1$ that more clearly shows the outflows. The red contours present a velocity range from +25 to +9 km s^{-1}, black contours from +9 to +1 km s^{-1}, and blue contours from +1 to −32 km s^{-1}. Again, the blue contours appear with several blobs due to the effect of the overlapped blueshifted lobe of the mm source outflow. This integrated intensity map confirms two outflows originating from IRS 3A and 3B as suggested from channel maps. Black contours in Figure 3.5 show an outflow from IRS 3A and especially the redshifted and blueshifted lobes around IRS 3B are clearly seen.

3.5.2 Mass, Momentum, and Energy

Bachiller et al. (1990) showed that the outflow regions in IRS 3 are optically thin in CO, using CO $J = 2 \rightarrow 1$ and $J = 1 \rightarrow 0$ lines instead of the CO isotopes ^{13}CO or C^{18}O, since the outflow regions are not dense enough to be traced by these isotopic observations. In addition, they estimated the excitation temperature of CO. As described in Bachiller et al. (1990), the CO column density can be estimated from the integrated intensity, assuming optically thin emission and level populations in local thermal equilibrium at the excitation temperature T_{21},

$$\frac{N(CO)}{cm^{-2}} = 1.06 \times 10^{13}\ T_{21}\ exp(16.5/T_{21}) \int T_R(2-1)\ d\Big(\frac{v}{km\ s^{-1}}\Big). \tag{3.2}$$

To estimate the masses of the lobes, we assume a typical abundance of CO, CO/H_2 = x(CO) $\sim 10^{-4}$, optically thin CO emission in outflow regions, and a CO excitation temperature of 11 K, as reported by Bachiller et al. (1990). These assumptions give the mass estimate equation,

$$\begin{aligned} M_{lobe} &= 2m_H\ A_{lobe}\ 10^4\ N(CO) \\ &= 2m_H\ 5.23 \times 10^{-5}\ \frac{\lambda^2 D^2}{2k} \int \frac{F_{lobe}(CO\ 2-1)}{Jy}\ d\Big(\frac{v}{km\ s^{-1}}\Big) \\ &= 3.22 \times 10^{-6}\ \mathrm{M}_\odot \Big(\frac{D}{250\ pc}\Big)^2 \int \frac{F_{lobe}(CO\ 2-1)}{Jy}\ d\Big(\frac{v}{km\ s^{-1}}\Big) \end{aligned} \tag{3.3}$$

where $A_{lobe} = \Omega D^2$ is the lobe area and F_{lobe} is the total lobe flux density. The mass estimates are summarized in Table 3.2 with momentum and kinetic energy. Note that the errors tabulated are only statistical errors. Moreover, important uncertainties like CO opacities and unknown 3-D geometry of outflows affect these outflow mass estimates (Lada, 1985; Bachiller et al., 1990). In the case of the blueshifted lobes, there is also the uncertainty from the contribution of the mm source outflow.

We also need to consider that interferometric observations resolve out flux from extended structures. The missing flux makes mass estimates of extended structures difficult and underestimated. On the other hand, interferometry is a powerful technique that can reveal small structures overlapped with large-scale emission. In this case, L1448 IRS 3 is overlapped with the large blueshifted lobe of the L1448-mm outflow. Therefore, we have the advantage of minimizing the L1448-mm outflow contamination as well as the disadvantage of losing the flux of extended features. The *uv* coverage of our observations allows us to recover flux up to 15″ structures. The missing flux is less significant in elongated structures because it also depends on the size-scales of the minor axis.

Compared to the single dish observations (beam size $\sim 12''$) of Bachiller et al. (1990), there is no significant missing flux in the redshifted wing ($\gtrsim 10$ km s^{-1}); the flux is consistent

within the uncertainties. The low velocity components (0 to 10 km s^{-1}) are dominated by the ambient cloud (Bachiller et al., 1990). Since our two channels in that velocity range still show outflow features consistent with the redshifted channels (see Figure 3.4), we argue that the majority of missing flux comes from the ambient cloud emission. From this point of view, the missing flux is a large advantage as it avoids contamination with the ambient cloud emission rather than the disadvantage of losing flux. On the other hand, the channel with -1.1 km s^{-1} central velocity may experience relatively large flux loss, as the IRS 3B outflow feature disappears or is indistinct from the extended, and mostly resolved-out, blueshifted lobe of the L1448-mm source. The missing flux in this channel would cause an underestimation of the IRS 3B outflow mass but does not significantly affect our interpretations. We discuss the effects caused by the missing flux in this channel later in related sections. Overall, although the true size of the emission is unknown, we conclude that the missing flux probably does not significantly affect our results.

We estimate the masses of the northern and the southern lobes of the IRS 3A outflow as 0.70×10^{-3} and 1.12×10^{-3} $M_\odot$, respectively. Considering that the southern lobe is overlapped with a portion of a redshifted lobe of an outflow from IRS 3B, we can regard 0.42×10^{-3} $M_\odot$ (the mass difference of the two lobes) as coming from IRS 3B. This assumes that the two lobes from an outflow have similar masses. As a result, the northern and the southern lobes of IRS 3A outflow have $\sim 0.70 \times 10^{-3}$ $M_\odot$ each.

The redshifted and blueshifted lobes of the outflow originating from IRS 3B are well distinguished in the velocity range +25 to -32 km s^{-1}. The outflow spans the blue, black, and red contours in Figure 3.5. The blueshifted lobe of this outflow has 0.98×10^{-3} $M_\odot$, which is comparable to the 0.75×10^{-3} $M_\odot$ of the redshifted lobe as a combination of the red contours (0.33×10^{-3} $M_\odot$) and a portion of the black contours (0.42×10^{-3} $M_\odot$). The difference is reasonable, considering the blueshifted regions are contaminated by components of the mm source outflow, probable flux loss in the -1.1 km s^{-1} channel, and flux gain in other blueshifted channels. In summary, the redshifted lobe of the IRS 3B outflow has 0.75×10^{-3} $M_\odot$ and the blueshifted lobe has 0.98×10^{-3} $M_\odot$, comparable within the uncertainties.

Estimates of momentum and kinetic energy of each component are also shown in Table 3.2. We use $V_{LSR} = 5$ km s^{-1} and do not apply the inclination factors, which are $1/cos\theta$ for momentum and $1/cos^2\theta$ for kinetic energy. Here θ is the inclination angle from the line of sight. When calculating the momentum and kinetic energy, we assume that components in each channel have the central channel velocity. Comparing momentum and energy of each lobe of the two outflows, the southern lobe of the IRS 3A outflow and the eastern lobe of the IRS 3B outflow have lower momentum and kinetic energy than their opposite lobes. Although the contamination of the L1448-mm outflow in the blueshifted lobe of the IRS 3B outflow and the nearly perpendicular aspect of the IRS 3A outflow to the line of

sight make the interpretation difficult, it is probable that the outflows from IRS 3A and 3B interact in the overlapped region because the kinetic energy difference is distinct even when considering a portion of the blueshifted lobe of IRS 3B to be the same mass as the redshifted lobe. Due to the collision of two outflows, the kinetic energy would be reduced. The fact that there is no blueshifted opponent of the small redshifted blobs of the IRS 3A outflow in the +15 km s^{-1} channel supports this idea as well. Besides, the heated clump, which Curiel et al. (1999) presented near IRS 3 in observations of the NH_3 $(J, K) = (1, 1)$ and $(2, 2)$ inversion transitions, is located in the overlapped region of the two outflows from IRS 3A and 3B. Although they argued that the heated clump would be a part of a larger heated region because IRS 3 is at the edge of their field, it may present the interaction of the two outflows. In addition, the fact that the redshifted component of the IRS 3B outflow detected in SiO $J = 2 \rightarrow 1$ over the interaction region has relatively low velocity compared to the blueshifted component (Girart & Acord, 2001), also supports interaction. Based on these considerations, we also suggest that IRS 3B is closer than IRS 3A because this deployment can reproduce the interaction. This is pointed out again later, in the CO $J = 2 \rightarrow 1$ linear polarization of Section 3.7.

3.5.3 Velocity, Inclination, and Opening

Based on the mass of the outflow lobes and an assumed mass loss rate, we can check whether or not the IRS 3A outflow is nearly perpendicular. If we assume a mass loss rate of 6×10^{-7} M$_\odot$ yr^{-1} from the two outflow lobes[2], the age of the outflow would be $\sim$ 2300 years and the proper velocity of the outflow would be $\sim$ 10 km s^{-1} since the outflows extend to 20″ (5000 AU at 250 pc). As the channel width is 4 km s^{-1} and the V_{LSR} is on the boundary of the two channels showing the outflow feature, the inclination including opening angle must be less than 22° from the plane of the sky; the IRS 3A outflow is nearly perpendicular to the line of sight.

The inclination angle of IRS 3B can be estimated from the velocity features detected. Figure 3.6 presents a velocity-position diagram cut along the outflow direction of position angle 105° from IRS 3B. Both redshifted (east) and blueshifted (west) lobes are divided into two components: one accelerating from the source and the other with a constant velocity. Using Figures 3.6 and 3.4, the accelerating portion up to +23 km s^{-1} (channel central velocity) and the constant part at +3 km s^{-1} are in the eastern (redshifted) region. Similarly, the accelerating portion up to −30 km s^{-1} and the constant part at −5 km s^{-1} are in the western (blueshifted) region. These velocities are +18, −2, −10, and −35 km s^{-1}

[2]This is consistent with previous studies suggesting that massive young stars lose mass up to 10^{-3} M$_\odot$ yr^{-1} and low mass stars down to 10^{-9} M$_\odot$ yr^{-1} (e.g. Kim & Kurtz, 2006; Wu et al., 2004; Bontemps et al., 1996). In order to obtain a reasonable outflow velocity ($\sim$ 10 km s^{-1}), we assume a mass loss rate of 6×10^{-7} M$_\odot$ yr^{-1}.

in the IRS 3B rest frame ($V_{LSR} = +5$ km s^{-1}). If the missing flux in the -1.1 km s^{-1} channel is part of the constant component, then arguable -6 km s^{-1} in the IRS 3B rest frame is a better extreme constant velocity. However, since the small difference in velocity will not significantly change the results derived below and since it is strongly dependent on the assumed missing flux, we use -10 km s^{-1} in the IRS 3B rest frame as the velocity of the constant velocity component in blueshifted region.

The constant and accelerating features are best explained by two possible geometric outflow effects, although an outflow with various velocity components is also a possible explanation. One is the geometric effect caused by precession and the other by a trumpet-shaped outflow. The precession of the IRS 3B outflow– the side of the redshifted lobe is precessing toward the observer and the side of the blueshifted lobe is away from the observer, would give the detected map features. In other words, the redshifted or blueshifted components further from the central source are older components emitted when the inclination was smaller than now. Therefore, the outflow is observed as accelerating away from the source, even assuming a constant outflow velocity. A trumpet-shaped outflow can also give the detected features. The "trumpet" outflow has different angles with respect to the line of sight along the redshifted or blueshifted lobes. These different angles can give the accelerating feature depending on the outflow inclination.

The nice aspect of the "trumpet" outflow is that we can estimate outflow parameters such as velocity, inclination angle, and opening angle, based on the observed data. The opening angle is assumed as the angle on the end of the outflow "trumpet". Therefore, the velocity difference between accelerating and non-accelerating features of the redshifted or blueshifted lobe is coming from the opening angle. In addition to the velocity (v), the inclination angle (θ_i), and the opening angle (θ_o), we adopt the velocity difference (Δv) and the opening angle difference ($\Delta\theta_o$) between the redshifted and blueshifted lobes. Note that the inclination angle is measured from the line of sight and that the opening angle is half of the outflow opening. As mentioned in the previous section, since the redshifted lobe of the IRS 3B outflow is likely to be interacting with the southern lobe of the IRS 3A outflow, a velocity difference needs to be included. The reason for applying the opening angle difference is that the side of the redshifted lobe has components in a blueshifted channel with a central velocity of $+3$ km s^{-1} (Figure 3.4), while the side of the blueshifted lobe does not. We define the velocity difference as $\Delta v = v_{blue} - v_{red} > 0$ ($v = v_{blue}$) and the opening angle difference as $\Delta\theta_o = \theta_{o,red} - \theta_{o,blue} > 0$ ($\theta_o = \theta_{o,blue}$). The blueshifted lobe is expected to have a higher velocity and a narrower opening angle than the redshifted lobe. Using Bayesian statistics, we determine the most likely parameter combinations to explain

the observed velocity features,

$$P(\{parameters\}|\{v_i'\}) = \frac{P(\{v_i'\}|\{parameters\})}{P(\{v_i'\})} P(\{parameters\}),$$
$$\text{where} \quad \{parameters\} = \{v,\ \theta_i,\ \theta_o,\ \Delta v,\ \Delta\theta_o\}. \tag{3.4}$$

The $\{v_i'\}$ is a set of four extreme values of the observed line-of-sight velocities in the outflow lobes with respect to the IRS 3B rest frame (v_1, v_2, v_3, and v_4). Since it is a fitting of a model, the evidence term $P(\{v_i'\})$ is just a normalization factor. In addition, since we do not have any preference to choose the five parameters, we assume that the prior probability densities, $P(\{parameters\})$, are uniform. However, note that the opening angle should be less than 45°; otherwise, we would observe redshifted components on the side of the blueshifted lobe as well as the blueshifted components on the side of the redshifted lobe. For the likelihood, $P(\{v_i'\}|\{parameters\})$, we choose a probability density having a constant value in the channel width (4 km s^{-1}) and exponentially decreasing outside of the channel width.

We found the parameters giving the maximum posterior probability, after taking into account central velocities of four-end channels showing outflow features in the IRS 3B rest frame, $\{v_i'\} = \{+18, -2, -10, -35\}$ km s^{-1}. The maximum posterior is obtained when the four velocities estimated from the five parameters are in the flat-top regions of each channel. Note that we adopted the likelihood (indicating channels) of functions having a constant value (flat-top) in the channel width (4 km s^{-1}) and exponentially decreasing outside. To explore the parameter space, the Metropolis-Hastings method (MacKay, 2003) was used; we obtained a few hundred thousand samples with the maximum posterior probability through one million trials. Since we use flat-top shaped channel functions for the likelihood, the parameters are widely distributed. For example, the velocity distribution peaks at around 40 km s^{-1} and quickly drops, but some cases have even a few hundred km s^{-1}. The inclination angle and the opening angle are distributed in $30 \sim 80°$ and $5 \sim 45°$, respectively.

However, as these parameters are not independent of each other, we can narrow the acceptable range of parameters. Figure 3.7 shows the velocity (solid circles), the inclination angle (solid squares), and the velocity and opening angle differences (open circles and open triangles, respectively) versus the opening angle. The opening angle is also plotted (solid triangles) to compare with the other parameters. For the plot, samples are divided by 5° bins of the opening angle and each bin has a few tens of thousand samples. The data points in Figure 3.7 are average values of the samples in each bin, and the error bars present their standard deviation. The dotted line without data points indicates the opening angle plus the opening angle difference, in other words, the redshifted opening angle. Note that small opening angles with relatively large velocities and inclination angles or large

opening angles with small velocities and inclination angles give the four observed line-of-sight velocities. However, opening angles larger than 26° are rejected because they have the 18 km s^{-1} component with the -10 km s^{-1} component on the same side, which is not consistent with our observation (Figure 3.6). Too small opening angles ($< 8°$) are also not likely due to the too large velocities required. As a result, we can constrain the opening angle to $8° < \theta_o < 26°$ and the other parameters to the values following the opening angle; for examples, $100 \gtrsim v \gtrsim 40$ km s^{-1} and $75° \gtrsim \theta_i \gtrsim 50°$. Recent Spitzer Space Telescope (SST) observations have suggested that an opening angle of $\sim 20°$ is preferred (Tobin et al., 2007). In that case, we constrain the inclination angle to $\sim 57°$, which is consistent with the SST observational results within uncertainties, and the velocity to ~ 45 km s^{-1}. These parameters give the age of the IRS 3B outflow detected in our field-of-view as ~ 600 years.

3.6 Binary System of IRS 3A and 3B

The velocity difference between IRS 3A and 3B detected in the ^{13}CO $J = 1 \rightarrow 0$ and C^{18}O $J = 1 \rightarrow 0$ observations can be understood as an orbiting binary system. This also supports the interaction of the two outflows from IRS 3A and 3B. Here we introduce a kinematical constraint for a Class 0 binary system.

When denominating velocities of the two clouds with respect to the center of mass of the binary system as v_A (> 0) and v_B (< 0) and the components of the velocities in the line-of-sight plane of the IRS 3A and 3B as $v_{A\parallel}$ and $v_{B\parallel}$, the projected velocities on the line of sight are $v'_A = v_{A\parallel} sin\theta$ and $v'_B = v_{B\parallel} sin\theta$ (Figure 3.8). Note that the vertical velocity components to the plane are $v_{A\perp}$ and $v_{B\perp}$, and so the proper motion velocities are indicated as $(v^2_{A\parallel} cos^2\theta + v^2_{A\perp})^{1/2}$ and $(v^2_{B\parallel} cos^2\theta + v^2_{B\perp})^{1/2}$. Similarly, the projected semimajor axis is $a' = a sin\theta \approx 7'' \times 250$ pc $= 1750$ AU. These projected velocity difference (here assuming 0.8 km s^{-1}) and the projected semimajor axis (~ 1750 AU) allow the estimation of the orbiting period (P) of the binary system,

$$
\begin{aligned}
|v_A| = \sqrt{v^2_{A\parallel} + v^2_{A\perp}} = \frac{2\pi a_A}{P} &> |v_{A\parallel}| \\
|v_B| = \sqrt{v^2_{B\parallel} + v^2_{B\perp}} = \frac{2\pi a_B}{P} &> |v_{B\parallel}|.
\end{aligned}
$$

Multiplying by $sin\theta$, they become

$$
\begin{aligned}
|v_{A\parallel}| sin\theta &< \frac{2\pi a_A sin\theta}{P} \\
|v_{B\parallel}| sin\theta &< \frac{2\pi a_B sin\theta}{P}
\end{aligned}
$$

and adding each side gives

$$|v'_A| + |v'_B| < \frac{2\pi a'}{P}. \tag{3.5}$$

In Equation (3.5), since v'_B is negative, the left hand side is the projected velocity difference, 0.8 km s^{-1}. Using the projected semimajor axis (1750 AU), we obtain an upper limit of the orbiting period, $\sim 6.54 \times 10^4$ years. Note that it is much longer than the age ($\sim$ 2300 years) of the IRS 3A outflow, which is obtained assuming the mass loss rate, and the estimated age ($\sim$ 600 years) of the IRS 3B outflow. Furthermore, since the masses of the two clouds were estimated as 0.21 and 1.15 M$_\odot$ in Section 3.3 and Table 3.1, we can also estimate an upper limit of the semimajor axis from the Kepler's third law,

$$\frac{a}{AU} = \left(\left(\frac{m_A + m_B}{\mathrm{M}_\odot} \right) \left(\frac{P}{yr} \right)^2 \right)^{1/3}. \tag{3.6}$$

The estimated masses and the orbiting period give a semimajor axis of $\sim$ 1800 AU, a slightly larger value than the projected semimajor axis. In this case, the $\theta = sin^{-1}(a'/a)$ is about 76° (refer to Figure 3.8), which means that the considered velocity difference (0.8 km s^{-1}) is acceptable for a gravitationally bound binary system. Note that the unconsidered central luminous sources can increase the semimajor axis by 26% ($= 2^{1/3}$) when they are assumed to have identical masses to the circumstellar material. This increases the probability of a gravitationally bound binary system. If the velocity difference were estimated as 0.5 km s^{-1} from higher spectral resolution observations, the upper limit of the orbiting period would be 1.05×10^5 years, the semimajor axis would be 2500 AU, and the $\theta = sin^{-1}(a'/a)$ would be 44°. As described above, the total mass and the projected velocity difference and semimajor axis give a kinematical, gravitationally bound constraint on apparent binary systems. Since the projected velocity difference is within values for a binary system, we conclude that the IRS 3A and 3B sources are likely to be gravitationally bound. Observations with higher spectral resolution will give a better constraint.

The angular momentum of the binary system is also noteworthy. We estimate the specific angular momentum (angular momentum per unit mass) of this binary system using the projected velocity components, the projected distance, and the mass ratio from the mass estimates of the continuum emission at $\lambda = 1.3$ mm. This estimate has uncertainties caused by the ambiguities of velocities of the line of sight as well as proper motions. The ambiguity of the line of sight comes from the broad channel width of our observation. If we can remove the ambiguity using higher spectral resolution observation, the estimate would be a lower limit of the specific angular momentum. The value is $\sim 3 \times 10^{20}$ cm^2 s^{-1}, similar to the upper limit of the specific angular momentum of binary stars in Taurus and to the lower limit of molecular cloud cores (Simon et al., 1995; Goodman et al., 1993).

3.7 Magnetic Fields

Linear polarization is marginally detected in both the $\lambda = 1.3$ mm continuum and CO $J = 2 \rightarrow 1$ spectral line. Vectors around IRS 3B in Figure 3.1 present polarization detected in the $\lambda = 1.3$ mm continuum. Since polarization of dust emission is perpendicular to the magnetic field, the magnetic field is expected in the north-south direction around IRS 3B. This is consistent with the large scale magnetic field observed by SCUBA at $\lambda = 850$ μm shown in Figure 3.9. Note that the vectors in Figure 3.9 also indicate linear polarization and the direction around IRS 3B is east-west like the $\lambda = 1.3$ mm continuum data in Figure 3.1. Toward the center of IRS 3B, weaker linear polarization is detected at both wavelengths. The polarization fractions are around 5% in our BIMA 1.3 mm continuum and around 2% in the SCUBA data. This smaller polarization fraction of the SCUBA data is from the larger beam size of SCUBA smearing out the linear polarization.

Linear polarization of the CO $J = 2 \rightarrow 1$ emission, tracing the outflows, was detected in patches of the overlapped region of the southern lobe of the IRS 3A outflow and the redshifted lobe of the IRS 3B outflow. Figure 3.10 is an intensity map of two channels combined in velocity from +1 to +9 km s^{-1}. Vectors present linear polarization directions and two lines on IRS 3A and 3B indicate outflow directions. According to the Goldreich-Kylafis effect (e.g. Kylafis, 1983), linear polarization of spectral lines can be either parallel or perpendicular to magnetic field, depending on the relation between line of sight, magnetic field direction, and velocity gradient. Since the polarization was detected in only a few small patches located in the overlapped region of the IRS 3A and 3B outflows, it is hard to define the morphology of the magnetic fields. However, as the vectors are likely parallel or perpendicular to the IRS 3B outflow, we suggest that the polarization comes from the IRS 3B outflow. At the same time, this suggestion implies that the magnetic field may be perpendicular or parallel to the outflow[3]. Although we cannot distinguish between the two, the parallel magnetic field can be from a large scale magnetic field morphology (hour glass morphology) widely accepted in forming protostars, and the perpendicular magnetic field can be from a helical structure extended from a toroidal magnetic field suggested by some theories (e.g. Ostriker, 1997). The fraction of linear polarization is around 6 to 15%.

Based on both dust polarization and CO $J = 2 \rightarrow 1$ polarization, we suggest a unified magnetic field morphology related to the disk and outflow structures in forming protostars.

[3]Girart et al. (1999) detected CO $J = 2 \rightarrow 1$ polarization perpendicular to dust polarization in NGC 1333 IRAS 4A and interpreted the spectral line polarization as parallel to the magnetic field. However, polarization in dust continuum and CO $J = 2 \rightarrow 1$ may not indicate the same magnetic field because dust continuum and CO $J = 2 \rightarrow 1$ trace different density regions; the magnetic field direction at the central core may change radially from an hour glass morphology (e.g. Fiedler & Mouschovias, 1993). In addition, detected polarization directions in our dust emission and CO $J = 2 \rightarrow 1$ data are likely to be parallel around the IRS 3B center. Therefore, we cannot define the magnetic field direction as either perpendicular or parallel to the CO $J = 2 \rightarrow 1$ polarization here.

The magnetic field inferred from the dust emission, perpendicular to outflow, may show a toroidal magnetic field around a circumstellar disk and the magnetic field inferred from CO $J = 2 \rightarrow 1$ may present a large scale morphology parallel to the outflow or helical structure perpendicular to the outflow. As discussed in Section 3.5, we can also suggest that the IRS 3B source is closer, because the polarization appears to be from IRS 3B. Polarization of the farther source (IRS 3A) is harder to detect due to the foreground cloud (IRS 3B).

3.8 Summary and Discussion

We present CO $J = 2 \rightarrow 1$, ^{13}CO $J = 1 \rightarrow 0$ and C^{18}O $J = 1 \rightarrow 0$ observations, and $\lambda = 1.3$ mm continuum and CO $J = 2 \rightarrow 1$ polarimetric observations. IRS 3A and 3B are distinctly detected with mass estimates of 0.21 and 1.15 $M_\odot$ respectively at $\lambda = 1.3$ mm, but IRS 3C is marginally detected with upper mass limit of 0.03 $M_\odot$ (Section 3.3). The ambient velocities of IRS 3A, 3B, and 3C are estimated as 5.5, 4.5, and 3.5 km s^{-1}, respectively, from ^{13}CO $J = 1 \rightarrow 0$ and C^{18}O $J = 1 \rightarrow 0$ channel maps (Section 3.4). The two close sources, IRS 3A and 3B, have a velocity difference less than 1 km s^{-1}; the difference is a kinematical constraint on a gravitationally bound binary system. Moreover, we estimated the specific angular momentum of the binary system as $\sim 3 \times 10^{20}$ cm^2 s^{-1}, similar to the upper limit of binary stars in Taurus and to the lower limit of molecular cloud cores (Section 3.6).

We present CO $J = 2 \rightarrow 1$ observations showing two outflows, one each from IRS 3A and 3B (Section 3.5). The outflow driven by IRS 3A has PA = 155° and is nearly perpendicular to the line of sight, while the outflow by IRS 3B has PA = 105°. In addition, we posit that the two outflows are interacting in the southern lobe of the IRS 3A outflow and the redshifted lobe of the IRS 3B outflow, based on a comparison of the kinetic energies of lobes. Coupled with the fact that the linear polarization detected in CO $J = 2 \rightarrow 1$ is likely to come from the IRS 3B outflow, IRS 3B is closer than IRS 3A. We also detected that the IRS 3B outflow has accelerating and non-accelerating features in the velocity-position diagram, which is interpreted as either a precessing outflow or a "trumpet" outflow. Assuming a "trumpet" outflow of IRS 3B rather than its precession, we estimated the velocity, inclination angle, and the opening angle, using Bayesian statistics. The velocity and the inclination angle are constrained between 100 and 40 km s^{-1} and between 75° and 50°, respectively, as the opening angle between 8° and 26°. Furthermore, using an opening angle of $\sim 20°$ from Spitzer Space Telescope observations, the velocity and the inclination angle of the IRS 3B outflow are ~ 45 km s^{-1} and $\sim 57°$.

Linear polarization in both the $\lambda = 1.3$ mm continuum and CO $J = 2 \rightarrow 1$ spectral line is marginally detected around the center and outflow of IRS 3B, respectively (Section 3.7). The dust emission polarization gives a magnetic field perpendicular to the outflow, which

may be a toroidal magnetic field parallel to the circumstellar disk. In contrast, the spectral line polarization suggests either a perpendicular or a parallel magnetic field to the IRS 3B outflow. To determine the relation between the magnetic field and the outflow direction, more sensitive polarimetric observations are required.

The L1448 IRS 3 is an excellent region to study star formation. The IRS 3A outflow, nearly perpendicular to the line of sight, enables the study of the disk and outflow structures in protostar systems more easily, since it shows the profile projected in the plane of the sky. In addition, the binary system of IRS 3A and 3B having two outflows in quite different directions gives an opportunity to study the interaction between two sources as well as constrain binary system formation itself. Finally, more sensitive polarimetric observations will provide clues on the connection between outflows and magnetic fields.

Table 3.1 Positions and simple estimates of mass from the $\lambda = 1.3$ mm continuum.

Source	α (J2000)[a]	δ (J2000)[a]	Flux (Jy)	Mass ($M_\odot$)	$\bar{n}_{H_2}$[b](cm^{-3})
L1448 IRS 3A.....	03 25 36.532	+30 45 21.35	0.196±0.019	0.21±0.02	3.7×10^7
L1448 IRS 3B.....	03 25 36.339	+30 45 14.94	1.094±0.027	1.15±0.03	4.8×10^7
L1448 IRS 3C.....	03 25 35.653	+30 45 34.20	< 0.031	< 0.03	$< 8.1\times10^7$

[a] The positions are from Looney et al. (2000).

[b] Mean number density represented by hydrogen molecules. The volumes are estimated as spheres with diameters of 5″, 8″, and 2″ for 3A, 3B, and 3C, respectively.

Table 3.2 Mass, momentum, and kinetic energy estimates of outflow lobes.

Lobes[a]	Red-North	Red-East	Black-North	Black-South[b]	Blue-West
Outflow Sources	IRS 3A	IRS 3B	IRS 3A	IRS 3A & 3B	IRS 3B
Integrated Flux (Jy km s^{-1})	47.47±1.43	101.6±1.55	168.7±1.75	347.3±2.01	304.2±4.36
Mass (10^{-3} $M_\odot$)	0.153±0.005	0.327±0.005	0.543±0.006	1.12±0.006	0.980±0.014
Mean no. density[c](10^3 cm^{-3})	6.6	6.9	7.0	5.9	9.2
Momentum[d](10^{-3} $M_\odot$ km s^{-1})	1.2	3.5	0.43, -0.64[f]	1.1, -1.1	-18
Kinetic Energy[e](10^{41} erg)	1.0	4.4	0.22	0.44	38

[a] Components in Figure 3.5 as contour colors and positions.

[b] This lobe has two components, one from the IRS 3A outflow and the other from the IRS 3B outflow.

[c] Mean number density represented by hydrogen molecules. Cylinders along outflows are assumed to estimate the volumes. The assumed diameters and lengths of the cylinders are 5.″5 & 13.″5, 6.″0 & 19.″0, 8.″0 & 17.″5, 11.″0 & 23.″0, and 10.″0 & 15.″5. Note that these are not mean number densities indicating the whole outflow lobes, but partial components of the lobes. For example, the mean number density of the northern lobe of the IRS 3A outflow would be $6.6 + 7.0 = 13.6$ (10^3 cm^{-3}), assuming the two components occupy the same region.

[d] Inclination factor, $1/\cos\theta$, is not applied.

[e] Inclination factor, $1/\cos^2\theta$, is not applied.

[f] Plus value is estimated from the redshifted channel and minus from the blueshifted channel.

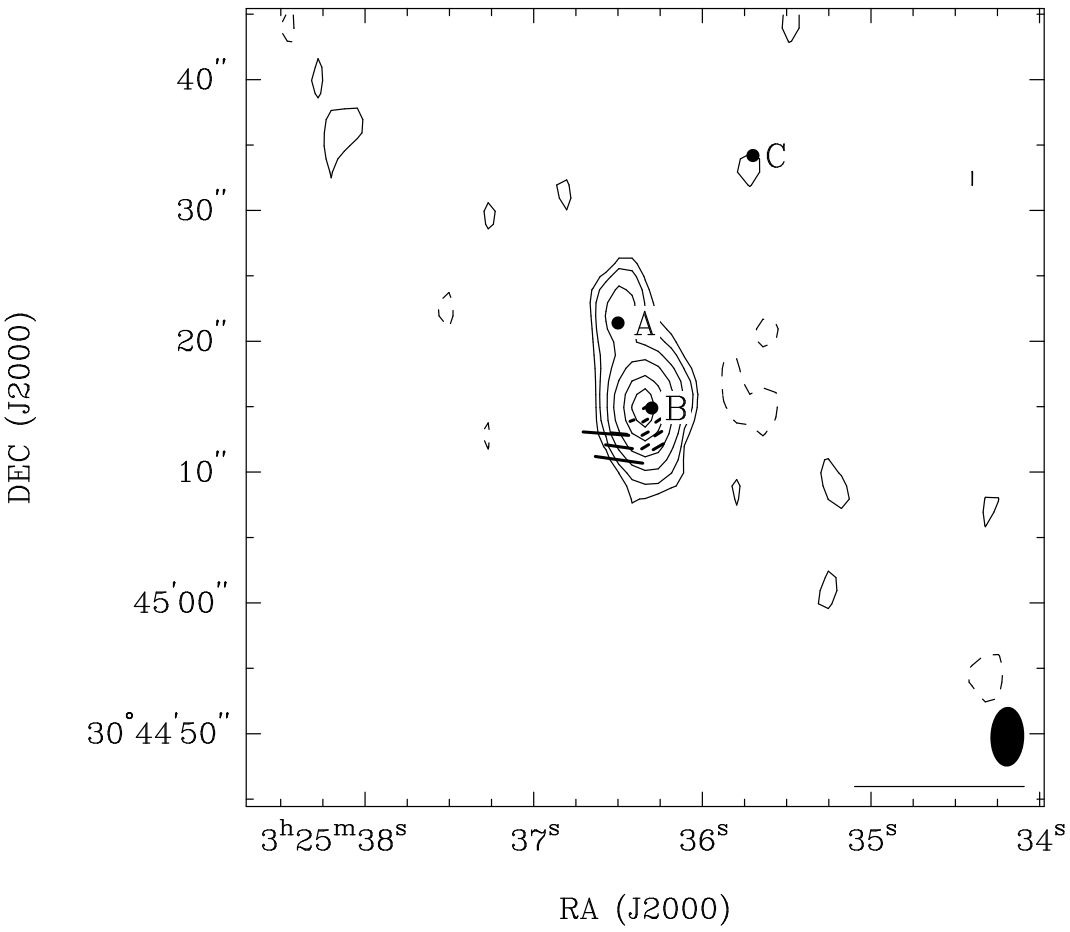

Figure 3.1 $\lambda = 1.3$ mm continuum map of L1448 IRS 3. Vectors indicate linear polarization and the symbols at bottom right show the synthesized beam of $4\farcs6 \times 2\farcs6$ (PA $= -1.6°$) and 100% polarization scale. Contour levels are 3, 5, 10, 20, 40, and 60 times $\sigma = 9.4$ mJy beam^{-1}.

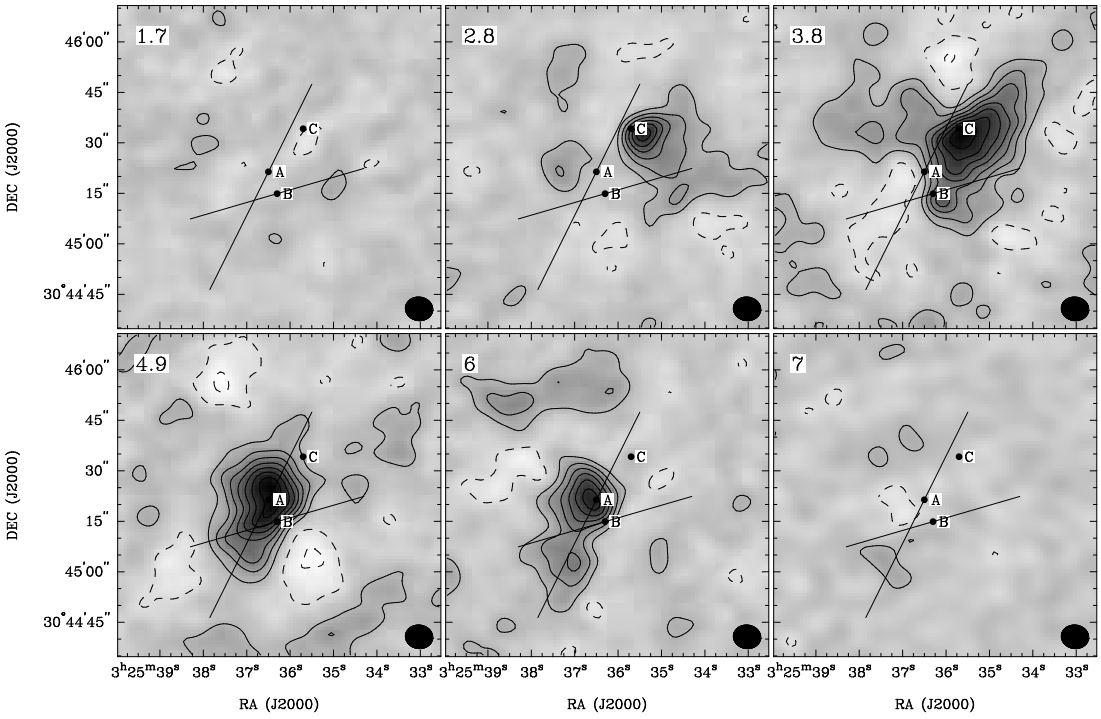

Figure 3.2 ^{13}CO $J = 1 \rightarrow 0$ channel maps of L1448 IRS 3. Two lines indicate the outflow directions that are discussed in Section 3.5. Source locations and beam size are marked. The synthesized beam is $8\farcs1 \times 7\farcs0$ and PA $= 82°$. Contour levels are 3, 7, 11, 15 19, 23, 31, and 35 times $\sigma = 76$ mJy beam^{-1}.

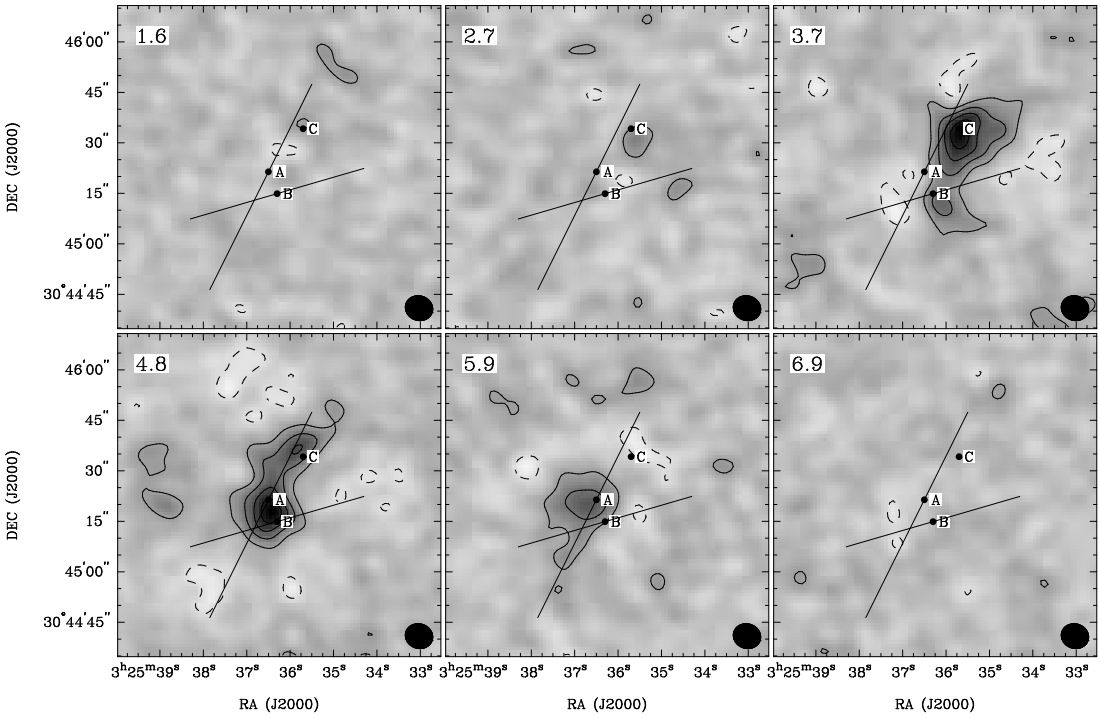

Figure 3.3 $C^{18}O$ $J = 1 \rightarrow 0$ channel maps of L1448 IRS 3. Two lines indicate the outflow directions that are discussed in Section 3.5. Source locations and beam size are marked. The synthesized beam is $8\farcs2 \times 7\farcs3$ and PA $= 72°$. Contour levels are 3, 7, 11, and 15 times $\sigma = 76$ mJy beam^{-1}.

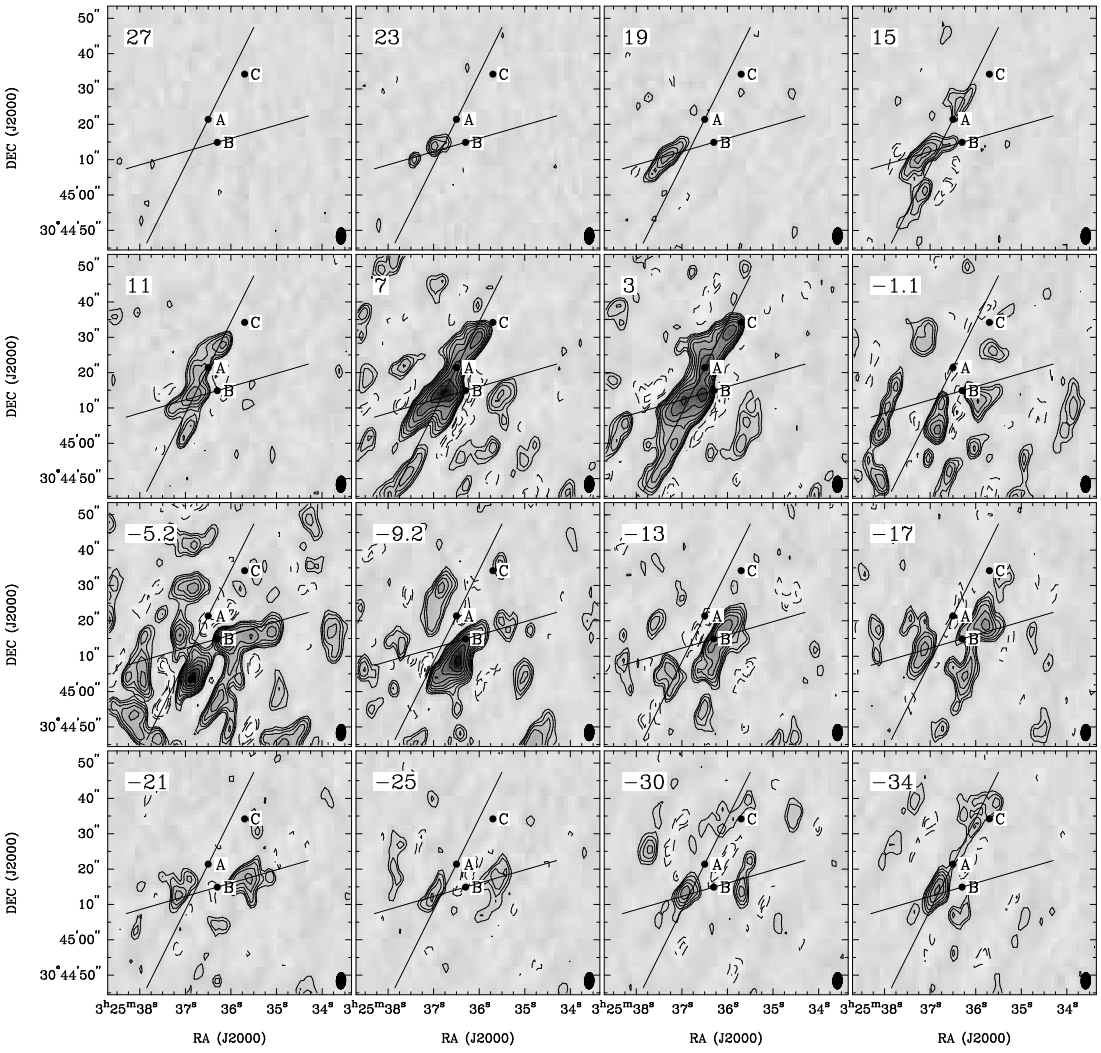

Figure 3.4 CO $J = 2 \rightarrow 1$ channel maps of L1448 IRS 3. Two lines indicate the outflow directions that are discussed in Section 3.5. Source locations and beam size are marked. The synthesized beam is $4\farcs5 \times 2\farcs5$ and PA $= -2.4°$. Contour levels are 2.8, 4, 5.7, 8, 11.3, 16, 22.6, 32, and 45.3 times $\sigma = 0.144$ Jy beam^{-1}.

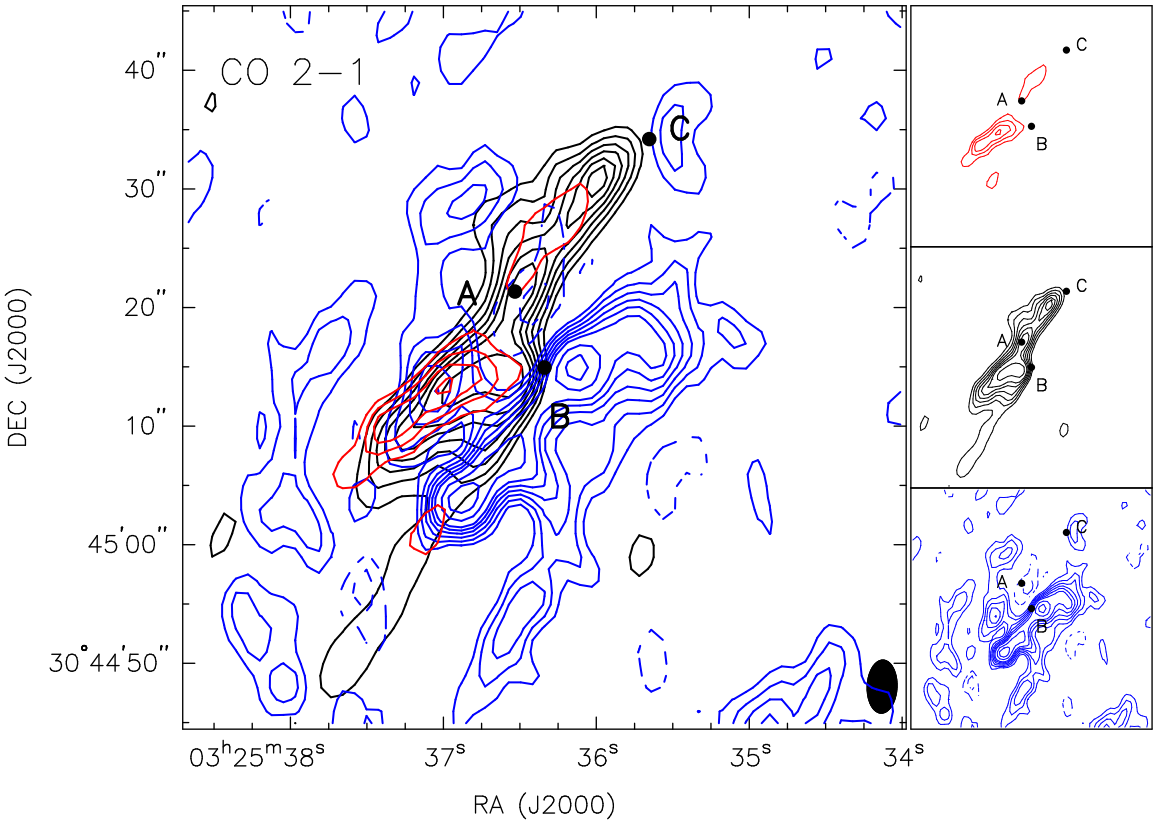

Figure 3.5 Integrated intensity map of L1448 IRS 3. Red, black, and blue contours present velocity ranges from +25 to +9 km s^{-1} (4 channels), from +9 to +1 km s^{-1} (2 channels), and from +1 to −32 km s^{-1} (8 channels), respectively. The three sub-images on the right have the same velocity ranges as the main panel with the same contour levels, size-scale, etc., but they are separated for easier comparison. The synthesized beam is $4\farcs5 \times 2\farcs5$ and PA = −2.4°. Black contours mainly show the IRS 3A outflow and red and blue contours mainly represent redshifted and blueshifted lobes of the IRS 3B outflow. Blue contours look complicated due to blueshifted components of the mm source outflow. Contour levels are 3, 5, 7, 9, 11, 13, 17, 21, 25, 29, 35, 41, and 49 times 2.3 Jy beam^{-1} km s^{-1}.

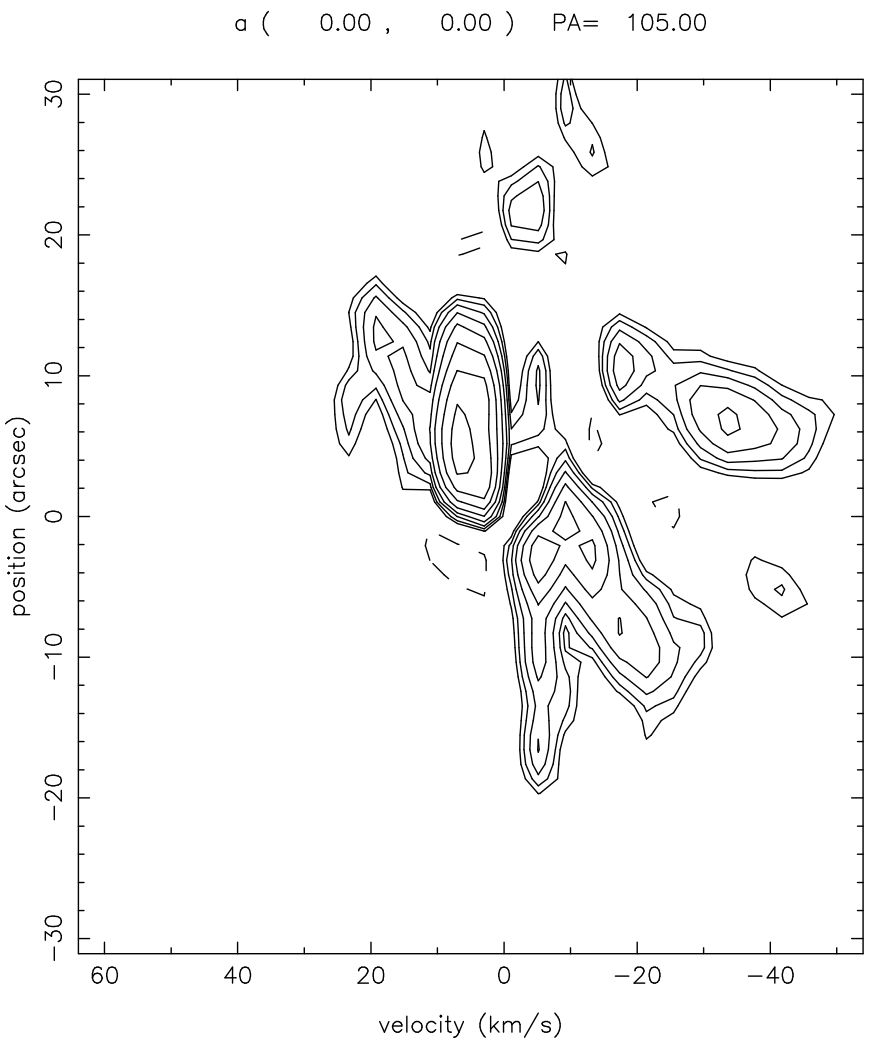

Figure 3.6 Velocity-position diagram of the L1448 IRS 3B outflow. The cut is along 105° from IRS 3B. Contour levels are 2.8, 4, 5.7, 8, 11.3, 16, 22.6, 32, and 45.3 times σ = 0.144 Jy beam^{-1} same as Figure 3.4.

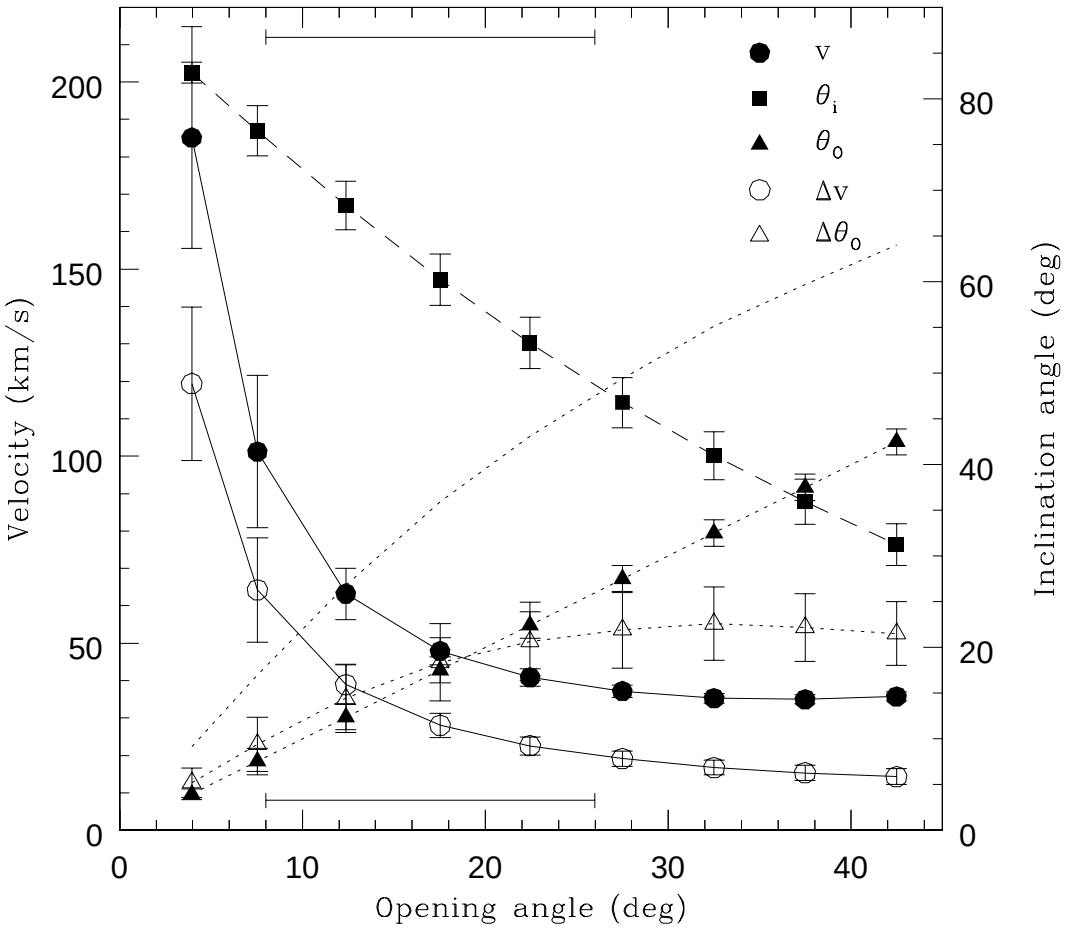

Figure 3.7 Results of searching IRS 3B outflow parameters, velocity (solid circles), inclination angle (solid squares), and velocity and opening angle differences (open circles and open triangles, respectively) versus opening angle. The opening angle is also plotted (solid triangles) to compare with the other parameters. The data points are average values of parameters of samples in 5° bins of the opening angle and the error bars present the standard deviations of the bins. The dotted line without data points indicates the opening angle plus the opening angle difference. The range of the derived opening angles that are consistent with the observations ($8° < \theta_o < 26°$) is indicated by the horizontal bars at the top and bottom of the plot.

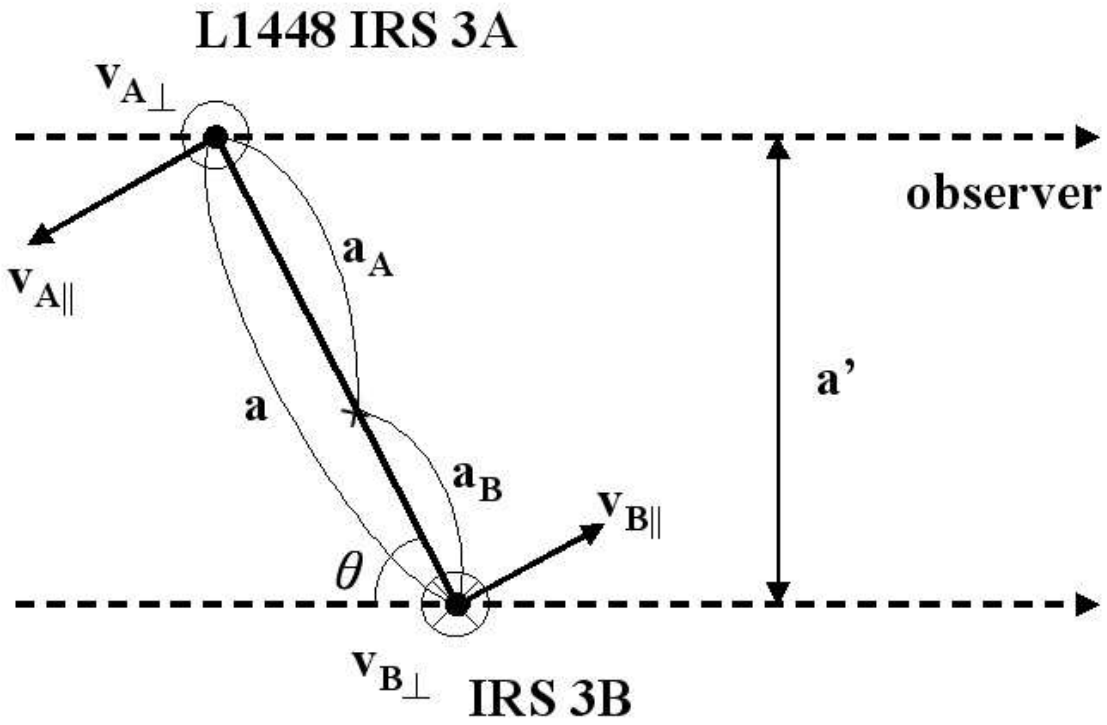

Figure 3.8 Schematic diagram illustrating the binary system of L1448 IRS 3A and 3B. The velocity components vertical to the line-of-sight plane are assumed as forward $v_{A\perp}$ and backward $v_{B\perp}$. They may be opposite directions such as backward $v_{A\perp}$ and forward $v_{B\perp}$.

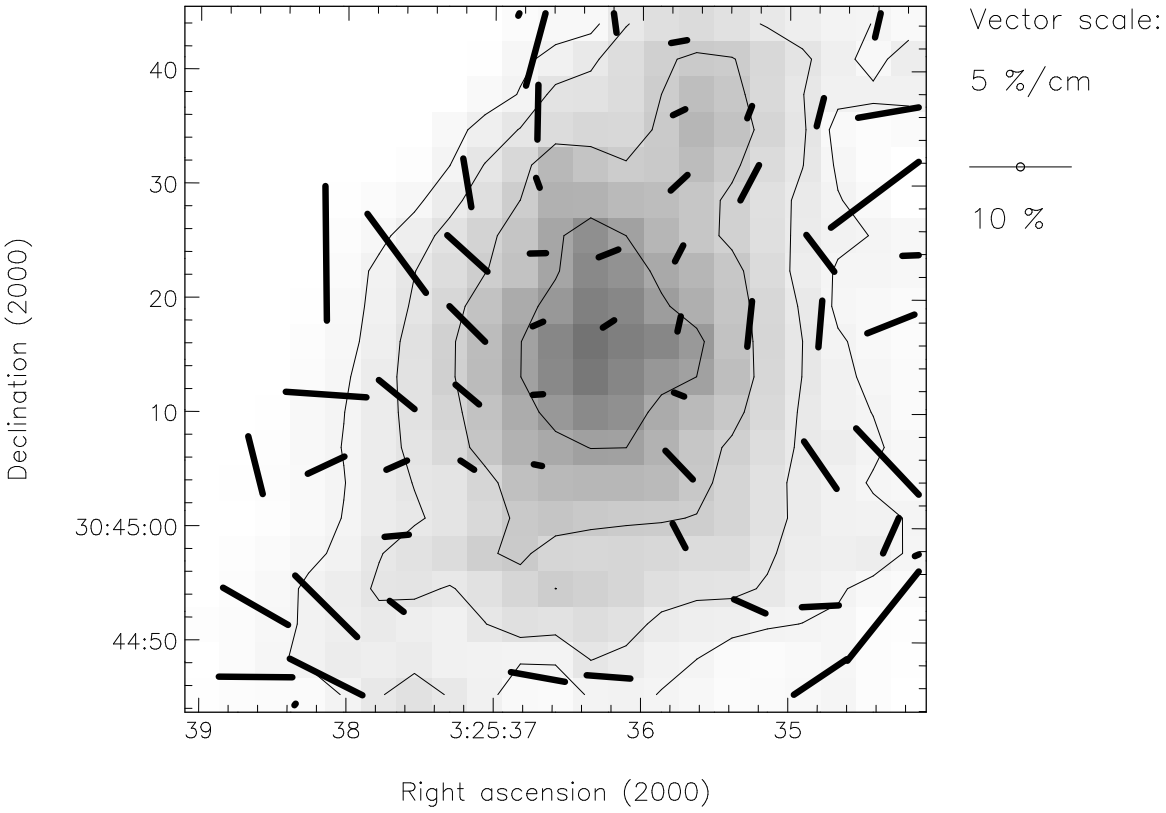

Figure 3.9 Large scale magnetic field in L1448 IRS 3 observed by SCUBA at $\lambda = 850$ μm. Note that vectors indicate linear polarization and the direction around IRS 3B is consistent with our $\lambda = 1.3$ mm continuum data. The beam size is $\sim 13''$. Gray scales and contour levels are 0.9, 0.8, 0.6, and 0.4 of the peak intensity, 6.5 Jy beam^{-1} derived from the data presented in Hatchell et al. (2005).

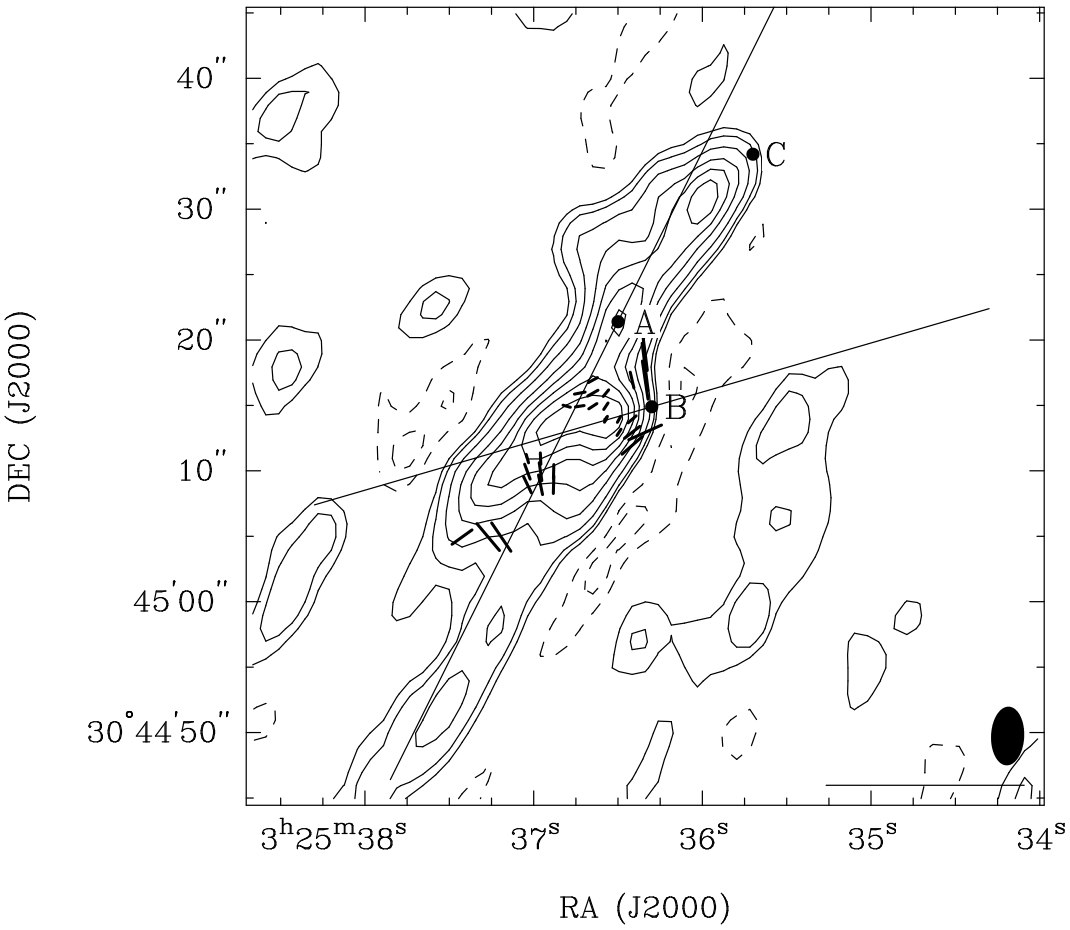

Figure 3.10 CO $J = 2 \rightarrow 1$ map of L1448 IRS 3, combined in two channels, a velocity range from +1 to +9 km s^{-1}. Vectors indicate linear polarization and the symbols at right bottom show the synthesized beam ($4\farcs5 \times 2\farcs5$ and PA $= -2.4°$) and 100% polarization scale. Two lines present outflow directions from IRS 3A and 3B. Contour levels are 3, 5, 9, 15, 21, 27, 33, 39, and 45 times $\sigma = 0.126$ Jy beam^{-1}.

4 Circumstellar Disks

4.1 Introduction

Circumstellar disks are often called T Tauri disks or protoplanetary disks. These disks, in particular circumstellar disks around young solar analogies, have been attracting astronomers' attention for the last few decades, as they are the natal environment of planetary systems. The most familiar circumstellar disk source would be the nearest one, the early solar system disk or the so-called solar nebula. Weidenschilling (1977) estimated the minimal-mass of the solar nebula as 0.01–0.1 $M_\odot$ and found that the surface density was proportional to $r^{-3/2}$, based on the current composition and mass of planets and asteroids. In addition, Hayashi (1981) studied the solar nebula structure including magnetic field effects and reported that the magnetic field effects are negligible except in the outer disk region.

On the other hand, circumstellar disks possibly developing extrasolar planetary systems have mainly been studied by their spectral energy distribution (SED) over the past 20 years (e.g., Beckwith et al., 1990; Andrews & Williams, 2005). For example, Beckwith et al. (1990) observed 86 YSOs in the Taurus-Auriga dark cloud at $\lambda = 1.3$ mm and detected dust continuum emission toward 42% of the targets. Based on the strength of the continuum emission and the low extinction of the central protostars, they showed that the small particles are distributed in geometrically flat structures (i.e., disks), not spherically distributed. They also estimated disk properties using dust temperatures obtained from SEDs and assuming disk structures like density and temperature distributions in a power law. A few years ago, Andrews & Williams (2005) presented multi sub/millimeter observations of a larger sample YSOs. They also estimated disk properties using SEDs.

Although using SEDs is a good method to study a large number of sources, it is difficult to investigate the disk structure in detail, due to lack of information; it requires one to assume disk structures. Meanwhile, there have been circumstellar disk studies using radio interferometric observations in dust continuum with high angular resolution (e.g. Mundy et al., 1996; Wilner et al., 1996; Lay et al., 1997). Indeed, radio interferometers at sub/millimeter are the best means to study circumstellar disks. They can provide angular resolutions high enough to resolve circumstellar disks, which are typically less than $1''$ in size, and they are sensitive to the dust black-body emission. Note that longer wavelength

observations can be contaminated with emission by other mechanisms such as free-free emission and synchrotron emission. The free-free emission fraction decreases along shorter wavelengths and down to about a few percent at $\lambda = 3$ mm.

In addition to dust continuum, gas spectral line observations have been carried out toward circumstellar disks as well, using radio interferometers (e.g. Dutrey et al., 1994; Guilloteau & Dutrey, 1994; Dutrey et al., 1996, 1998; Guilloteau & Dutrey, 1998; Simon et al., 2000; Dartois et al., 2003; Qi et al., 2003, 2004; Piétu et al., 2005; Dutrey et al., 2006; Qi et al., 2006; Dutrey et al., 2007). As circumstellar disks are detected as more extended in spectral lines (mainly CO), they are resolved out easily by interferometers in expanded configurations. This aspect makes it difficult to obtain good spectral line data for disk studies. However, spectral line data provide much information. For example, they enable studies of disk kinematics (if they are in Keplerian rotation or not) and they can be used for examining vertical disk temperature distribution (e.g., Dartois et al., 2003). Furthermore, multiple species observations of molecules and ions allow us to study chemistry in circumstellar disks (e.g., Dutrey et al., 2006; Bergin, 2009) and it is a potential means for investigating a disk's ionization fraction with X-ray observations (e.g., Qi et al., 2006), which is a key property to examine the accretion mechanism of circumstellar disks.

These radio interferometric observations in dust continuum and gas spectral lines have been limited in a number of targets. In other words, lack of sensitivity and angular resolution has led to bright targets so far: bright and/or close T Tauri stars or more massive counterpart systems (Herbig Ae/Be stars). CARMA has been changing this situation with its unprecedented image fidelity from the largest number of baselines and its high angular resolution. Therefore, we have initiated a CARMA T Tauri disk survey two years ago. So far we have obtained a "complete" data set of 6 targets over A, B, C, and/or D configurations at $\lambda = 1.3$ mm and 2.7 mm and here we present the results.

Some previous studies have fit SEDs with interferometric data together (e.g., Kitamura et al., 2002; Andrews et al., 2009). However, we did not attempt to fit SED data simultaneously when finding the best model, since the SED data have been obtained mostly with low angular resolution ($\sim 10''$) and they depend on an assumption of dust opacity with frequency. In addition, note that we have two wavelength data at sub-arcsecond resolution each, which are the best data set ever to constrain disk properties.

Circumstellar disk models have been assumed with a power-law density distribution in many observational studies using SED and interferometry data (e.g., Beckwith et al., 1990; Mundy et al., 1996; Andrews & Williams, 2007; Dutrey et al., 2007). It is a quite reasonable and successful assumption. The minimal-mass solar nebula shows a power-law density distribution (Weidenschilling, 1977) and Mundy et al. (1996) found early that interferometric data of HL Tau with sub-arcsecond angular resolution follow a power-law density distribution very well. In addition, numerical simulations of circumstellar disks show that

the density distribution of circumstellar disks is a power law (e.g., Ayliffe & Bate, 2009). However, there is no fundamental physics behind such a power-law disk model. In addition, it can not explain the differences between disk sizes detected in dust continuum (compact and massive) and CO (extended and less massive). For having a better physical understanding, the viscous accretion disk model (e.g., Pringle, 1981; Hartmann et al., 1998) with a form of a power-law density distribution tapered by an exponential function started being used to fit observational data recently, instead of truncated power-law models (Kitamura et al., 2002; Hughes et al., 2008; Isella et al., 2009; Andrews et al., 2009). Some previous studies also argue that the viscous accretion disk model explains both dust continuum and gas spectral line data better than the power-law disk model (Hughes et al., 2008). However, comparison of the truncated power-law disk model with the viscous accretion disk model without an outer radius may not be able to distinguish the boundary effects; it can be just due to the extremely different boundaries. In this study, therefore, we compare a power-law disk model of a Gaussian edge with the viscous accretion disk model to fit our data, in order to find whether the viscous accretion disk model is preferred for fitting the observational data.

As introduced in Chapter 1, Bayesian inference is used to find parameter distributions to fit observational data, instead of the commonly used least χ^2 method. The Bayesian approach provides a basis of probability theory to compare two models as well as to achieve parameter probability distributions, which are not given by the χ^2 method. Although the χ^2 method has been used widely, a couple of circumstellar disk studies have been carried out utilizing Bayesian inference (Lay et al., 1997; Isella et al., 2009). Note that, however, no model comparison has been attempted for circumstellar disks so far in the Bayesian approach.

In this chapter, we present observational results of our CARMA T Tauri disk survey. The data have the best angular resolutions ever at $\lambda = 1.3$ mm and 2.7 mm and they have been obtained at two wavelengths with the high image fidelity of CARMA. In addition, we will compare a flared power-law disk model of a Gaussian edge with a viscous accretion disk model in Bayesian inference. First, brief introductions of the targets are given in Section 4.2 and CARMA observations and data reduction are discussed in the following section. After that, the two disk models of flared power-law disks with a Gaussian edge and viscous accretion disks are explained. The observational and fitting results are following code test results in Section 4.5 and 4.6. At the end discussion and summary of the results are found.

4.2 Targets in the Taurus Molecular Cloud

Circumstellar disk targets of this study are located in the Taurus molecular cloud. The Taurus molecular cloud is a well-known, nearby star forming region. The distance has been

determined by various methods (Rebull et al., 2004): e.g., star counting (e.g., McCuskey, 1938), optical extinction (e.g., Kenyon et al., 1994, 140 ± 10 pc), parallax measurement (e.g., Hipparcos astrometric data: Bertout et al., 1999), and protostellar rotational properties (Preibisch & Smith, 1997, 152 ± 10 pc). The measured distances to the Taurus molecular cloud are somewhat different in methods and in regions. For example, Bertout et al. (1999) reported three regions of 125^{+21}_{-16} pc, 140^{+16}_{-13} pc, and 168^{+42}_{-28} pc, using Hipparcos astrometric data. However, 140 pc is within uncertainties of most of the ranges, so it is accepted for all 6 targets in this study. Note that the distance difference affects the physical sizes and mass estimates.

These 6 targets have been chosen in the sample of Beckwith et al. (1990), which observed 86 YSOs in the Taurus molecular cloud at $\lambda = 1.3$ mm using the IRAM 30 m telescope. Andrews & Williams (2005) carried out submillimeter observations at $\lambda = 450$ and 850 μm toward YSOs of the Taurus molecular cloud using SCUBA on the JCMT. On the other hand, Kenyon & Hartmann (1995) compiled published IR and optical observations with supplementary IR observations in the cloud. Recently, Furlan et al. (2009) also reported $\lambda \approx 10$ μm feature strengths (equivalent width of the 10 μm feature, EW(10 μm)) and spectral index (n_{13-31}) between $\lambda = 13$ and 31 μm of T Tauri disks in the Taurus molecular cloud including our targets except HL Tau, as well as two other star forming regions using SST IRS data. They utilized these values to indicate dust evolution; for example, smaller n_{13-31} values present disks with more dust settlement (less flaring) and EW(10 μm) shows the amount of small dust grains (< 5 μm), which means that smaller EW(10 μm) indicates more evolved dust. Selected information from the above studies is summarized in Table 4.1. More detailed studies have been carried out toward these targets and some selected examples are introduced in the following.

CI Tau was observed by Beckwith et al. (1990) with a continuum flux of 190 ± 17 mJy at $\lambda = 1.3$ mm. In addition, variability in optical spectra has been detected, which can be interpreted as a temporary obscuration of a local hot region (Smith et al., 1999). Andrews & Williams (2007) observed CI Tau using SMA at $\lambda = 880$ μm with a moderate angular resolution ($> 1''$). By model fitting of SED data and visibility data averaged in annulus, they constrained physical properties such as density and temperature distributions, size, and mass.

DL Tau has been detected with a continuum flux of 230 ± 14 mJy by IRAM observations (Beckwith et al., 1990). It has also been detected in the CO $J = 2 \rightarrow 1$ line, and the velocity field was shown (e.g., Koerner & Sargent, 1995). Simon et al. (2000) studied the kinematics using PdBI data in CO $J = 2 \rightarrow 1$. They showed that the disk is in Keplerian rotation and estimated the protostellar mass as 0.72 ± 0.11 $M_\odot$ assuming the inclination determined by the continuum image ($49 \pm 3°$). Kitamura et al. (2002) has studied the disk structure by fitting SEDs and Noveyama Millimeter Array data taken at $\lambda = 2$ mm with $1''$ resolution.

They employed a viscous accretion disk as well as a power-law disk model. Andrews & Williams (2007) also studied the DL Tau disk structure using SMA data at $\lambda = 1.3$ mm with about $2''$ resolution.

DO Tau has a continuum flux of 136±11 mJy in the Beckwith et al. (1990) observations. Koerner & Sargent (1995) have reported CO $J = 2 \rightarrow 1$ observational results . The line profile has a much broader feature in the blueshifted region than in the redshifted region, which indicates that it needs infall and bipolar outflow components. DO Tau is also one of the sample in the studies of Kitamura et al. (2002).

FT Tau has a continuum flux measured in Beckwith et al. (1990) of 130 ± 14 mJy at $\lambda = 1.3$ mm. In previous survey observations at optical wavelengths, however, the spectral type of FT Tau was not determined probably due to an undetermined luminosity, although the surveys included the target. Therefore, there is no good estimate of protostellar mass and age, which are normally determined by its effective temperature and luminosity. Robitaille et al. (2007) reported wide ranges of stellar parameters by SED fitting: for example, protostellar temperature between 3060 and 5013 K and mass between 0.11 and 2.03 $M_\odot$. Andrews & Williams (2007) observed FT Tau with an angular resolution of $1.7'' \times 1.1''$ at $\lambda = 880$ μm using SMA. Although they did not resolve the disk structure, they constrained disk properties by model fitting with the data and SEDs.

Haro 6-13 has been detected with a continuum flux of 124 ± 13 mJy by Beckwith et al. (1990). Recently, Schaefer et al. (2009) observed the target in CO $J = 2 \rightarrow 1$ and $J = 1 \rightarrow 0$ as well as $\lambda = 1.3$ mm and 2.7 mm continuum using PdBI. They estimated the protostellar mass as 1.0 ± 0.15 $M_\odot$, based on the rotational velocity field. They discussed that the difference from the mass estimated by the evolutionary track on the HR diagram (~ 0.6 $M_\odot$) may be due to limited number of channel maps for the CO data model fitting.

HL Tau is one of the T Tauri stars (Class II) that has been studied very broadly over the last two decades (e.g., CO cloud associated to HL Tau: Beckwith et al., 1986). The disk has been studied by observations in sub/millimeter wavelength continuum using various single dishes and interferometers: for example, IRAM at $\lambda = 1.3$ mm (Beckwith et al., 1990), BIMA at $\lambda = 2.7$ mm (Mundy et al., 1996; Looney et al., 2000), VLA at centimeter and millimeter wavelengths (Wilner et al., 1996), interferometers including OVRO and CSO-JCMT at sub/millimeter wavelengths (Lay et al., 1997), and JCMT at submillimeter wavelengths (Chandler & Richer, 2000). In particular, Mundy et al. (1996) found physical properties such as density and temperature distribution, disk mass, outer radius, and inclination angle, through power-law disk model fitting to sub-arcsecond ($1\farcs32 \times 0\farcs48$) angular resolution BIMA data at $\lambda = 2.7$ mm. Kitamura et al. (2002) also studied HL Tau by modeling of a viscous accretion disk as well as a power-law disk. In addition to the disk structure, an optical jet was also studied (e.g., Mundt et al., 1990). Robitaille et al. (2007) has reported that HL Tau has an envelope component through SED modeling over optical,

IR, and submillimeter wavelengths.

Recently, Greaves et al. (2008) has claimed a protoplanet candidate around 65 AU using the VLA at 1.3 cm with 0.08″ angular resolution. Nero & Bjorkman (2009) discussed the possibility of planet formation through disk fragmentation where Greaves et al. (2008) found a compact feature in HL Tau. Based on the Toomre Q parameter and cooling time, they argue that the compact feature can be explained by a planet formed by disk fragmentation. In contrast, Carrasco-González et al. (2009) did not detect a continuum object corresponding to the protoplanet candidate, at $\lambda = 7$ mm with $\sim 0.05''$ angular resolution.

4.3 Observations and Data

We have carried out a survey of protoplanetary disks using CARMA. As introduced in Chapter 1, CARMA is a heterogeneous array consisting of six 10.1 m, nine 6.4 m, and eight 3.5 m antennas. For this project, the 3.5 m antennas were unavailable and the benefits are apparently minimal, as high angular resolution and high sensitivity are required. It was attempted to obtain 11 protoplanetary disk data but due to weather and other instrumental issues we ended up with "complete" data sets of 6 targets: CI Tau, DL Tau, DO Tau, FT Tau, Haro 6-13, and HL Tau in alphabetical order. The details of data acquisition are summarized in Table 4.2. As shown in the table, it took about two years to achieve all the data and the observation time is roughly 160 hours in total, counting only the useful data sets. Five targets among the six have been observed in A and/or B configurations, which provide high angular resolution better than 0.3″ at $\lambda = 1.3$ mm. Table 4.3 has information of the final combined data with their synthesized beam sizes and the noise level.

We have observed the protoplanetary disks in A, B, C, and D configurations, in order to detect large scale structures as well as small scales. The highest angular resolution (the smallest synthesized beam size) is $\sim$0.13″ at $\lambda = 1.3$ mm toward HL Tau. The angular resolutions for the other targets are a bit less ($\sim$0.3″). The *uv* coverage of our data are summarized in Table 4.3. As shown in the table, the minimum *uv* distance is about a few kilo-wavelengths, which means our data sets are sensitive up to a few tens of arc second scales. As the target disks are less than 1 arc second in size, there is no resolving-out flux issue in the study, from which interferometric observations typically suffer.

The largely extended arrays (A and B configurations) require more stable atmospheric conditions due to long baselines. It is actually challenging to obtain such good weather conditions even at the CARMA site. To verify our data quality, therefore, we have observed an additional calibrator (a test calibrator) with a gain calibrator. Since a test calibrator is chosen to be a point source nearby our targets, data quality after applying gain solutions can be examined by the test calibrator's shape and flux. All of our A and B configuration

data and some of the compact array data have such a test calibrator. Most of our data have built a point or point-like image of a test calibrator, which means successful calibration. Here the "point-like" means that the deconvoluted size of a test calibrator is less than half of a synthesized beam in both major and minor axes. A few of the worst data sets have a test calibrator size comparable to the synthesized beam and those sets are indicated in Table 4.2. In addition, we examined the flatness of the *uv* amplitude slopes of the gain calibrators. Since *uv* data are the Fourier transform of an image, a gain calibrator of a point source should have a flat amplitude versus *uv* distance. If it is not achieved, i.e., amplitudes at long *uv* distance regions (small scales, central regions) drop, the target data are likely to be biased, resulting in an apparent shallower gradient of density and/or temperature. All of our data sets have a flat amplitude slope of gain calibrators after calibration, except a data set taken in B configuration at $\lambda = 1.3$ mm toward DO Tau, which has about 25% variation in the middle. However, the DO Tau data are also used with caution, since it does not appear to affect the results significantly.

CARMA itself has a special technique for calibration of atmospheric perturbation, called Paired Antenna Calibration System (PACS) (Lamb et al., 2009). In large antenna spacings such as A and B configurations, the 3.5 m antennas are paired with boundary 10.4 m or 6.1 m antennas, which are elements of long baselines. The 3.5 m antennas are always observing a calibrator at 30 GHz, while the other antennas are observing science targets and calibrators. During the calibration of data, the phase of the 3.5 m antenna gain solution is used to correct the phase delay (phase difference) caused by short atmospheric perturbations ($\sim$4–20 seconds) on the paired antennas. Since visibility phase depends on time delay and wavelengths/frequencies, the phase of the gain solution is scaled by the ratio of observation frequencies to 30 GHz. The A configuration data of HL Tau at $\lambda = 1.3$ mm and the A configuration data of FT Tau at $\lambda = 2.7$ mm are calibrated using PACS. The calibrators used for PACS are separated from HL Tau and FT Tau by 9° and 13°, respectively, and the improvement of calibrated data is about 10–20% in terms of image noise levels and the size, flux, and peak intensity of test calibrators.

Similar to the study of envelope properties described in Chapter 2, we have obtained two wavelength data ($\lambda = 1.3$ mm and 2.7 mm) in order to better constrain the dust properties. The absolute flux calibration is again noteworthy here. As emphasized in Chapter 2, properties constrained by multi-frequency data mainly depend on absolute flux calibration. To minimize the bias induced by flux calibration uncertainty, a good flux calibrator (e.g., Uranus) was used (Table 4.2). In addition, gain calibrator fluxes of all tracks have been compared with each other in the time basis. Rapid variation of gain calibrator fluxes (e.g., 50% increase or decrease within a few days) is unrealistic, although quasar gain calibrators are intrinsically variable. For comparison, the CARMA flux catalog and the SMA calibrator list have been taken into account, as well as the gain calibrator values bootstrapped from

flux calibrators. One more thing to be pointed out is that different array-configuration data of the same targets have been compared at common *uv* distances. Sub/millimeter dust emission from T Tauri disks is not variable over a period of a few years, so amplitudes at common *uv* positions should be comparable even in different configuration arrays. It is so at common *uv* distances, when objects are spherical or *uv* coverage around the *uv* distances is similar. Actually, this comparison is a crucial step when combining various array-configuration data. As a result, we presume absolute flux calibration uncertainty of our T Tauri disk data is less than the uncertainty assumed in the envelope studies of Chapter 2 (15% at $\lambda = 1.3$ mm and 10% at $\lambda = 2.7$ mm), which use only one or two tracks in an array-configuration for each frequency data.

MIRIAD has been employed to calibrate and map data. Individual tracks have been calibrated separately and combined in the invert-Fourier transform step to make maps. The sensitivity and emphasized scales of maps depend on weighting schemes of visibility data. Natural weighting gives the highest S/N and the worst angular resolution, since visibility data points are sparse at large *uv* distances and visibilities at larger *uv* distances are noisier due to atmospheric turbulence. On the other hand, uniform weighting emphasizes small scales best although the S/N is worst. For intermediate weighting, Briggs introduced a robust parameter (Briggs, 1995): 2 of the parameter for weighting close to the natural weighting and -2 close to the uniform weighting. In order to have small structures reasonably emphasized, the weighting scheme with a robust value of 0 has been applied.

4.4 Disk Model Fitting

4.4.1 Disk Model I: Power Law Disk with a Gaussian Boundary

We adopt a power-law disk model with a flaring in hydrostatic equilibrium. We assume the disk is axisymmetric and the expression of the density in cylindrical coordinates (R, ϕ, z) is:

$$\begin{aligned} \rho(R,z) &= \rho(R,0)\ \exp[-(z/H(R))^2] \\ &= \rho_0 \Big(\frac{R}{R_0}\Big)^{-p} \exp[-(z/H(R))^2]. \end{aligned} \tag{4.1}$$

The z dependence and the scale hight $H(R)$ is determined by the hydrostatic equilibrium between the gravity of the central protostar and the pressure of the temperature at radius R. We ignore self gravity of the disk mass and assume that dust temperature and gas kinetic temperature are the same. In addition, we assume a constant temperature in the z direction and a "thin" disk ($R \gg z$) for the purpose of calculating the scale heights. Note that temperature depends on r in our modeling. Throughout this chapter, r indicates the distance from the central protostar and R is used for the radial distance in cylindrical

coordinates: i.e., $r^2 = R^2 + z^2$. Therefore, the scale height is obtained in the following way:

$$\begin{aligned}
\frac{\partial P}{\partial z} &= -\rho g_{\perp} \\
\frac{\partial(\rho(R,z))}{\rho(R,z)} &= -\frac{GM_*\bar{m}}{kT(R,0)}\frac{z}{r^{3/2}}\partial z \\
&\approx -\frac{GM_*\bar{m}}{kT(R,0)}\frac{z}{R^{3/2}}\partial z \\
\rho(R,z) &= \rho(R,0)\ \exp[-(z/H(R))^2], \qquad (4.2)\\
\text{where} \quad H(R) &= \sqrt{\frac{2kR^3T(R,0)}{GM_*\bar{m}}}.
\end{aligned}$$

Here G is the gravitational constant, k is the Boltzmann's constant, M_* is the central protostellar mass, and $\bar{m}$ is mean mass of molecules, i.e., mean molecular weight times hydrogen mass ($\bar{m} = \mu m_H = 2.4 m_H$). The mean molecular weight is obtained assuming $X = 0.7$, $Y = 0.28$, and $Z = 0.02$: $1/\mu = 0.5X/1 + Y/4 + 0.5Z/15.5$. As a fiducial disk mass is about a few tenths of the central protostar, we can ignore the self gravity of the disk. Previous studies (e.g., Dartois et al., 2003) have suggested a temperature gradient in the vertical direction of disks: colder in the midplane. In addition, if dust grain settling onto the midplane is significantly progressed, the temperature gradient would be much larger. However, note that the constant temperature assumption is not bad for scale heights, since the flaring part of disks are likely to be determined by the radiative equilibrium with the central protostar, regardless of the midplane conditions, and disks are "thin".

As same as the envelope studies in Chapter 2, the temperature distribution is obtained from radiative equilibrium with the central protostar. Here is the expression of temperature again for convenience. Note that it is the same as Equation 2.6 with a different distance expression:

$$\begin{aligned}
T(R,z) &= T_0 \left(\frac{R_0}{r}\right)^{2/(4+\beta)} \left(\frac{L_*}{L_0}\right)^{1/(4+\beta)} \\
&= T_0 \left(\frac{R_0}{r}\right)^{q} \left(\frac{L_*}{L_0}\right)^{q/2}, \qquad (4.3)
\end{aligned}$$

where $q \equiv 2/(4+\beta)$. We set the calibration factors (T_0, R_0, and L_0) to $T_0(R_0 = 1\ \mathrm{AU}) = 300$ K in the case of $L_0 = 1 L_\odot$. Furthermore, as the luminosity dependence is weak, we ignored the L_* factor. As our targets have 0.77–2.10 $L_\odot$ of L_* and the exponent is about 0.25 at most, the effect of the ignorance on temperature is less than 20%. Using this

temperature distribution, the scale height $H(R)$ can now be expressed as:

$$\begin{aligned} H(R) &= \sqrt{\frac{2kR_0^3T_0}{GM_*\bar{m}}}\Big(\frac{R}{R_0}\Big)^{3/2-q/2} \\ &= H_0\Big(\frac{R}{R_0}\Big)^{3/2-q/2}. \end{aligned} \tag{4.4}$$

Note that from the density and the scale height expressions, the surface density of this model is also a power law with $s = p - 3/2 + q/2 = p - 3/2 + 1/(4+\beta)$:

$$\begin{aligned} \Sigma(R) &= \int_{-\infty}^{\infty} \rho(R,z)dz \\ &= \sqrt{\pi}\rho(R,0)H(R) \\ &\propto R^{-s} \propto R^{-p+3/2-1/(4+\beta)}. \end{aligned} \tag{4.5}$$

The outer boundary of our disk model has the density decreasing as a Gaussian function with the same scale height as the vertical direction of the disk's outer radius. This model is comparable to the case of viscous accretion disk models with a constant surface density distribution in terms of the boundary form (e.g., Pringle, 1981). Although it is somewhat arbitrary, this edge condition provides the same decay of density in all outward directions at the disk outer radius. On the other hand, the inner edges are assumed sharp. Some modeling studies of circumstellar disks have presumed sublimation radii of dust grains (e.g., Andrews et al., 2009), but it is possible that inner radii are determined by other effects such as an unresolved binary companion, formed planets, etc. Therefore, we leave the inner radii as a free parameter. The Gaussian outer boundary gives an expression of ρ_0 as a function of M_{disk}:

$$\begin{aligned} M_{disk} &= \int_{R_{in}}^{R_{out}} \int_{-\infty}^{\infty} \rho(R,z)\ 2\pi R\ dz\ dR \\ &\quad + \int_{R_{out}}^{\infty} \int_{-\infty}^{\infty} \rho(R_{out},0)\exp\Big[-\frac{(R-R_{out})^2+z^2}{H(R_{out})^2}\Big]\ 2\pi R\ dR\ dz \\ &= \frac{2\pi^{3/2}}{7/2-p-q}\big[\rho(R_{out},0)H(R_{out})R_{out}^2 - \rho(R_{in},0)H(R_{in})R_{in}^2\big] \\ &\quad + \pi^{3/2}\rho(R_{out},0)H(R_{out})^2\big[\pi^{1/2}R_{out} + H(R_{out})\big] \\ \rho_0 &= M_{disk}\Big[\frac{2\pi^{3/2}}{7/2-p-q}\big[\big(R_{out}/R_0\big)^{-p}H(R_{out})R_{out}^2 - \big(R_{in}/R_0\big)^{-p}H(R_{in})R_{in}^2\big] \\ &\quad + \pi^{3/2}\big(R_{out}/R_0\big)^{-p}H(R_{out})^2\big[\pi^{1/2}R_{out} + H(R_{out})\big]\Big]^{-1}. \end{aligned} \tag{4.6}$$

The dust opacity spectral index β is one of the most interesting parameters in this study.

Indeed, in order to constrain β better, we fit two wavelength data simultaneously using

$$\kappa_\nu = \kappa_0(\nu/\nu_0)^\beta. \tag{4.7}$$

β is determined between two wavelengths ($\lambda = 1.3$ mm and 2.7 mm) and $\kappa_0 = 0.01$ cm^2 g^{-1} at 230 GHz is assumed. The κ_0 is based on the case of ice mantle grains following MRN size distribution (Mathis et al., 1977) in Ossenkopf & Henning (1994). In addition, we assume that a gas-to-dust mass ratio of 100. The assumed κ_0 corresponds to the case of $\kappa_\nu = 0.1(\nu/1200\ GHz)^\beta$ with $\beta = 1.39$ (e.g., Hildebrand, 1983; Beckwith & Sargent, 1991). As addressed in Chapter 2, the uncertainty of κ_0 is large, around factor of two (Ossenkopf & Henning, 1994).

It would be good to note how the central protostellar mass affects disk models. A mechanism of protostellar emission is potential energy released from accreting material, which means luminosity of the central protostar depends on its mass, assuming the same accreting radius. In addition, more importantly at this late stage of YSOs more massive protostars have a larger photospheric luminosity at the same age (e.g., Siess et al., 2000). Therefore, more massive protostars induce higher T_0 (refer to Equation 4.3), resulting in a disk mass shift. However, since we set the temperature scaling factor $T_0 = 300$ K at $R_0 = 1$ AU ignoring the luminosity factor, there is no such an effect in our modeling. Rather, the central protostellar mass provides information about disk thickness. More massive central protostars allow a smaller scale height, which means thinner disks (refer to Equation 4.4). In summary, all the parameters to be constrained for the power-law disk model are p, β, M_{disk}, R_{in}, R_{out}, θ_i, PA, and M_*, where θ_i is an inclination angle of a disk (a face-on disk with $\theta_i = 0°$) and PA is a position angle of a disk measured eastward from the north.

Kinematic information obtained from the data sets are not used to constrain disk models in the study here. However, it would be worth attempting to utilize the spectral line data as well to better constrain disk models. Here we use line data only to determine the sign of inclination for HL Tau ($\theta_i > 0°$) and DO Tau ($\theta_i < 0°$) without presenting the data.

4.4.2 Disk Model II: Viscous Accretion Disk

In addition to the power-law disk with a Gaussian edge, a viscous accretion disk model is attempted to fit our data. The viscous accretion disk model has the density distribution form of a power-law disk tapered by an exponential function (e.g., Pringle, 1981). Thin disk models of viscous accretion disks have a surface density distribution expressed as (e.g., Andrews et al., 2009):

$$\Sigma(R) = \Sigma_0\Big(\frac{R}{R_c}\Big)^{-\gamma}\exp\Big[-\Big(\frac{R}{R_c}\Big)^{2-\gamma}\Big], \tag{4.8}$$

where R_c is a characteristic radius. As in the power-law disk model, we assume disk flaring in hydrostatic equilibrium vertically (Equation 4.2, 4.5, and 4.4), so the density and the surface density distributions are:

$$\rho(R,z) = \rho_0\Big(\frac{R}{R_c}\Big)^{-p}\exp\Big[-\Big(\frac{R}{R_c}\Big)^{7/2-p-q/2}\Big]\exp\Big[-\Big(\frac{z}{H(R)}\Big)^2\Big] \quad (4.9)$$

$$\Sigma(R) = \pi^{1/2}\rho_0 H(R_c)\Big(\frac{R}{R_c}\Big)^{3/2-p-q/2}\exp\Big[-\Big(\frac{R}{R_c}\Big)^{7/2-p-q/2}\Big]. \quad (4.10)$$

Note that $\Sigma_0 = \pi^{1/2}\rho_0 H(R_c)$ and $\gamma = -3/2 + p + q/2$, from Equation 4.8 and 4.10. The ρ_0 can be expressed in M_{disk} as:

$$\begin{aligned} M_{disk} &= \int_{-\infty}^{\infty}\int_{R_c}^{\infty}\rho(R,z)\ 2\pi R\ dR\ dz \\ &= \frac{2\pi^{3/2}}{7/2-p-q/2}\rho_0 H(R_c)R_c^2\exp\Big[-\Big(\frac{R_{in}}{R_c}\Big)^{7/2-p-q/2}\Big] \\ \rho_0 &= M_{disk}\Big[\frac{2\pi^{3/2}}{7/2-p-q/2}H(R_c)R_c^2\exp\Big[-\Big(\frac{R_{in}}{R_c}\Big)^{7/2-p-q/2}\Big]\Big]^{-1}. \end{aligned} \quad (4.11)$$

Therefore, the density distribution is presented by M_{disk}, p, β (for q), and R_c. Note that it is the same with the power-law disk model except R_c, which is implanted instead of R_{out}. For this viscous accretion disk model, an outer disk radius is not employed. However, the modeling disks are cut off at 5 R_c due to limitation in image size and for simplicity in integration.

On the other hand, the temperature distribution, sharp inner radius, and κ_ν are assumed as in the power-law disk model. As a result, the parameters to constrain for the viscous accretion disk model are p, β, M_{disk}, R_{in}, R_c, θ_i, PA, and M_*, as in the power-law disk model, except R_c instead of R_{out}.

4.4.3 Model Fitting Procedures

Bayesian inference introduced in Chapter 1 is employed to carry out model fitting. As described in the previous subsections, we use two disk models: a power-law disk with Gaussian boundaries and a viscous accretion disk. In both cases, identical procedures have been carried out, as described in the following.

Disk models are first built in two dimensional logarithmic grids by solving the radiative transfer equation numerically along the line of sight. Note that the disk inclination is applied when constructing the disk model, so the disk model must be two dimensional and the radiative transfer equation is numerically integrated along the third axis, line of sight. No optically thin nor Rayleigh-Jeans approximations are assumed. Afterward, disk images are made by interpolations of the disk models in two dimensional linear pixels. The center

positions and position angles (PAs) of the disks are applied when making the disk images.

The disk images are multiplied by three different normalized primary beams, which correspond to three different kinds of baselines in CARMA: 10.4 m–10.4 m antennas, 10.4 m–6.1 m antennas, and 6.1 m–6.1 m antennas. These three primary beam corrected images are Fourier-transformed into model visibility maps. Then, the actual model visibilities are sampled in the *uv* coverage of observational data by bi-linear interpolation of the model visibility maps. Image pixel sizes and image sizes are selected to obtain reasonable pixel sizes and *uv* coverage of visibility maps. For example, an image pixel size of 9 AU and an image size of 1024 pixel by 1024 pixel are used for HL Tau data, which provide *uv* coverage up to about 1600 $k\lambda$ (a *uv* range: -1604 to +1604 $k\lambda$) and a visibility map pixel of about 3.1 $k\lambda$, based on the Nyquist theorem: for example, the *uv* range $\Delta_{uv} = 1/2\delta_{image}$, where δ_{image} is the image pixel size.

Model fitting is done by comparing observational data with the model data sampled along the observational *uv* coverage. To find the distributions of the parameters for the observational data, we use Bayesian inference, as described in Section 1.3. Gaussian functions are employed for the likelihood, as the noise of interferometric data shows a normal distribution. The uncertainty of each data visibility point is estimated as (e.g., Thompson et al., 2001):

$$\sigma = \frac{2k}{A\eta}\sqrt{\frac{T_1 T_2}{2\Delta\nu t_{int}}}. \tag{4.12}$$

Here k is Boltzmann's constant, A is antenna area, η is the efficiency of the antenna surface and correlator, T_1 and T_2 are system temperatures of antennas corresponding to the baseline, $\Delta\nu$ is bandwidth, and t_{int} is integration time. Note that CARMA measures the efficiencies empirically by interferometric observations (JyperK $= 2k/A/\eta$). Individual wide bandwidth windows of 15 channels ($\Delta\nu \sim 500$ MHz) are averaged and considered a visibility point. The central channel frequency of the window is used for computing its *uv* distance in units of wavelength. As the data are real numbers in image space, i.e., the *uv* coverage is symmetric at the phase center, the symmetric data points are added to the sample. In addition, the real and imaginary components of complex visibility data are regarded as independent data.

Effects of atmospheric turbulence are applied for the uncertainty estimate simply by assuming 30° of phase RMS, resulting in about 15% increase of noise. The atmospheric turbulence effects may cause larger phase scatters at longer *uv* distances. It can typically be seen in gain (phase) calibrator data. When weather conditions (mainly atmospheric phase RMS) are not good, the phase distribution of a gain calibrator shows a conic shape with a larger scatter at longer *uv* distances. Using the gain calibrator phase scatter (RMS) increasing along *uv* distance may provide a way to estimate the atmospheric turbulence effects. The atmospheric phase RMS, which is measured by the CARMA atmospheric phase monitor consisting of two dishes spanning a 100 m baseline and receiving a satellite signal

at about 12.5 GHz, can also be used for the estimate. However, the CARMA atmospheric phase monitor is fixed toward a specific position and at the 100 m baseline, which is too limited to apply to observational data. In addition, since the phase calibrator phase scatter is also dependent on the calibrator flux, it is not straight forward to utilize the atmospheric effects properly. Therefore, we simply apply the atmospheric effects by assuming 30° of phase RMS, resulting in 15% increase of T_{sys}. We point out that it is just a simplest way, since the atmospheric effects vary along *uv* distance and gain calibrator brightness. The atmospheric effects are applied as a factor in the form:

$$T'_{sys} = T_{sys}\exp[(\text{phase RMS in radian})^2/2]. \tag{4.13}$$

Note that we check data quality using phase calibrator amplitudes along *uv* distance and test calibrator images to keep the quality "evenly" across data sets as much as possible.

Searching distributions of model parameters by the Metropolis Hastings method has two parts, as described in Section 1.3. The first part is finding a convergence region of parameters. For a better performance, we start with multiple initial conditions, which are randomly generated. After running for a while, the initial conditions converge into a parameter set (normally two sets with different signs of inclination angles). Annealing is also used to accelerate the convergence. We start a fresh run from the convergent parameter set with a smaller standard deviation of the proposal Gaussian functions. The smaller standard deviation of the proposal functions are set to have an acceptance rate of about 10–50 %. The GASDEV subroutine of the Numerical Recipes using the Box-Muller method is used to produce random numbers in the Gaussian distribution (Press et al., 1996).

4.5 Code Test with Artificial Disk Data

The model fitting code used in this study has been tested by artificial disk data generated by the MIRIAD task IMGEN and UVMODEL. First, noise visibilities have been produced using HL Tau data of A, B, and C configurations at $\lambda = 1.3$ mm, through subtracting HL Tau components from the calibrated data. Afterward, a disk component was made using IMGEN and added to the noise data using UVMODEL. The artificial disk is face-on ($\theta_i = 0°$) and has a power-law intensity distribution of index 3/4: $I_\nu(R) \propto R^{-t}$, where $t = 3/4$. The inner and outer radii of the disk are $0.1''$ and $1.0''$ respectively, which are 15 AU and 150 AU at 150 pc (an assumed distance to the artificial disk). To avoid optically thick effects for a direct comparison with analytical values, total flux of the disk is chosen very small, 6.83 mJy at $\lambda = 1.3$ mm. Accordingly, the noise level of HL Tau has been scaled down by 10^{-5}. The visibility uncertainties determined by T_{sys} were also scaled down by 10^{-6}. The flux of the disk at $\lambda = 2.7$ mm is set to a quarter of the $\lambda = 1.3$ mm flux,

resulting in $\beta = 0$ when the disk is optically thin.

Three minor code modifications have also been made for a direct comparison with analytical solutions. Note that these modifications are only for this artificial disk test. One is the Rayleigh-Jeans approximation, $B_\nu(T) \approx 2kT/\lambda^2$. When assuming the approximation in optically thin objects, the intensity distribution is simply density distribution times temperature distribution. The second one is a sharp outer edge instead of Gaussian edges. In the case of Gaussian edges, analytical solutions can also be obtained easily. However, the simpler sharp edge is just fine for this code test. The last one is a temperature distribution depending on only R, i.e., $T(R)$, instead of $T(r) = T(R, z)$.

To examine if the code converge into a common parameter set, 16 initial conditions have been chosen randomly. Table 4.4 lists the random initial parameter values. Ranges of parameters are 1.15–3.35 for p, -0.35–1.7 for β, 0.0003–0.0030 $M_\odot$ for M_{disk}, 1–20 AU for R_{in}, 40–460 AU for R_{out}, −80–80° for θ_i, 0–180° for PA, and 0.2–5.0 $M_\odot$ for M_*. The first data line of the table shows a set of parameters to fit the artificial disk, which is analytically obtained. As shown in the table, PA can be any value (cannot be constrained), since the disk is face-on. In addition, M_* is not constrained, as the disk is face-on and the temperature is a function of only R (not R and z) in this test. When assuming optically thin and Rayleigh-Jeans approximation, the intensity distribution is corresponding to surface density distribution times temperature distribution: $t = s + q = s + 2/(4+\beta) = p - 3/2 + 3/(4+\beta)$ (Equation 4.5 and 4.3). In other words, this artificial disk of $t = 3/4 = p - 3/2 + 3/(4+\beta)$ has $p = 1.5$ when $\beta = 0$. On the other hand, the disk flux corresponds to a disk mass:

$$\begin{aligned} M_{disk} &= F_\nu D^2 / \kappa_\nu B_\nu(\langle T_d \rangle) \\ &\approx F_\nu D^2 \lambda^2 / 2\kappa_\nu k \langle T_d \rangle \\ &= 0.045/\langle T_d \rangle \ M_\odot, \end{aligned} \tag{4.14}$$

where $F_\nu = 6.83$ mJy, $D = 150$ pc, $\kappa = 0.01$ cm^2 g^{-1}, $\lambda = 1.3$ mm, k is the Boltzmann's constant, and $\langle T \rangle$ is a mean dust temperature of disks. The mean dust temperature of disks is defined as:

$$\begin{aligned} \langle T \rangle &= \frac{\int_{R_{in}}^{R_{out}} \Sigma(R) T_d(R) 2\pi R dR}{\int_{R_{in}}^{R_{out}} \Sigma(R) 2\pi R dR} \\ &= \frac{s-2}{s+q-2} T_0 R_0^q \frac{R_{out}^{-s-q+2} - R_{in}^{-s-q+2}}{R_{out}^{-s+2} - R_{in}^{-s+2}} \left(\frac{L_*}{L_0}\right)^{q/2} \\ &\approx \frac{s-2}{s+q-2} T_0 \left(\frac{R_0}{R_{out}}\right)^q \left(\frac{L_*}{L_0}\right)^{q/2}, \end{aligned} \tag{4.15}$$

where $R_{out} \gg R_{in}$. Therefore, the artificial disk is 0.001366 $M_\odot$, when $L_* = 1.0$ $L_\odot$ and $T_0 = 300$ K at $R_0 = 1$ AU that we assume.

Table 4.5 shows mean parameters of the 16 different initial condition cases after about 6000 proposals have been made. The acceptance rate is about 20–30%, which means each case has about 1000–1800 samples accepted. Also, Table 4.5 has the maximum posterior in individual runs. Note that the listed means of parameters are not necessarily the parameter set giving the maximum posterior. The maximum posterior of individual runs in Table 4.5 increased largely from the initial posterior in Table 4.4.

Based on the comparable posterior of the 16 cases in Table 4.5, they converge into parameters that fit the artificial disk data well. Note that p, β, M_{disk}, R_{in}, R_{out}, and θ_i are very close to the expected values. As mentioned, PA and M_* can be any values in this test. The best fit sample of ID 13 is plotted with the artificial disk visibility data in Figure 4.1. In the figure, open squares and triangles present data at $\lambda = 1.3$ mm and 2.7 mm and the solid lines indicate the best fit model of the ID 13 run. These test results using an artificial disk lead to the conclusion that the code works correctly and has the ability to constrain disk parameters.

4.6 Results

4.6.1 Observational Results

Figure 4.2 and 4.3 present the amplitude distribution (averaged in annulus) along *uv* distance of observational data with the best fitting model overlaid. The left column is the case of the power-law disk model and the right column is for the viscous accretion disk model. In addition, the dust opacity spectral indexes ($\beta \approx \log(F_{1mm}/F_{3mm})/\log(\nu_{1mm}/\nu_{3mm}) - 2$) calculated from the observational data are shown. Note that β in the plots are, therefore, of optically thin and Rayleigh-Jeans approximations. Open squares and open triangles indicate data points of $\lambda = 1.3$ mm and 2.7 mm, respectively. The error bars are calculated in $\Sigma\sigma_i^2/N^2$, where σ_i^2 is the variance of a visibility data point in a annulus calculated from its T_{sys} and N is the total number of data in the annulus. Absolute flux calibration uncertainty is not applied for the plots. As shown, the two models are fitting observational data well. Note that since the viscous accretion disk model does not have an outer radius, there are no step features at around $200 - 300\ k\lambda$, corresponding to about $1''$ (refer to DL Tau and HL Tau plots). Although it is not clear due to large uncertainties, CI Tau, DL Tau, and FT Tau have increasing β with *uv* distance, which can be interpreted as smaller grains at the central region. If it is true, it would be an indirect evidence for inner holes, which might be cleared by protoplanets. On the other hand, Haro 6-13 has a decreasing β trend with *uv* distance; the data of $\lambda = 2.7$ mm get above the model fit, which assumes a constant β. It was seen in envelopes of Chapter 2, for younger YSOs. It is interesting to recognize that Haro 6-13 is the youngest in our sample.

The observational disk images, combined with multiple array data, are shown in the

left column of Figure 4.4 to 4.9 with model (in middle) and residual images (in right). The residual results are discussed later and note that to display two disk models, the observations appear twice. The cross marks indicate the offset positions of disk centers (Table 4.3) and the contour levels are 2.5, 4.0, 6.3, 10, 16 etc. (in logarithm) times σ listed in Table 4.3. The synthesized beams are also marked in the bottom right corner. CI Tau, DL Tau, FT Tau, and HL Tau images are well resolved, and interesting substructures are shown. In particular, substructures of CI Tau and DL Tau are present in the similar pattern at both $\lambda = 1.3$ mm and 2.7 mm maps, which gives better fidelity. Moreover, they look like a spiral structure. These are discussed later. In the case of FT Tau, there is a feature at $\lambda = 2.7$ mm to suggest that it may be a binary system or a nearly edge-on disk with an inner hole. The HL Tau image, in particular at $\lambda = 1.3$ mm, is the best angular resolution image taken at this wavelength ever ($0.13''$ resolution). The disk image clearly shows its geometrical position. DO Tau and Haro 6-13 are not resolved well.

4.6.2 Comments on Model Fitting

Each target has been attempted with 8 randomly chosen initial parameter sets. After running the 8 Markov chains of Metropolis Hastings algorithm long enough to roughly cover the "whole" parameter space, the convergence has been checked. Since we started with a "step" (the standard deviation of the Gaussian proposal functions) corresponding to about one tenth or one twentieth of the range of each parameter, a few hundred samples of each parameter cover the parameter range. Note that the worst case of Markov chains is the random walk, $L \approx \delta\sqrt{N}$ where L is a visited range, δ is a step, and N is the number of samples. It is noteworthy that the widths of proposal functions for individual parameters have been adjusted to have a comparable acceptance rate over parameters first. It is a crucial step to have an efficiently working Markov chain. We also tested a few different step widths for obtaining better flexibility and efficiency (acceptance rate). In addition, to improve the convergence we employed the annealing technique, as introduced in Chapter 1.

In fact, after about 10000 proposals have been made, the multiple chains converged to a similar parameter set for most targets. In a bad quality data set or existence of distinct substructures such as FT Tau, which likely have "deep" local minima, there are multiple converging parameter sets. In such a case, multiple chains have been chosen for the next long run. Note that since we allow a range of -83° to 83° for inclination (our code has not been designed for edge-on disks so it is very slow in such cases) and a range of 0° to 180° for PA, there are roughly the same number of chains converging to either sign of inclination: for example, 4 chains going to about 41° and 4 chains going to about -41° for the HL Tau inclination. If a disk is optically thin, either sign of inclination gives an identical image. In other words, forward and backward half regions of the disk have the same intensity distribution. However, if a disk is not optically thin, the forward half region would be

fainter. It is because the closer part along a line of sight (experiencing less optical depth) on the forward half region is a relatively outer disk portion in the line of sight, which has a lower temperature. Although we compute the optical depth effects correctly, due to a wide gap (e.g., $\sim 80^\circ$ for HL Tau) between the two fine inclination values, it is rarely possible to move from one to the other in a Markov chain. It is why we have both signs of inclination. It would be an option to ignore the optical depth effects and limit the inclination within a sign. However, we intend to examine whether our data allow us to constrain the inclination sign as well. Note that if a disk has a bipolar outflow, the inclination sign can be clearly determined by the blue- and red-shifted portion of the outflow. HL Tau is an example and its inclination should be plus. But we do not use the information as a prior. On the other hand, we may use the results of whether our disk fitting can also constrain the inclination sign based on the clear cases of HL Tau ($\theta_i > 0$) and DO Tau ($\theta_i < 0$).

These 8 chains of each target have been "burned-in" and a fresh long chain for each sign of inclination has been taken from the last parameter set, with smaller widths of proposal functions for a larger acceptance rate (a few tens percent): one quarter of those of the previous chains. In the case of FT Tau, which gives multiple converging parameters, more chains have been chosen, as mentioned. The posterior distributions of parameters have been obtained from the long chains with several tens of thousands trials.

4.6.3 Fitting Results

We present the results of the final runs for 6 targets. Note that we did not use any priors obtained from the images of the targets except the center positions. We tested the center positions determined by a Gaussian fit of the IMFIT task in MIRIAD and the ones manually determined, based on the peak intensity positions. The better offset values, which give higher posteriors at the end, are finally adopted and can be found in Table 4.3.

The fitting results are listed in Table 4.6 and the posterior distributions of parameters in individual targets are presented in Figure 4.10 to 4.15. The parameter ranges to be allowed are also listed in the table. We adopted uniform priors over the ranges. The table values are the means of individual parameters weighted by the posterior and the errors are the standard deviation of the posterior distribution. The solid lines of Figure 4.10 to 4.15 indicate normal distributions at the posterior weighted means with the standard deviation. As shown, most of parameters have a normal distribution posterior. However, as expected, when parameters are limited by the search range, there is a shift between the posterior distribution and its normal distribution match: e.g., M_* (M_{cen} in the plots) of CI Tau in both models. In addition, some parameters do not seem to have a normal distribution: e.g., M_{disk} of Haro 6-13 in both models. It may indicate that the disk mass cannot be constrained well by these models. Otherwise, it may indicate that the sample is just not large enough.

The volume density distribution index (p) of the power-law disk model is between 1.7 to 3.26, which correspond to surface density index (s) between 0.43 and 2.00 ($s = p - 3/2 + 1/(4+\beta)$ in Section 4.4). The surface density index is distributed in a quite large range and CI Tau has the most similar value with the solar nebular's ($\sim$ 1.5: Weidenschilling, 1977). It is noteworthy that the large $p \sim 3.25$ ($s \sim 2.0$) of DO Tau and Haro 6-13 can be because the targets have not been resolved. The outer radius of very large values (around 460 AU, the upper limit) also makes it suspicious. On the other hand, the p of the accretion disk model can be converted into γ expressing the surface density distribution (Equation 4.8) by $\gamma = p - 3/2 + 1/(4 + \beta)$. As shown in Table 4.6, γ of our sample disks are distributed from -0.69 to 1.99. Such a large range of γ has been reported by recent other studies (Isella et al., 2009; Andrews et al., 2009).

The dust opacity spectral index β and disk masses appear to be constrained very closely in the two models. It is natural because β is sensitive to the difference of flux densities at two wavelengths and a disk mass is mainly constrained by the total flux. β of our sample disks ranges from -0.04 to 0.75. The negative values of CI Tau and FT Tau probably indicate absolute flux calibration errors. In most targets except DL Tau and HL Tau, β values are around 0, which can be interpreted as grain growth. We estimated that β of Class 0 YSOs is around 1 in Chapter 2, so grains may be grown much further. It is valid even for DL Tau and HL Tau, since they have β smaller than 1. Disk masses are around 0.015–0.095 $M_\odot$. FT Tau, which is possibly a binary system, appears to have the least disk mass in our sample and HL Tau has the largest mass. Note that the disk mass has a large uncertainty because κ_0 has a factor of two uncertainty (e.g., Ossenkopf & Henning, 1994) and T_0 (temperature at R_0) is fixed in our modeling. However, the effects on the disk mass of the fixed T_0 are not significant, since T_0 is weakly sensitive to the luminosity of the central protostar.

The inner radii of disks have been fitted between 0.7 to 15 AU in both models. These large radii, larger than the dust grain sublimation radius, might indicate inner holes cleared up by protoplanets. Moreover, the increasing β with uv distance (Figure 4.2 and 4.3) might also support this idea. Although we warn that our data set might not allow us to constrain the inner radius decisively due to still lack of angular resolution, the fact that the models with a large inner radius better fit data is noteworthy. Both models give a similar inner radius for most disks, except DL Tau.

Since our data sets resolve the disks well except DO Tau and Haro 6-13, the outer radius is well constrained, distributed between several tens and a few hundreds AU. Since we use a Gaussian edge for the power-law disk model, the outer radius tends to be constrained smaller than the power-law disk model with a sharp edge, which has been used in previous studies (e.g., Mundy et al., 1996; Andrews & Williams, 2005). On the other hand, the accretion disk model constrains the characteristic radius instead, which is where the disk density distribution changes from the power-law dominant region to the exponential dominant re-

gion (Equation 4.8). Comparing the surface density equation of our accretion disk model with a similarity solution of viscous accretion disks and considering the mass flow equation (e.g., Andrews et al., 2009; Hartmann et al., 1998; Pringle, 1981), the characteristic radius can express the transitional radius R_t, where the bulk flow direction changes from inward to outward to conserve angular momentum (e.g., Equation A9 in Andrews et al., 2009):

$$R_t = R_c\Big[\frac{1}{2(2-\gamma)}\Big]^{1/(2-\gamma)}. \tag{4.16}$$

The R_t of our sample disks are in a range of 32 to 80 AU, as listed in Table 4.6.

The two geometrical parameters, inclination (θ_i) and position angle (PA), are well constrained. The values are consistent with previous high angular resolution observations (e.g., HL Tau: Mundy et al., 1996) and are self-explainable by the image itself. The DO Tau and the HL Tau inclination angles are constrained with the right sign (consistent with blue/redshifted bipolar outflow regions) in both models. The two targets have clear disk orientation and bipolar outflow features. Besides, the inclination of DL Tau is also constrained with the same sign in both models, which make the value more reliable. However, the other three targets have inclinations with different signs in the two models.

The parameter M_* is interesting, since it can indicate dust settlement. The idea is that if M_* is larger than the protostellar mass spectrophotometrically measured, the disk is thinner than that in hydrostatic equilibrium. The most distinct case is DL Tau; only DL Tau has large M_* in both disk models. Based on its large M_*, DL Tau appears to have a smaller scale height than that estimated from hydrostatic equilibrium. It means that dust settling is likely to have been undertaken. Interestingly, Furlan et al. (2009) exactly support the dust settling with small n_{13-31} and EW(10 μm) values. Note that EW(10 μm) indicates the amount of small (< 5 μm) silicate grains and n_{13-31} represents the flareness of disks by intervening of protostellar emission. Additionally, many substructures have been detected in DL Tau.

4.7 Discussion

4.7.1 Correlation between Properties

We calculate correlation coefficients between properties of circumstellar disks and central protostars, in order to find any possible relationship between them. The correlation coefficients are calculated as:

$$R_{xy} = \frac{\Sigma(x_i-\bar{x})(y_i-\bar{y})}{\sqrt{\Sigma(x_i-\bar{x})^2}\sqrt{\Sigma(y_i-\bar{y})^2}}, \tag{4.17}$$

where $\bar{x}$ and $\bar{y}$ are means of $\{x_i\}$ and $\{y_i\}$, respectively. One of the properties we have for protostars is the ages (Age_B) reported by Beckwith et al. (1990). In addition, we attempt

a new age estimate (Age_S) by Siess et al. (2000), which provides a web-based tool, and the values are in Table 4.7. The same T_{eff} and L_* of Beckwith et al. (1990) are also used for the latter case. Therefore, FT Tau whose effective temperature has not been reported is excluded for the age estimate. The EW(10μm) and n_{13-31} reported by Furlan et al. (2009) are also considered (Table 4.1), presumably indicating dust evolution of disks. In addition, the constrained properties, s, β, M_{disk}, R_{in}, R_{out}, and M_* for the power-law disk model and γ, β, M_{disk}, R_{in}, R_t, and M_* are taken into account. One last thing we have is the disk accretion rate per unit mass using the disk mass accretion rate estimated by SED fitting (Robitaille et al., 2007). The values are in Table 4.7.

The correlation coefficients are presented in Table 4.8 and strong correlations (> 0.8) have been emphasized with a bold font. The table includes a lot of information. Among them a few correlations (underlined in the table) may need to be noted at least, although our sample size is small. In the power-law disk model, the surface density index appears to be anti-correlated with the Age_B, which means that as disks evolve the density gradient decreases. This trend also appears in the accretion disk model. In addition, less massive disks have smaller β values. It can imply that there may be more hidden mass in more evolved disks with larger grains. On the other hand, it could be interpreted simply as disks with larger grains are less massive. However, considering that the continuum emission per unit grain mass decreases, the former interpretation is arguably preferred. Besides, the accretion rate appears to be anti-correlated with Age_S. It may indicate that there is a common accretion mechanism regardless of disk masses and the mechanism efficiency decreases with time. On the other hand, it may show that the protostellar age and the disk age are consistent. The anti-correlation between n'_{13} and M_* shown in the accretion disk model, in other words, the trend that thinner disks have smaller n'_{13-31} verifies the usefulness of n'_{13-31} to measure the flareness of disks. It is not shown in the power-law disk model. However, we do not see the trend of R_t increasing with time, which Isella et al. (2009) reported using a two thin layer model. Recently, Andrews et al. (2009) did not see the trend either. As they addressed, it might be due to our small number of sample or due to model differences. Also, the trend of dust grain settlement is not clear. There is no clear correlation between protostellar ages and M_*, which is used as a ruler of the disk thickness in our modeling.

4.7.2 Protoplanet Candidate around HL Tau and Substructures of Disks

Figure 4.4 to 4.9 show interesting substructures and residuals of targets. In this section, we discuss them focusing on HL Tau. As introduced in Section 4.2, there is a study to claim a protoplanet candidate around HL Tau at about 65 AU northwest of the center detected at $\lambda = 1.3$ cm (Greaves et al., 2008). However, since free-free emission (non dust thermal emission) is significant at the wavelength, it was not clear whether the emission

excess indicates a small companion. In addition, Carrasco-González et al. (2009) did not find a corresponding signal at $\lambda = 7$ mm. The best opportunity to figure out whether there is a protoplanet or not is shorter millimeter wavelength observations (sensitive to dust continuum and little bias from free-free emission) with high angular resolution. Therefore, our observations toward HL Tau provide the best opportunity to search for a protoplanet and/or substructure.

The observational maps of the left column in Figure 4.9 do not highlight any interesting substructure. However, the residual maps of the right column feature distinct structures. As discussed in the next section (Section 4.7.3), HL Tau prefers the accretion disk model, which means that the residual map of the accretion disk model is more reliable. Therefore, we focus on the residual map of the accretion disk model. First, there is a narrow dust lane spanning from the northwest to the north of the center in an arc at the residual map of $\lambda = 1.3$ mm. The end of the northwest is the direction where (Greaves et al., 2008) suggested a small companion. However, our dust lane is $0.2''$ further out than their position. Greaves et al. (2008) reported a flux of ~ 8 μJy at $\lambda = 1.3$ cm for their protoplanet candidate. When considering a spectral index of ~ 2.75 as the case of optically thin with $\beta = 0.75$, the flux at $\lambda = 1.3$ mm would be ~ 4 mJy, which should be detected in our map with S/N ~ 4. Note that the companion would be smaller than our synthesized beam so the flux per beam could be considered as the object total flux. Therefore, it is unlikely that the small compact signal detected by Greaves et al. (2008) is a protoplanet candidate.

The arc structure of the dust lane is very interesting. Considering the inclination and the position angle, the arc is spanning around the same radius from the center, about 100 AU. Nero & Bjorkman (2009) studied possibility of planet formation by disk fragmentation in three disks including HL Tau, considering cooling time and the Toomre Q parameter to indicate gravitational instability. The required shorter cooling time of a perturbation sets the upper limit of surface density, while the Q parameter constrains the lower limit. What they found is that in the case of HL Tau, the disk mass range that can fragment is between 0.04-0.09 $M_\odot$when the surface density index $s = 0.5$ and the region is out of about 50 AU. These are satisfied by the dust lane but we calculated the Q parameter to have a better idea.

The Q parameter is defined as (Toomre, 1964),

$$Q \equiv \frac{c_s \Omega}{\pi G \Sigma}, \tag{4.18}$$

where c_s is the isothermal sound speed, Ω is the orbital angular velocity, G is the gravitational constant, and Σ is the surface density, and it indicates where is gravitationally unstable ($Q \lesssim 1$). As we constrained disk temperature and density distributions, the Q parameter can be calculated assuming a Keplerian rotation of disks. Since $\Sigma = \sqrt{\pi} H \rho$,

$H = \sqrt{2}c_s/\Omega'$, and $\Omega = \sqrt{GM/R^3}$,

$$Q = \frac{\Omega\Omega'}{\pi\sqrt{2\pi}G\rho} = \frac{\sqrt{M_* M_{*dyn}}}{\pi\sqrt{2\pi}R^3\rho}. \tag{4.19}$$

Note that the density at the midplane is used, and since we adopted M_* for the disk geometry, Ω and Ω' are distinguished. Figure 4.16 shows the Q parameter along radius in both the power-law disk and the accretion disk models. The weighted mean values of parameters are used and $M_{*dyn} = 0.5$ $M_\odot$ is assumed for all targets. As shown in the figure, HL Tau has a minimum Q value very close to 1 around 100 AU, which means that substructures by gravitational instability can develop in the region. This is exactly what we detected in the residual map: a dust lane at about 100 AU of radius. Furthermore, looking at the map closer (Figure 4.17), there are even a few blobs. Based on Nero & Bjorkman (2009), the fragment mass can be estimated by

$$M_f \sim 1 M_{Jupiter} \Big(\frac{\Sigma}{10 \text{ g cm}^{-2}}\Big)^{3/2} \Big(\frac{M_{*dyn}}{M_\odot}\Big)^{-1/2} \Big(\frac{r}{100 \text{ AU}}\Big)^3. \tag{4.20}$$

As HL Tau has $\Sigma \approx 17.3$ g cm^{-2} at 100 AU and $M_{*dyn} \approx 0.5$ $M_\odot$, the fragment mass would be about 3 $M_{Jupiter}$. These dust lane and blobs are promising for a site to develop protoplanets, based on the observations and theoretical studies.

HL Tau has more substructures, which are positive residuals around the center in the $\lambda = 1.3$ mm and 2.7 mm maps and northeast and southeast blobs at $\lambda = 2.7$ mm. The central residuals may indicate the cavity walls of a bipolar outflow. The northeast appears to be the blueshifted portion of a bipolar outflow in our CO $J = 2 \rightarrow 1$ data (Kwon et al. in preparation), so the northeastern side may get hotter by the protostellar emission than the other side. The temperature difference can cause positive residuals anti-symmetrically at the two wavelengths. The residuals shown in Haro 6-13 can also be explained by the bipolar outflow cavity. On the other hand, the blobs of the $\lambda = 2.7$ mm residual maps might be a cold extension of the dust lane.

The substructures and residuals of CI Tau, DL Tau, and FT Tau might not be explained by the Q parameters, since the values appear to be in the gravitationally stable region, $Q > 5$. However, we suggest that they may have "hidden" mass in the cold midplane and/or large grains, based on the substructures. As the features of CI Tau and DL Tau appear at both wavelength maps in the same pattern, they are likely to be real structures. The correlation between β and disk mass also supports this idea, as addressed in Section 4.7.1. FT Tau has a feature of a binary system or a nearly edge-on disk with a hole. Therefore, although the fitting with a single disk is fine based on the residual, the special features are not explained by the single disk model with an intermediate inclination. More careful modelings with flexible offset positions may be required. Although the position

angles are constrained as about 160° in the two models, the central elongated feature is along $\sim 30°$. Further observations using high angular resolution at $\lambda = 1.3$ mm, in which dust continuum is stronger, may reveal interesting features toward this object.

Particularly, the substructures of CI Tau and DL Tau resemble spiral structures. The trailing spiral structure built by gravitationally instability is an efficient mechanism to transport angular momentum outward (e.g., Hartmann, 2001). Therefore, if we could obtain the kinematics of the features, it will allow us to study the accretion mechanism. While the accretion mechanism of the gravitational instability generally appears in the outer disk region, the most successful mechanism to explain angular momentum transport in the accretion disks is the magnetorotational instability (MRI) (e.g., Balbus, 2003). The key aspects MRI requires are magnetic fields coupled with material to act as a tension and disk rotational velocities decreasing outward. As with the trailing spiral arms, in which the gravity of the mass excess acts as a tension, a faster rotating inner region is dragged by the slower rotating outer region connected by the magnetic field tension. Therefore, angular momentum is transported outward. The rotation decreasing outward is a general property of circumstellar disks, whose velocity appears Keplerian. For the former aspect of magnetic fields coupled with disk material, the key property of disks is ionization fraction. Gammie (1996) tackled which parts of disks are coupled with magnetic fields and suggested a layered accretion disk. While the inner region (< 0.1 AU) is collisionally ionized, the outer region is layered with accretionally active (ionized enough by cosmic rays) and dead zones (cold midplane).

A nice aspect of the viscous accretion disk model, which is one of the models we employed, is that it provides a means to investigate the physical origin of viscosity. Viscosity of disks is normally parameterized as $\nu = \alpha c_s H$, where α is a dimensionless parameter, c_s is a sound speed, and H is a scale height (e.g., Shakura & Sunyaev, 1973). On the other hand, since the mass accretion rate is related to the viscosity in a structure-determined disk (e.g., Equation A10 in Andrews et al., 2009), we can estimate the α parameter of our disk models fitting data, assuming an accretion rate. For this calculation, we use the mass accretion rate estimated by Robitaille et al. (2007) using SED fitting (Table 4.7) and the equation derived by Andrews et al. (2009):

$$\alpha \approx \frac{2R_c^2}{3(2-\gamma)} \frac{\dot{M}_*}{M_d} \Big(\frac{R}{R_c}\Big)^{\gamma} \frac{1}{c_s H}. \tag{4.21}$$

α is a function of radius but we calculated only the values at 10 AU and 100 AU in Table 4.7. The α values at 10 and 100 AU of our sample disks are all in the range that MRI can be the viscosity origin for: 0.005–0.6 (Balbus, 2003), except FT Tau at 100 AU. However, since the fitting is not good for FT Tau and the investigation of the viscosity origin is beyond the scope of this study, further attempts to understand the exception are not made.

4.7.3 Disk Model Comparison

We employed two disk models: the power-law disk and the viscous accretion disk. The former has been used in the past 20 years for interferometric data modeling as well as SED data modeling. However, there is no fundamental physics behind it, although it gives a successful fit for the solar nebula and high angular resolution observations, and some numerical simulation shows the relation. In addition, it could not explain the disk size differences detected in dust continuum and gas spectral lines, since the model was assumed to have a sharp outer radius. On the other hand, the viscous accretion disk model better provides a disk structure to explain the different sizes observed in dust continuum and in gas (Hughes et al., 2008), as it does not have an outer radius. Instead, it has a form of a power-law disk tapered by an exponential function. Additionally, it is based on a physics of viscous accretion to conserve angular momentum.

However, there is no quantitative comparison between the two models yet. In addition, it is not clear if the better explanation by the accretion disk model is just due to the boundaries. Therefore, we compare the viscous accretion disk model with a power-law disk having a Gaussian edge. As introduced in Chapter 1, Bayesian inference provides a way for model comparison; models can be compared by evidence, which is the integration of likelihood times prior over the whole possible parameter space of a model. We set the prior as well as the number of free parameters are the same for the two models (uniform priors over the same ranges), so we just need to integrate likelihood. The likelihood integration can be estimated by the best likelihood times the posterior accessible volume:

$$\begin{aligned} K &= \frac{P(D \mid H_P)}{P(D \mid H_A)} \\ &= \frac{\int dm P(D \mid m, H_P) P(m \mid H_P)}{\int dm P(D \mid m, H_A) P(m \mid H_A)} \\ &\approx \frac{P(D \mid m_{best}, H_P) P(m_{best} \mid H_P) \sigma_{(m|D)_P}}{P(D \mid m_{best}, H_A) P(m_{best} \mid H_A) \sigma_{(m|D)_A}} \\ &\approx \frac{P(D \mid m_{best}, H_P) \sigma_{(m|D)_P}}{P(D \mid m_{best}, H_A) \sigma_{(m|D)_A}}, \end{aligned} \tag{4.22}$$

where the subscript P and A indicate the power-law disk model and the accretion disk model, respectively. The posterior accessible volume is estimated by $\sigma_{(m|D)} = \Pi \sigma_i$, where σ_i is posterior widths of p, β, M_{disk}, R_{in}, R_{out} (or R_c), θ_i, PA, and M_*.

The K values of our targets are shown in Table 4.9 with the evidence of the two models. As shown in the table, none of the models is preferred by all disks, rather quite even. Note that since we have some posterior distribution is limited by the search range of parameters (e.g., M_* in CI Tau), some evidence could be underestimated. Thus we do not count on a small difference in $\ln(K)$. Particularly, the less resolved disk Haro 6-13 appears to be nearly

equal in the two models. However, we found two distinct cases: DL Tau and HL Tau. The power-law disk model is preferred by DL Tau over the accretion disk model and vice versa by HL Tau.

DL Tau is the oldest in our sample and shows interesting substructures. In addition, it has the lowest mass accretion rate per unit disk mass. Therefore, it may imply that T Tauri disks become a power-law disk, as they evolve and have less accretion. The accretion disk model can have such a trend (Equation 4.8) if γ gets larger with time, as the density distribution is closer to a power-law with larger γ. However, the accretion model may be limited to a specific "power-law" index (e.g., 2) and we obtained the opposite result: γ anti-correlated with age. As a result, we suggest that the accretion disk may not be preferred by more evolved disks like DL Tau. In addition, it may result in a large range of γ detected in the recent disk survey results (Isella et al., 2009; Andrews et al., 2009).

On the other hand, HL Tau, in which the accretion disk model is preferred, has a strong bipolar outflow and a high accretion rate per unit disk mass. Thus, the accretion disk model is preferred by a disk with strong accretion indeed. However, it is noteworthy that HL Tau may have a weak envelope component (note the very small M_*, limited by the prior range, meaning large flareness) so another model considering an envelope component would be preferred over the two models. In other words, note that the model comparison here is only limited to the two disk models.

4.8 Conclusion

We have been carrying out a T Tauri disk survey using CARMA, which provides the unprecedented image fidelity and angular resolution. So far, we have achieved multi-wavelength ($\lambda = 1.3$ mm and 2.7 mm) and multi-configuration (A, B, C, and/or D) data up to angular resolution of $0.13''$ toward 6 targets: CI Tau, DL Tau, DO Tau, FT Tau, Haro 6-13, and HL Tau. Using Bayesian inference, we obtained disk properties of the viscous accretion disk model as well as the power-law disk model, such as density distribution, dust opacity spectral index, disk mass, disk inner and outer radii, inclination, position angle, and disk thickness (scale height factor).

First, we found interesting features of substructures and residuals:

1. HL Tau has a dust lane at 100 AU in an arc, although we did not find any compact feature at the position where a protoplanet candidate has been claimed. The region is gravitationally unstable based on the Toomre Q parameter and can be fragmented. Indeed, there are a few blobs in the lane, which possibly develop $\sim$3 $M_{Jupiter}$ protoplanets.

2. CI Tau and DL Tau show a spiral-like pattern in both wavelength maps and FT Tau has a feature of a binary system or a single edge-on disk with a hole.

Second, we detected anti/correlation between properties of protostars and circumstellar

disks:

3. The protostellar age is anti-correlated with the disk density distribution index. In other words, the older disks have the shallower density gradient along radius.

4. The opacity spectral index β is correlated with disk mass, which means that the less massive disks have a smaller β. It may imply more non-detectable mass in the cold midplane and/or in large grains of disks with a smaller β.

5. The accretion rate per unit disk mass decreases with the protostellar age.

Finally, the two models have been compared to examine which model is preferred for our sample disks. What we found is:

6. None of the two models is preferred by all our disks, rather evenly preferred. There are two distinct cases; DL Tau prefers the power-law disk model and HL Tau prefers the accretion disk model. While HL Tau has a strong bipolar outflow and accretion, DL Tau is the oldest in our sample and it has a low mass accretion rate. Therefore, we suggest that the power-law disk model is preferred by more evolved disks with less accretion over the accretion disk model.

Table 4.1 Disk targets. Information comes from literature: the effective temperature, luminosity, mass, and age of the central protostars (Beckwith et al., 1990), the spectral types of the central protostars and YSO class (Kenyon & Hartmann, 1995), and the equivalent width of 10 μm features and the spectral indexes between $\lambda = 13$ and 31 μm (Furlan et al., 2009). The protostellar spectral type of Haro 6-13 is based on Andrews & Williams (2005). The positions are phase centers of the observations. Actual target centers are offset from them.

Targets	Positions (J2000)		ST	Class	T_{eff}	L_*	Age	M_*	EW(10μm)	n_{13-31}
	h m s	$^\circ$ $'$ $''$			[K]	[L$\odot$]	[10^6 years]	[M$\odot$]		
CI Tau	04 33 52.000	+22 50 30.20	K7	II	4000	1.14	0.79	0.70	2.55	-0.17
DL Tau	04 33 39.076	+25 20 38.14	K7	II	3890	0.77	1.20	0.56	0.51	-0.77
DO Tau	04 38 28.583	+26 10 49.85	M0	II	4000	1.38	0.60	0.72	0.94	-0.13
FT Tau	04 23 39.178	+24 56 14.30	–	II	3890	–	–	–	1.86	-0.46
Haro 6-13	04 32 15.410	+24 28 59.97	M0	I/II	3890	2.10	0.13	0.55	3.87	0.38
HL Tau	04 31 38.471	+18 13 58.11	K7	II	3890	0.90	0.95	0.55	–	–

Table 4.2 Protoplanetary disk observations

Targets	Obs. Dates	Array	Wavelengths	Flux cal.	Gain cal.	Test cal.
CI Tau	2007 Sep. 18	C	1 mm	Mars	0530+135 (3.0)	
CI Tau	2007 Nov. 25	B	1 mm	MWC349 (1.9)	0530+135 (2.4), 0510+180 (0.8), 3C84 (4.2)	0431+206 (0.034-0.045)
CI Tau	2008 Jan. 18	B	3 mm	MWC349 (1.3)	0530+135 (3.8), 3C84 (7.1), 0510+180 (0.8)	
CI Tau	2008 Jun. 13	D	1 mm	Uranus	0530+135 (1.6), 3C111 (1.7)	
CI Tau	2008 Oct. 29	C	3 mm	3C273 (14)	0530+135 (2.0)	0431+206 (0.15)
CI Tau	2009 Mar. 30	D	3 mm	Uranus	0510+180 (1.1), 3C111 (2.8)	0431+206 (0.14-0.15)
DL Tau	2008 Oct. 21	C	3 mm	Uranus	0530+135 (2.0), 3C111 (6.5)	0431+206 (0.13)
DL Tau	2008 Oct. 29	C	3 mm	Uranus	0530+135 (2.0), 3C111 (6.5)	0431+206 (0.13)
DL Tau	2008 Dec. 11	B	1 mm	3C84 (5.0)	0510+180 (1.1)	0431+206 (0.05)
DL Tau	2008 Dec. 14	B	1 mm	3C84 (5.0)	0510+180 (1.1)	0431+206 (0.05)
DL Tau	2009 Jan. 21	A	3 mm	3C454.3 (10)	0510+180 (1.3), 3C111 (3.8)	0431+206 (0.05-0.08)*
DL Tau	2009 Jan. 22	A	3 mm	3C84 (9.0)	0510+180 (1.3)	0431+206 (0.05-0.09)*
DL Tau	2009 Mar. 11	D	1 mm	Uranus	0510+180 (0.9), 3C111 (2.3)	0431+206 (0.055)
DO Tau	2007 Nov. 27	B	1 mm	MWC349 (1.9)	0530+135 (2.4)	0431+206 (0.038-0.057)
DO Tau	2008 Oct. 18	C	3 mm	3C84 (9.0)	0530+135 (2.0)	0431+206 (0.13)
DO Tau	2008 Oct. 28	C	3 mm	Uranus	0530+135 (2.0), 3C111 (6.9)	0431+206 (0.14)
DO Tau	2008 Oct. 28	C	3 mm	3C84 (9.0)	0530+135 (2.0)	0431+206 (0.14)
DO Tau	2009 Mar. 27	D	1 mm	Uranus	0510+180 (0.8), 3C111 (2.0)	0431+206 (0.05)
FT Tau	2008 Aug. 26	D	1 mm	3C84 (4.2)	0530+135 (1.5), 3C111 (1.5)	
FT Tau	2008 Oct. 15	C	1 mm	Uranus	0530+135 (1.1), 3C111 (4.3)	0357+233 (0.35)
FT Tau	2008 Oct. 26	C	3 mm	3C454.3 (20)	0530+135 (2.0), 3C111 (7.2)	0357+233 (0.43)
FT Tau	2009 Feb. 15	A	3 mm	Uranus	0510+180 (1.3), 3C111 (3.5)	0431+206 (0.03)*
Haro 6-13	2008 Jan. 12	B	1 mm	3C454.3 (11)	0530+135 (2.2)	0510+180 (0.58-0.74)
Haro 6-13	2008 Apr. 25	C	1 mm	Uranus	0530+135 (2.0), 3C111 (1.9)	
Haro 6-13	2008 Jul. 1	D	1 mm	Uranus	0530+135 (1.6), 3C111 (1.7)	
Haro 6-13	2009 Jan. 4	B	3 mm	Uranus	0510+180 (1.3)	0431+206 (0.16)
Haro 6-13	2009 Apr. 18	C	3 mm	Uranus	0510+180 (1.0), 3C111 (2.6)	0431+206 (0.11-0.15)
HL Tau	2007 Nov. 4	C	1 mm	Uranus	0530+135 (2.6)	
HL Tau	2008 Feb. 16	B	3 mm	Uranus	0530+135 (4.0), 3C111 (6.7)	0510+180 (1.0-1.2)
HL Tau	2008 Oct. 27	C	3 mm	Uranus	0530+135 (2.0)	0431+206 (0.13-0.15)
HL Tau	2009 Jan. 1	B	1 mm	3C84 (4.5)	0510+180 (0.9)	0431+206 (0.04-0.05)
HL Tau	2009 Jan. 17	A	1 mm		0510+180 (0.9)	0431+206 (0.02)
HL Tau	2009 Jan. 31	A	1 mm	3C84	0510+180 (0.9)	0431+206 (0.02-0.03)

Table 4.3 Reduced data sets

Targets	Arrays	Freq. [GHz]	*uv* coverage [kλ]	Beam (PA) [$''\times''$ ($^\circ$)]	RMS [mJy beam^{-1}]	Gaussian fit sizes (PA) [$''\times''$ ($^\circ$)]	ΔRA [$''$]	ΔDec [$''$]
CI Tau	BCD	229	6.8—726.5	0.44×0.29 (-76)	2.0	0.80×0.37 (-31)	0.26	-0.21
	BCD	113	3.9—363.8	1.00×0.76 (87)	0.6	1.08×0.62 (85)		
DL Tau	BD	229	8.5—723.8	0.49×0.28 (83)	1.1	0.76×0.63 (53)	0.10	-0.24
	AC	113	7.4—727.6	0.31×0.25 (-81)	0.5	1.01×0.59 (6)		
DO Tau	BD	229	7.0—604.1	0.44×0.37 (72)	2.4	0.83×0.41 (51)	0.06	-0.54
	C	113	8.3—143.8	1.63×1.11 (83)	0.8	0.49×0.14 (32)		
FT Tau	CD	229	7.5—287.1	0.88×0.60 (82)	1.4	0.95×0.37 (-3)	0.18	-0.32
	AC	113	4.1—727.6	0.31×0.27 (-25)	0.6	0.78×0.51 (71)		
Haro 6-13	BC	229	12.3—616.6	0.52×0.39 (-61)	2.3	0.34×0.25 (1)	0.14	-0.56
	BC	113	8.0—365.4	0.84×0.64 (-90)	0.7	point		
HL Tau	ABC	229	15.5—1452.0	0.17×0.13 (85)	0.9	0.80×0.62 (-48)	-0.76	-0.74
	BC	112	8.0—359.0	0.98×0.70 (80)	1.1	0.77×0.68 (-57)		

Table 4.4 Random initial parameter values to fit the artificial disk

ID	p	β	M_{disk}	R_{in}	R_{out}	θ_i	PA	M_*	ln(posterior)
			[$M_\odot$]	[AU]	[AU]	[°]	[°]	[$M_\odot$]	
	1.50000	0.00000	0.0013660	15.00000	150.0000	0.0000	———	———	
1	2.78783	1.69556	0.0023102	1.98683	75.2268	64.0614	167.5144	0.4866569	-7.8985987904E+08
2	2.08696	1.58828	0.0006993	1.99078	352.2446	-58.8183	111.0579	1.4613461	-1.8445581212E+06
3	1.97350	1.53475	0.0028602	6.57020	83.5028	38.1936	3.1449	4.5007005	-4.0712576037E+08
4	2.41828	0.26287	0.0027446	7.98777	352.2101	-29.2115	85.4808	3.6187177	-8.4139300099E+06
5	2.89364	0.72043	0.0014587	9.11560	334.2396	-31.7199	14.3142	2.4647405	-1.3296131647E+07
6	1.61211	-0.31364	0.0026997	13.48814	321.6044	-40.7358	31.2178	0.4016203	-1.7142829228E+06
7	2.43719	0.07145	0.0025414	18.07534	237.9505	36.2952	91.3859	4.9953508	-7.0421966392E+06
8	2.34618	0.43029	0.0003929	1.24725	134.3350	31.7723	17.0043	0.8719709	-2.0596771734E+06
9	2.86267	0.66715	0.0025554	4.77866	360.6638	24.1483	156.6417	0.9336945	-8.2774785441E+07
10	2.70519	-0.18358	0.0017704	15.89647	195.1954	-0.8326	60.3080	2.8701406	-5.3834642963E+06
11	2.80335	1.49319	0.0010050	10.16538	370.0411	32.0070	87.1890	1.8956110	-3.6826668403E+06
12	1.31539	0.27500	0.0003324	11.92023	222.8686	-17.6507	71.1254	2.1140161	-4.8721728288E+06
13	1.22397	1.06035	0.0015329	5.30198	288.9479	-43.2691	149.9517	0.3254254	-2.7044189388E+06
14	2.10401	0.97296	0.0009456	1.92674	251.7285	-43.8091	117.8400	1.9271222	-9.9826506093E+05
15	2.56369	1.13733	0.0014343	14.10224	355.2610	-51.8000	47.8713	1.2445998	-3.1567940671E+06
16	1.73945	1.34138	0.0012109	10.12353	117.1968	10.6275	27.3876	4.8607831	-9.7649312770E+06

Table 4.5 Mean parameters after about 6000 proposals

ID	ln(posterior)	Proposals	p	β	M_{disk}	R_{in}	R_{out}	θ_i	PA	M_*
					[$M_\odot$]	[AU]	[AU]	[°]	[°]	[$M_\odot$]
			1.50000	0.00000	0.00137	15.00000	150.00000	0.00000	———	———
1	-2.3793251220E+03	5927	1.51374	0.01377	0.00136	14.69109	150.25026	2.25605	179.35664	0.23015
2	-2.3642839053E+03	5862	1.51588	0.00724	0.00137	14.67945	150.56906	-3.56951	89.43077	1.85363
3	-2.3204676134E+03	5704	1.49872	-0.00672	0.00138	14.39079	150.17022	3.52123	0.82930	4.40784
4	-2.4036444927E+03	6192	1.51077	-0.01286	0.00139	14.84561	150.93400	-5.15682	91.05488	4.61245
5	-2.4258569139E+03	6126	1.52587	0.00913	0.00137	15.09886	150.54282	-2.50169	0.65266	1.16094
6	-2.5134943488E+03	5870	1.52785	-0.00210	0.00138	15.22609	151.29850	-6.34421	0.72240	0.33059
7	-2.3216081472E+03	7352	1.50477	-0.00280	0.00138	14.57862	150.43224	4.10963	89.75163	4.49024
8	-2.3707913430E+03	7351	1.49365	0.00896	0.00135	13.96492	148.79346	0.00812	49.65558	0.46221
9	-2.6891238576E+03	6598	1.53915	-0.00241	0.00138	15.87452	151.24467	5.26779	168.27153	0.25809
10	-2.3259233971E+03	6287	1.49881	-0.00440	0.00138	14.20861	150.06911	0.43656	47.75050	2.88662
11	-2.9081441675E+03	6222	1.55313	0.01003	0.00138	16.28164	151.65661	6.32400	1.32156	0.20016
12	-2.3411334339E+03	6030	1.49021	0.00829	0.00136	13.80861	149.24876	-0.04378	88.61064	2.45614
13	-2.3162503138E+03	6662	1.49505	-0.00540	0.00138	14.30971	149.84627	-1.59161	90.24160	0.76401
14	-2.3594104285E+03	6518	1.50988	0.00715	0.00137	14.72919	149.88460	0.00080	96.30073	1.24545
15	-2.4470896097E+03	6492	1.52676	0.00061	0.00138	15.22367	150.69800	-2.05155	1.41851	0.23571
16	-2.3552357020E+03	6543	1.50860	0.00764	0.00136	14.73578	149.34174	-0.00484	3.02017	3.93095

Table 4.6 Disk fitting results of 8 parameters. Note that the M_* is constrained by the disk scale heights in our models. Therefore, comparing the M_* with the observational central protostellar mass provides an idea of whether the disk is thiner than expected from hydrostatic equilibrium.

Power-law disk models									
Targets	p	β	M_{disk} [$M_\odot$]	R_{in} [AU]	R_{out} [AU]	θ_i [°]	PA [°]	M_* [$M_\odot$]	s
	1.15–3.35	-0.35–1.7	0.005–0.2	0.1–20	40–460	-83–83	0–180	0.2–5	
CI Tau	2.70±0.04	-0.03±0.01	0.0229±0.0005	11.5±0.6	237±15	56±2	12±2	0.3±0.1	1.45
DL Tau	1.93±0.02	0.47±0.01	0.0277±0.0002	5.0±0.5	130±2	-38.1±0.9	55±2	4.4±0.5	0.66
DO Tau	3.26±0.03	0.077±0.009	0.0338±0.0007	14.7±0.4	449±9	-26±2	56±5	0.21±0.01	2.00
FT Tau	1.7±0.3	-0.04±0.02	0.0149±0.0002	9±5	80±3	-54±1	172±1	3.2±0.9	0.43
Haro 6-13	3.22±0.04	0.13±0.04	0.033±0.004	0.9±0.9	429±23	-66±2	160±2	3.2±0.4	1.96
HL Tau	1.715±0.004	0.751±0.003	0.0958±0.0002	7.94±0.05	79.1±0.3	40.6±0.1	135.1±0.2	0.206±0.004	0.425

Viscous accretion disk models										
Targets	p	β	M_{disk} [$M_\odot$]	R_{in} [AU]	R_c [AU]	θ_i [°]	PA [°]	M_* [$M_\odot$]	γ	R_t [AU]
	0.00–3.35	-0.35–1.7	0.005–0.2	0.1–20	40–460	-83–83	0–180	0.2–5		
CI Tau	2.08±0.08	-0.03±0.01	0.0234±0.0008	6±2	166±9	-58±2	13±2	0.6±0.5	0.83	80
DL Tau	1.46±0.01	0.46±0.01	0.0294±0.0003	0.7±0.4	104±1	-38±1	56±2	4.4±0.5	0.19	51
DO Tau	3.25±0.05	0.07±0.01	0.036±0.002	14.5±0.2	220±73	-27±2	57±5	2.3±0.8	1.99	
FT Tau	0.6±0.2	-0.04±0.01	0.0152±0.0002	10±4	60±1	55±1	172±1	0.6±0.3	-0.69	32
Haro 6-13	3.23±0.06	0.13±0.04	0.033±0.006	1±1	114±16	67±2	160±2	1.5±0.5	1.98	
HL Tau	1.128±0.003	0.756±0.003	0.0976±0.0002	4.40±0.09	82.4±0.1	40.7±0.1	135.4±0.2	4.4±0.2	-0.162	41.9

Table 4.7 New age estimates and disk mass accretion properties. The ages are estimated using the web-based tool of Siess et al. (2000) and the T_{eff} and L_* of Beckwith et al. (1990). The M_{disk} values are of the accretion disk model estimate in Table 4.6 and the $\dot{M}_{disk}$ values come from Robitaille et al. (2007).

Targets	Age [10^6 years]	M_{disk} [$M_\odot$]	$\dot{M}_{disk}$ [$\times 10^{-7}$ $M_\odot$ year^{-1}]	$\dot{M}_{disk}/M_{disk}$ [$\times 10^{-6}$ year^{-1}]	α(10 AU)	α(100 AU)
CI Tau	1.41	0.0234	1.17	5.00	0.0613	0.0420
DL Tau	1.54	0.0294	1.17	3.98	0.1569	0.0213
DO Tau	1.14	0.036	6.76	18.7	–	–
FT Tau	–	0.0152	0.51	3.38	0.0786	0.0018
Haro 6-13	0.66	0.033	–	–	–	–
HL Tau	1.28	0.0976	10.2	10.5	0.4458	0.0256

Table 4.8 Correlation coefficients between properties and fit parameters of protostars and circumstellar disks. The Age_B indicates ages of Beckwith et al. (1990) and the Age_S is the new age estimate using the tool of Siess et al. (2000). The EW and n_{13} stand for EW(10 μm) and n_{13-31}, respectively, and their primes are the ones corrected by $\cos(\theta_i)$. R_{out} excludes DO Tau and Haro 6-13, which have the upper limit.

Power-law disk model											
Properties	Age_B	Age_S	EW	n_{13}	s	β	M_{disk}	R_{in}	R_{out}	M_*	
Age_B	1.00	0.95	-0.81	-0.99	**-0.83**	0.56	0.22	0.25	**-0.84**	0.04	
Age_S		1.00	-0.74	-0.92	-0.66	0.29	0.02	0.43	-0.72	-0.09	
EW			1.00	0.83	0.42	-0.47	0.04	-0.48	0.36	-0.04	
EW′	-0.79	-0.66	0.95	0.83	0.46	-0.71	-0.06	-0.18	0.37	-0.32	
n_{13}				1.00	0.83	-0.45	0.47	-0.23	**0.81**	-0.34	
n'_{13}	-0.95	**-0.83**	0.84	0.98	0.77	-0.63	0.32	-0.08	0.73	-0.46	
s					1.00	-0.50	-0.30	0.09	**0.98**	-0.25	
β						1.00	**0.84**	-0.30	-0.44	-0.03	
M_{disk}							1.00	-0.06	-0.26	-0.47	
R_{in}								1.00	0.05	-0.70	
R_{out}									1.00	-0.19	
M_*										1.00	

Accretion disk model											
Properties	Age_B	Age_S	EW	n_{13}	γ	β	M_{disk}	R_{in}	R_t	M_*	$\dot{M}/M$
Age_B	1.00	0.95	-0.81	-0.99	**-0.85**	0.55	0.23	-0.12	-0.26	0.66	-0.75
Age_S		1.00	-0.74	-0.92	-0.73	0.28	0.03	0.02	-0.03	0.40	**-0.96**
EW			1.00	0.83	0.34	-0.45	-0.04	-0.33	-0.17	-0.64	-0.34
EW′	0.61	0.54	-0.93	-0.56	-0.08	0.43	0.34	0.43	0.33	0.64	0.75
n_{13}				1.00	0.76	-0.44	0.42	0.00	0.30	-0.49	0.61
n'_{13}	-0.81	-0.68	0.95	0.84	0.34	-0.70	-0.11	-0.05	0.00	**-0.82**	-0.09
γ					1.00	-0.32	-0.15	0.14	0.77	-0.17	0.76
β						1.00	**0.85**	-0.47	-0.37	**0.92**	0.07
M_{disk}							1.00	-0.17	-0.19	0.67	0.36
R_{in}								1.00	0.53	-0.38	0.66
R_t									1.00	-0.16	0.69
M_*										1.00	0.19
$\dot{M}/M$											1.00

Table 4.9 Disk model comparison.

Targets	$\ln(P(D \mid H_P))$	$\ln(P(D \mid H_A))$	$\ln(K)$	Preferable model
CI Tau	-4393789.4	-4393785.0	-4.4	Comparable
DL Tau	-15379030.2	-15379099.6	69.4	Power-law
DO Tau	-5639430.5	-5639425.8	-4.7	Comparabe
FT Tau	-3979031.3	-3979036.6	5.3	Comparable
Haro 6-13	-2990863.3	-2990863.4	0.1	Comparable
HL Tau	-51568147.5	-51568102.9	-44.6	Accretion

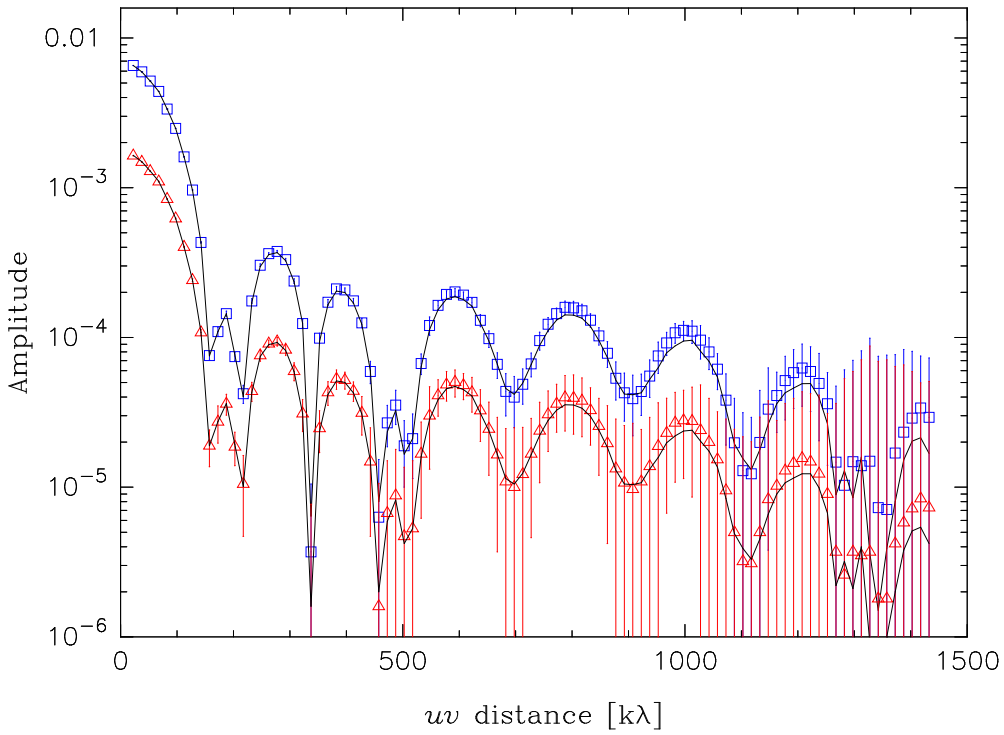

Figure 4.1 Visibility amplitudes along uv distance of the best fit models (in the ID 13 run) to the artificial disk data in $\sim 16 \times 6000$ proposals. Open square and triangles are artificial disk data at $\lambda = 1.3$ mm and 2.7 mm, respectively, and solid lines are the best fit models.

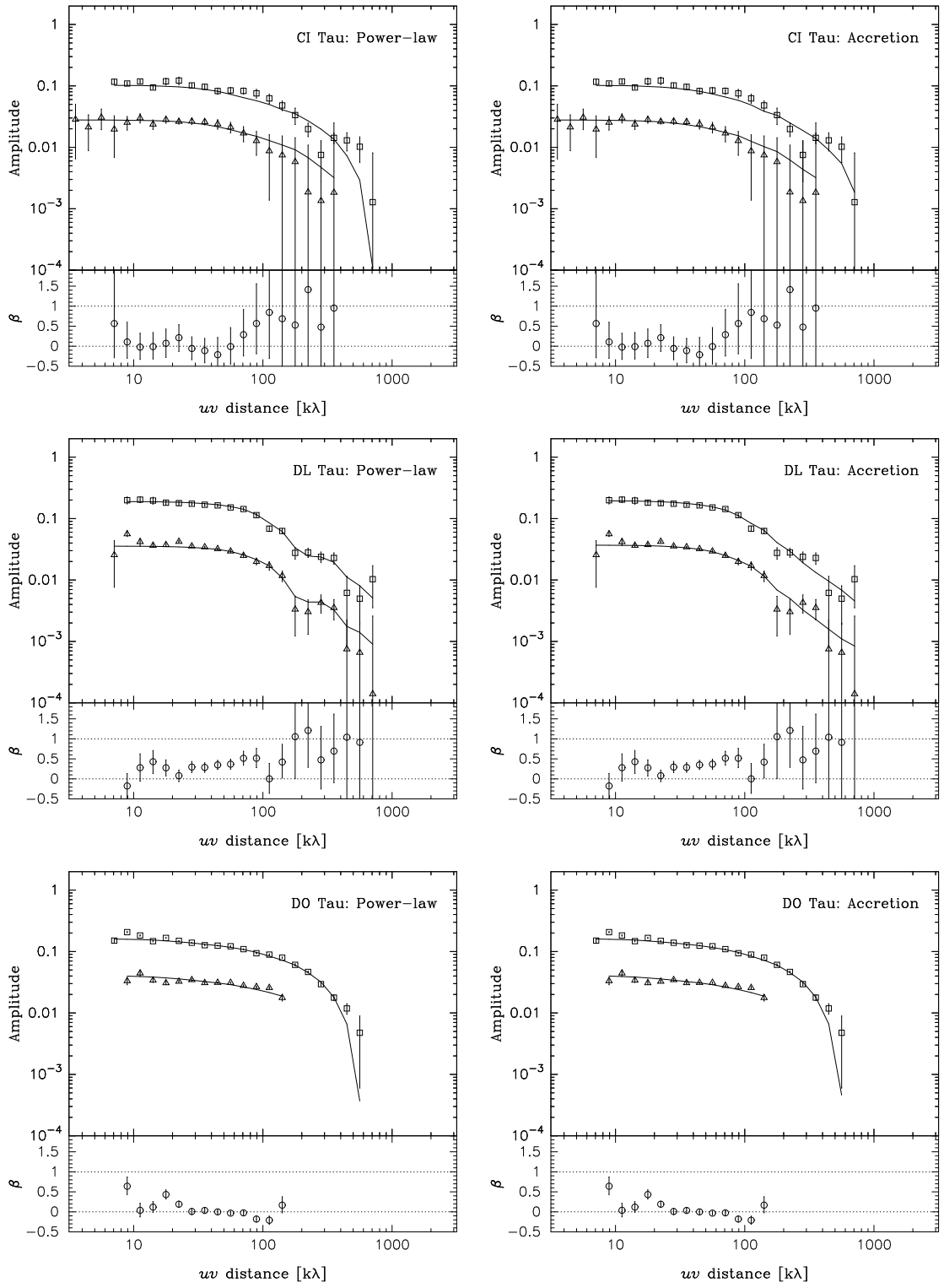

Figure 4.2 *uv* amplitude plots of CI Tau, DL Tau, and DO Tau with their best fitting models for the power-law disk and the accretion disk. β calculated from the observational data are also shown. Open squares are for $\lambda = 1.3$ mm data and open triangles for $\lambda = 2.7$ mm data.

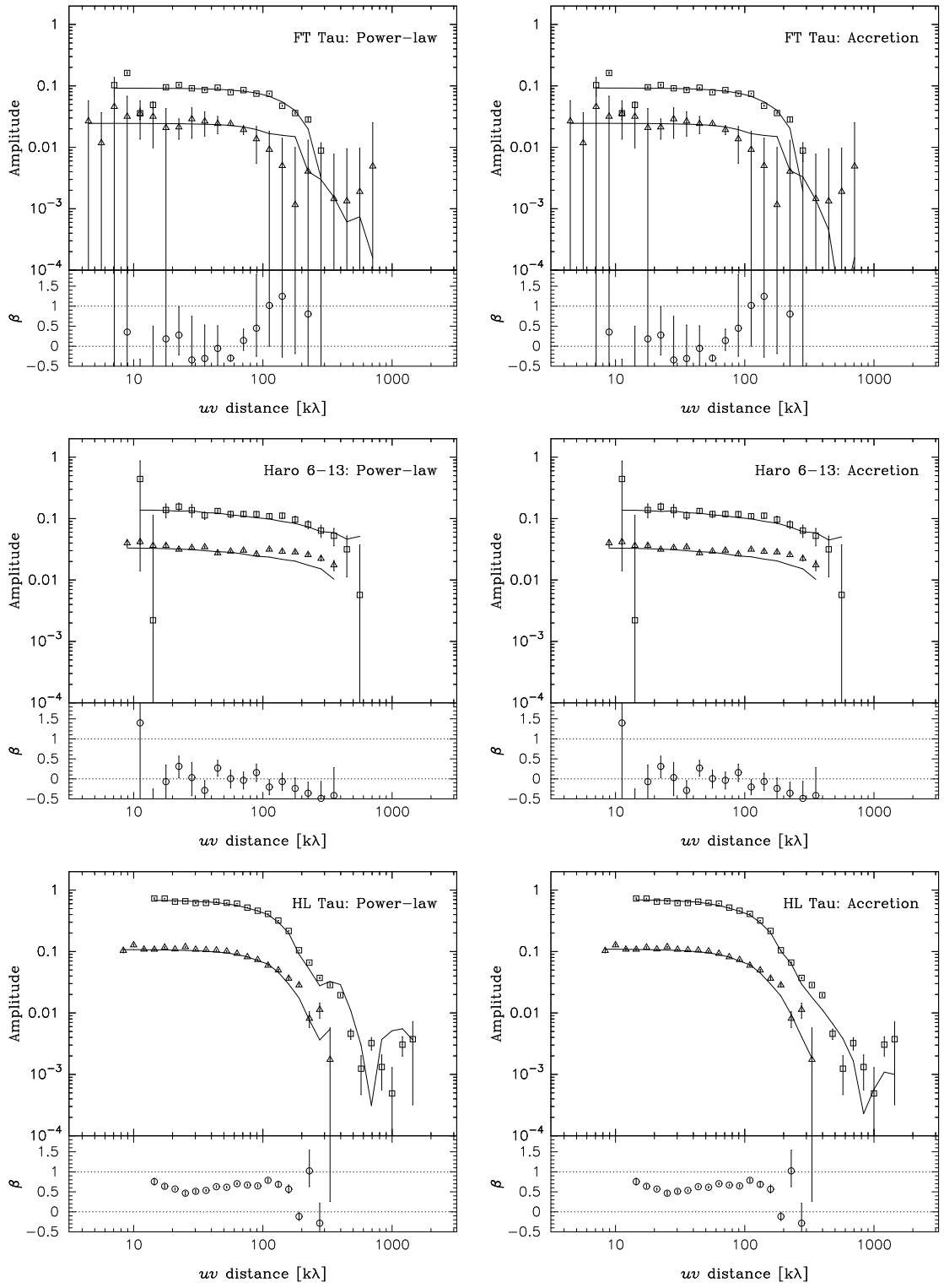

Figure 4.3 *uv* amplitude plots of FT Tau, Haro 6-13, and HL Tau with their best fitting models for the power-law disk and the accretion disk. β calculated from the observational data are also shown. Open squares are for $\lambda = 1.3$ mm data and open triangles for $\lambda = 2.7$ mm data.

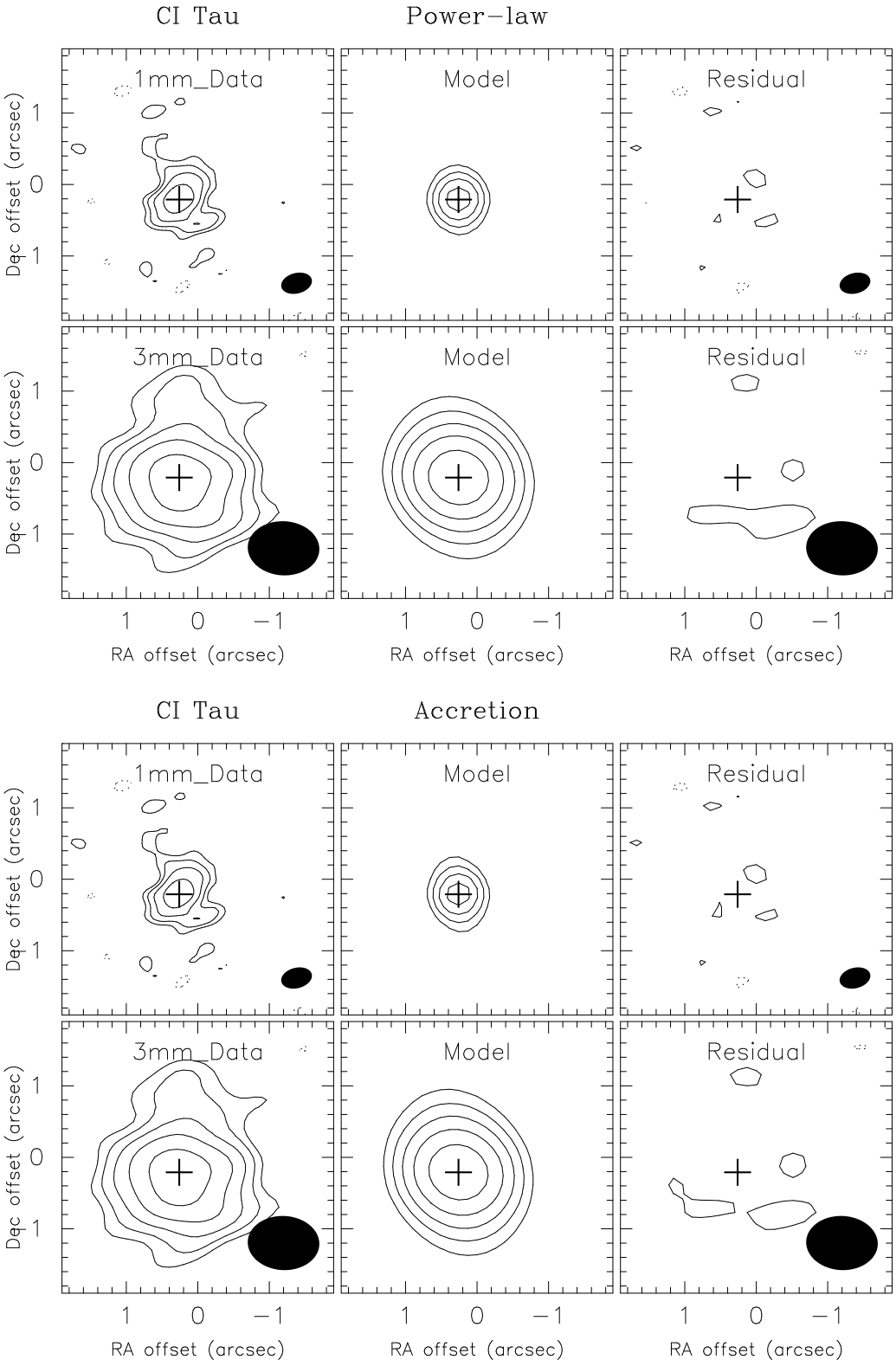

Figure 4.4 CI Tau continuum, model, and residual maps at $\lambda = 1.3$ mm and 2.7 mm for the power-law and the accretion disk models. The contour levels are 2.5, 4.0, 6.3, 10, and 16 times $\sigma = 2.0$ and 0.6 mJy beam^{-1} at $\lambda = 1.3$ mm and 2.7 mm, respectively.

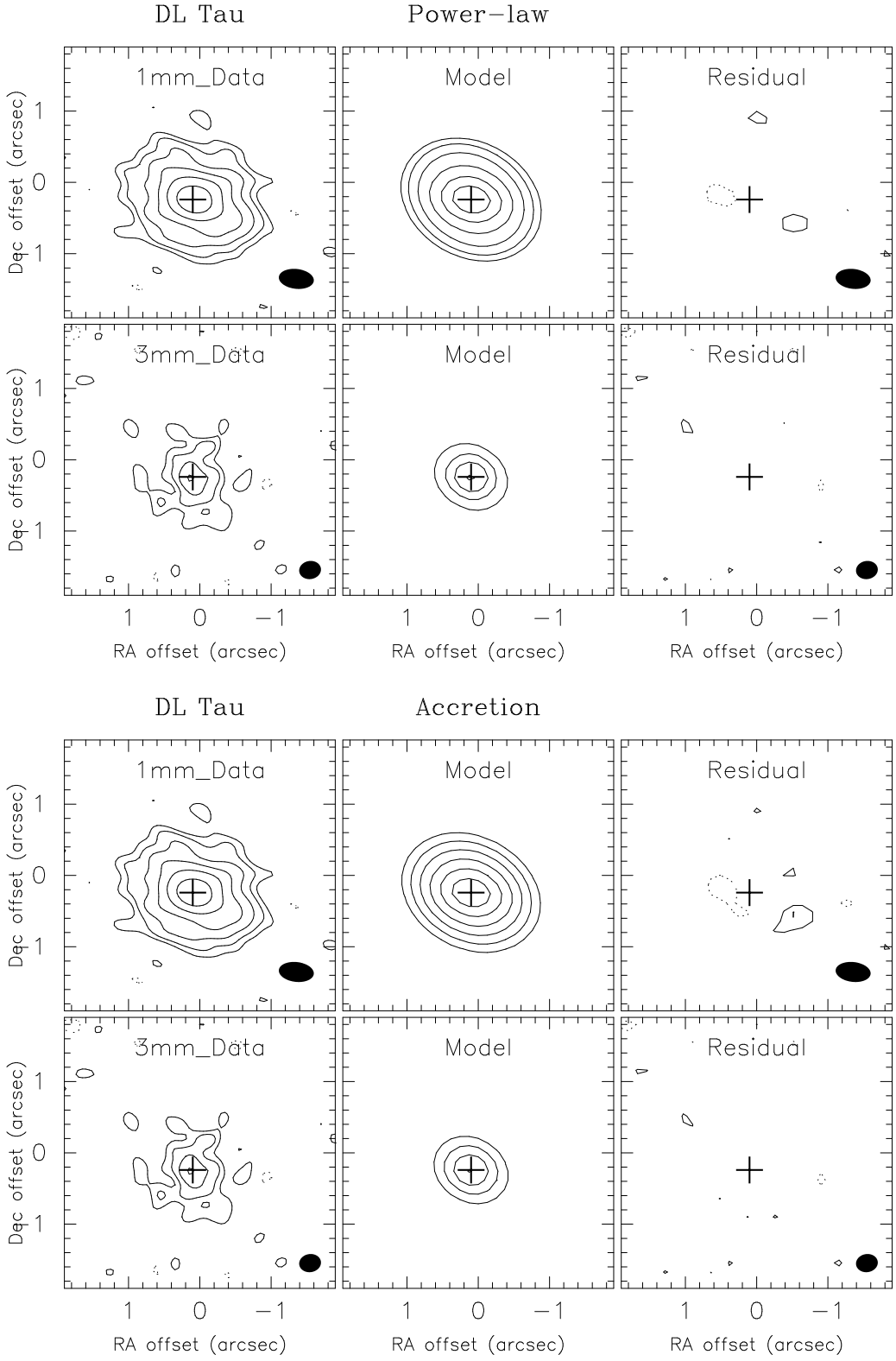

Figure 4.5 DL Tau continuum, model, and residual maps at $\lambda = 1.3$ mm and 2.7 mm for the power-law and the accretion disk models. The contour levels are 2.5, 4.0, 6.3, 10, 16, and 25 times $\sigma = 1.1$ and 0.5 mJy beam^{-1} at $\lambda = 1.3$ mm and 2.7 mm, respectively.

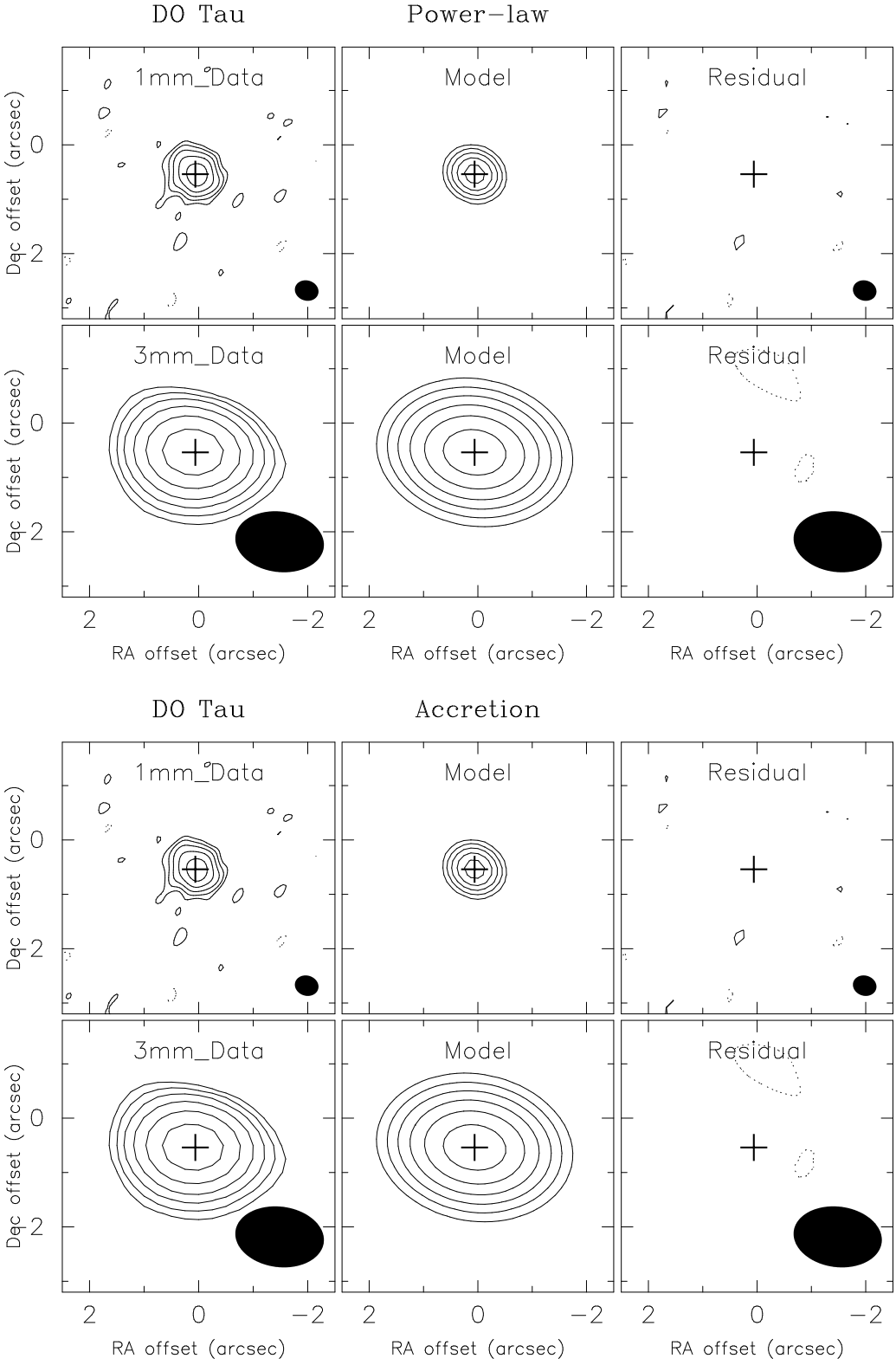

Figure 4.6 DO Tau continuum, model, and residual maps at $\lambda = 1.3$ mm and 2.7 mm for the power-law and the accretion disk models. The contour levels are 2.5, 4.0, 6.3, 10, 16, and 25 times $\sigma = 2.4$ and 0.8 mJy beam^{-1} at $\lambda = 1.3$ mm and 2.7 mm, respectively.

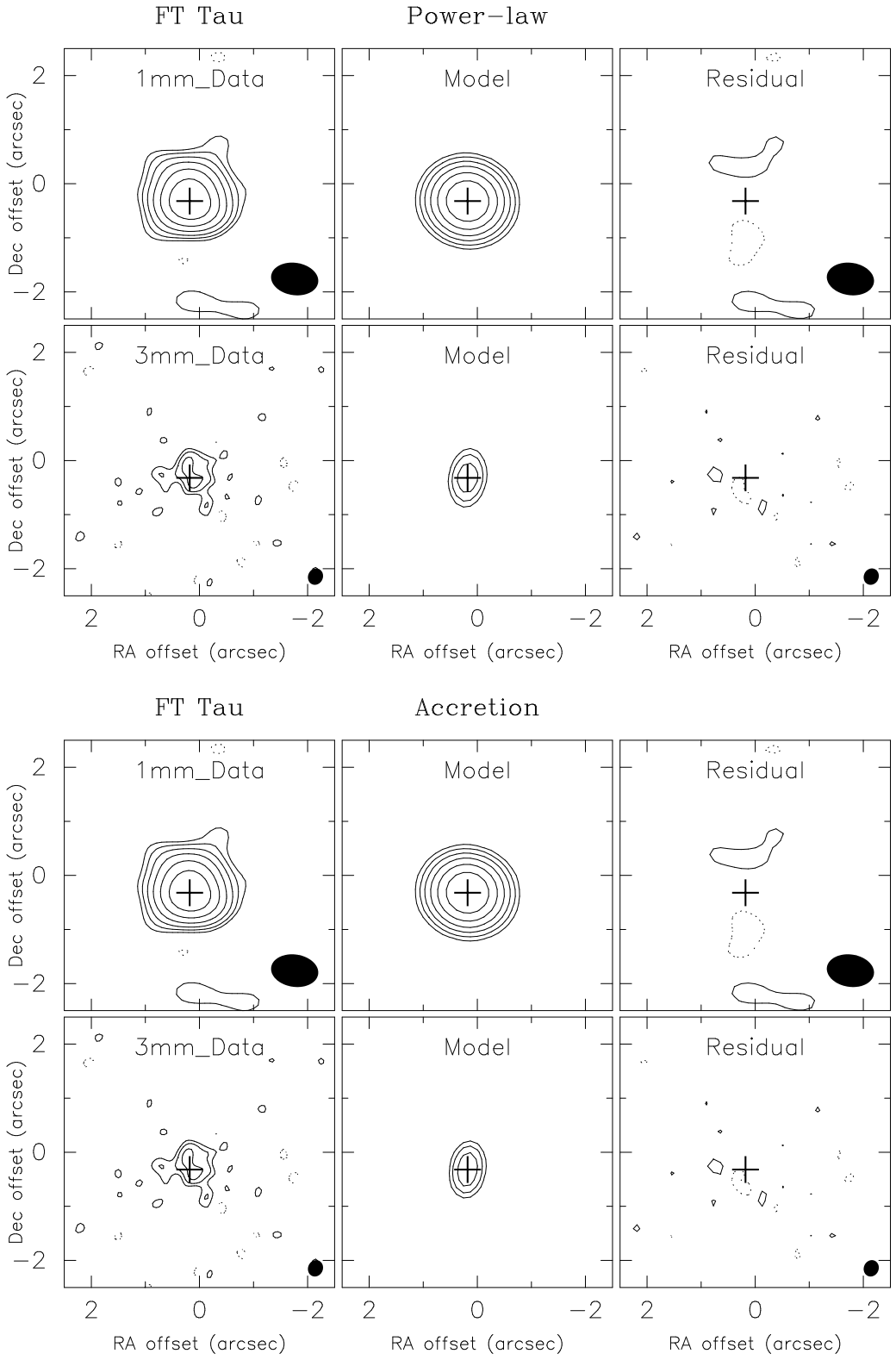

Figure 4.7 FT Tau continuum, model, and residual maps at $\lambda = 1.3$ mm and 2.7 mm for the power-law and the accretion disk models. The contour levels are 2.5, 4.0, 6.3, 10, 16, and 25 times $\sigma = 1.4$ and 0.6 mJy beam^{-1} at $\lambda = 1.3$ mm and 2.7 mm, respectively.

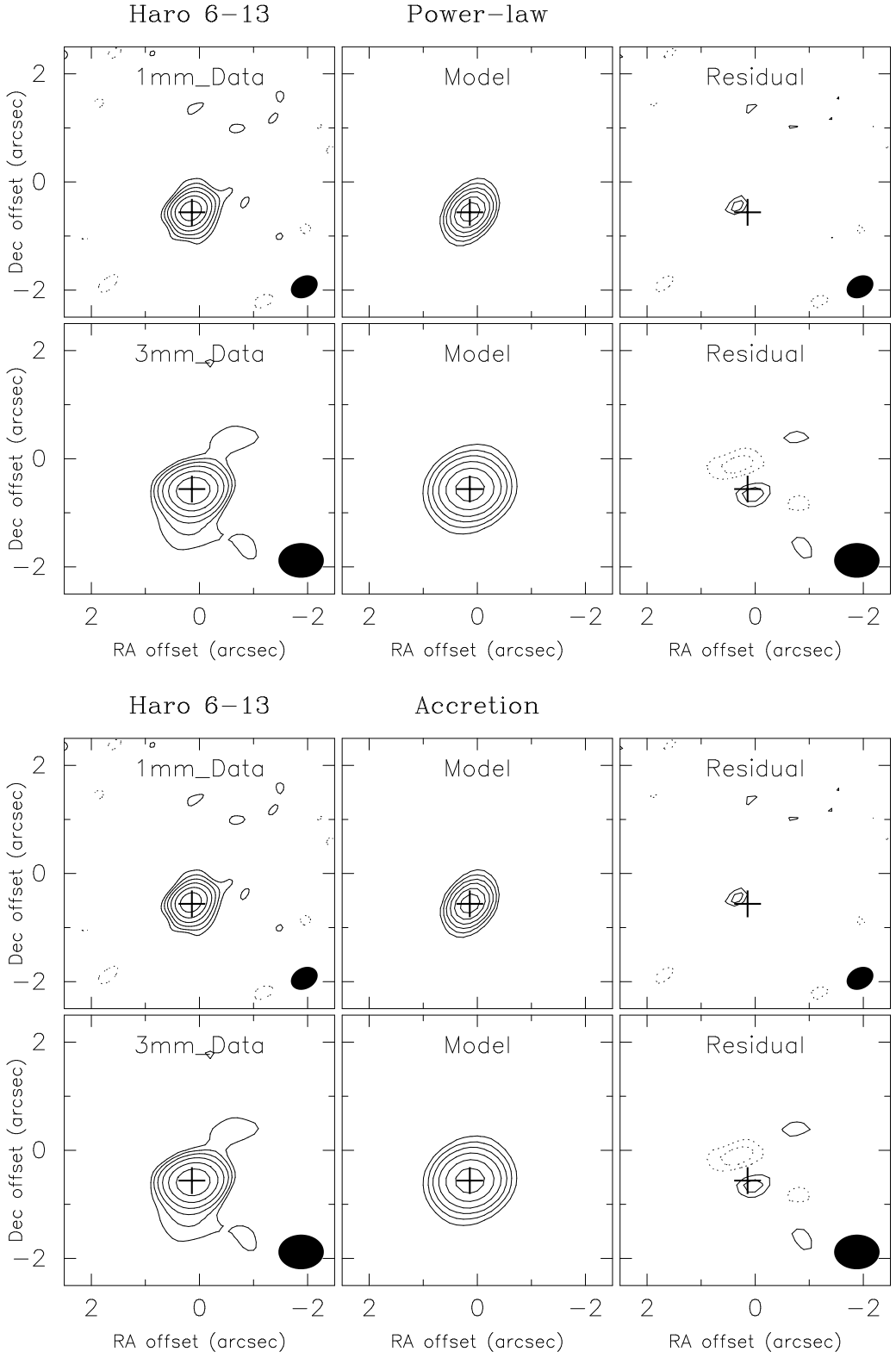

Figure 4.8 Haro 6-13 continuum, model, and residual maps at $\lambda = 1.3$ mm and 2.7 mm for the power-law and the accretion disk models. The contour levels are 2.5, 4.0, 6.3, 10, 16, and 25 times $\sigma = 2.3$ and 0.7 mJy beam^{-1} at $\lambda = 1.3$ mm and 2.7 mm, respectively.

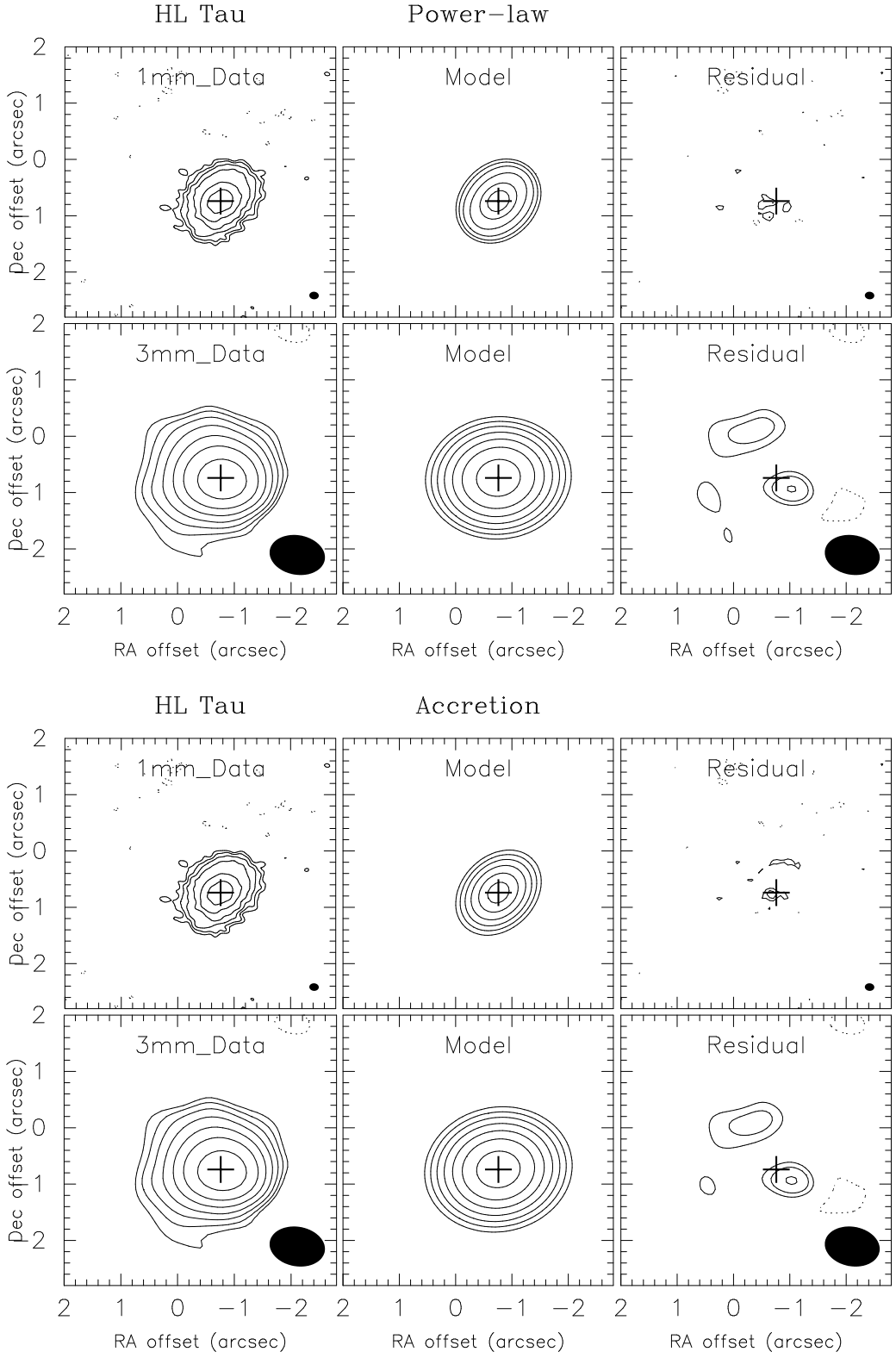

Figure 4.9 HL Tau continuum, model, and residual maps at $\lambda = 1.3$ mm and 2.7 mm for the power-law and the accretion disk models. The contour levels are 2.5, 4.0, 6.3, 10, 16, 25, and 40 times $\sigma = 0.9$ and 1.1 mJy beam^{-1} at $\lambda = 1.3$ mm and 2.7 mm, respectively.

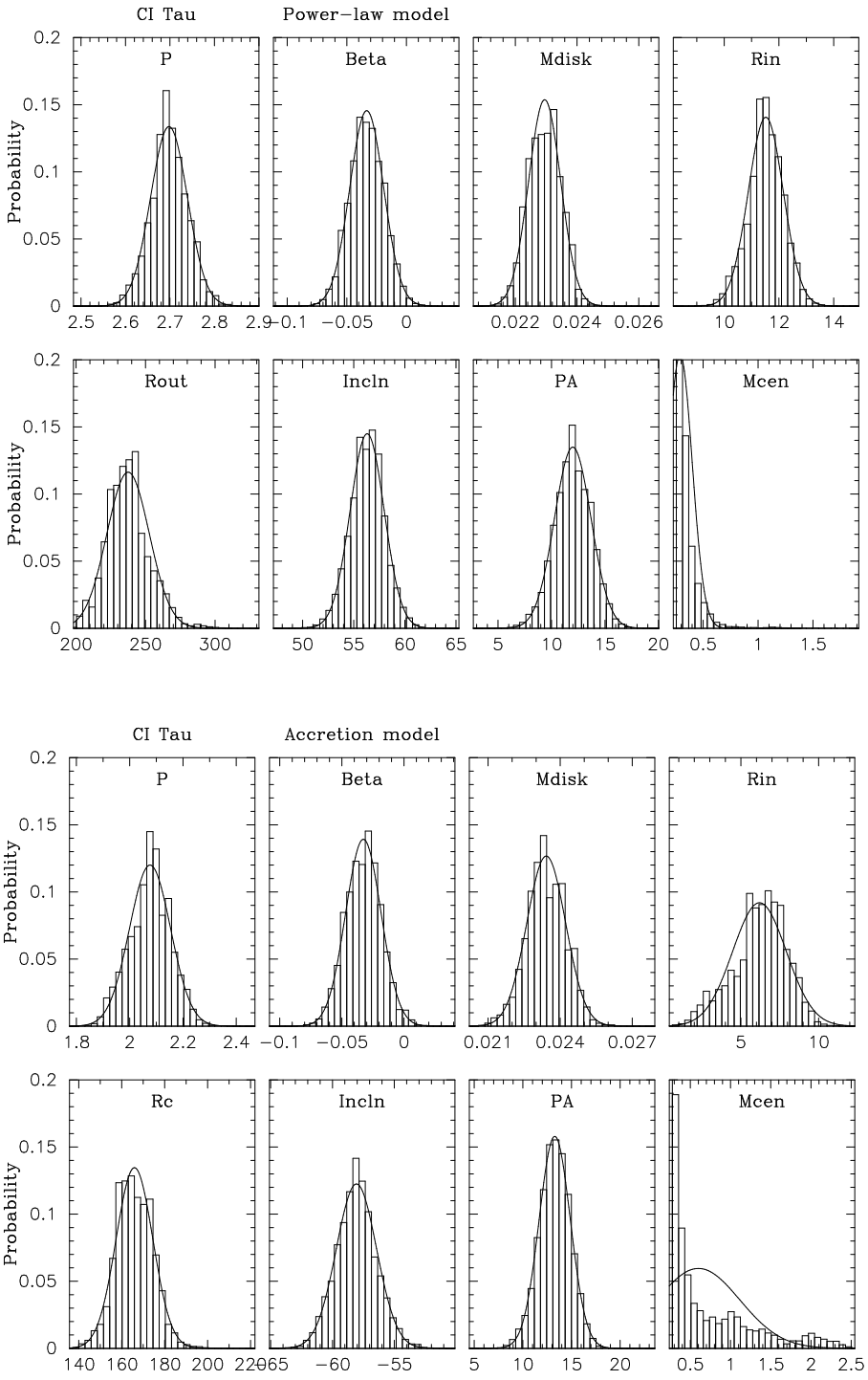

Figure 4.10 Posterior distribution of parameters in CI Tau.

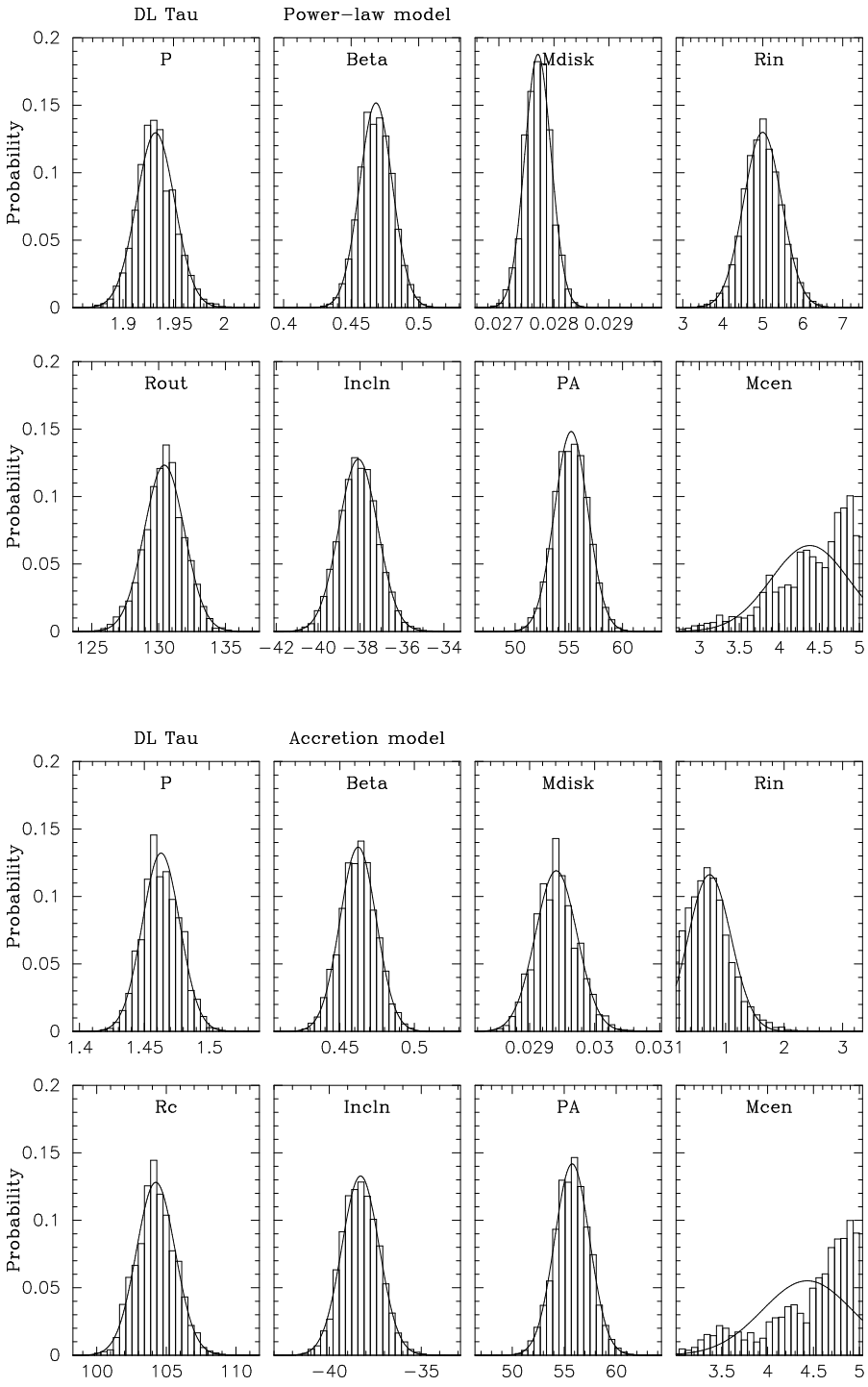

Figure 4.11 Posterior distribution of parameters in DL Tau.

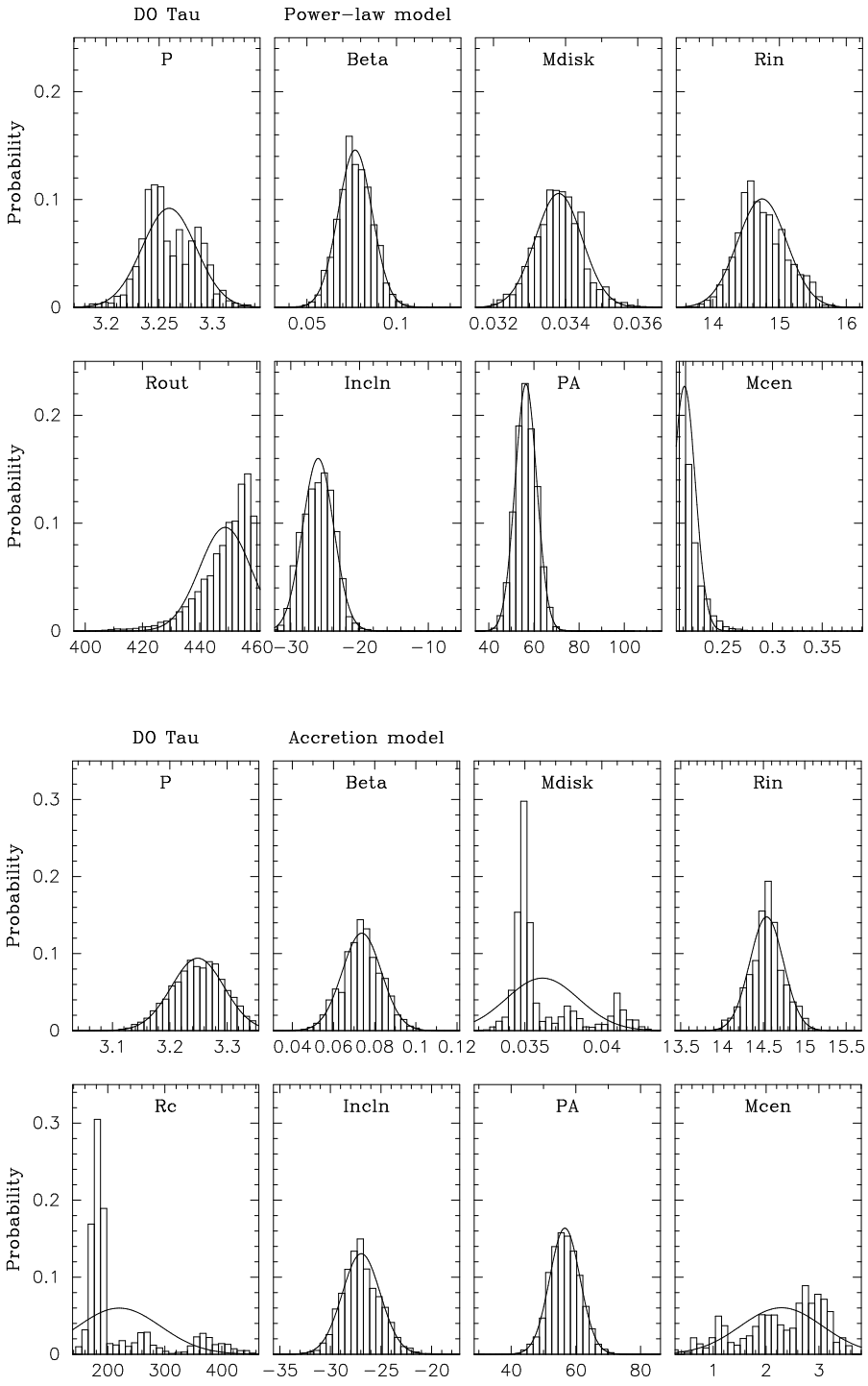

Figure 4.12 Posterior distribution of parameters in DO Tau.

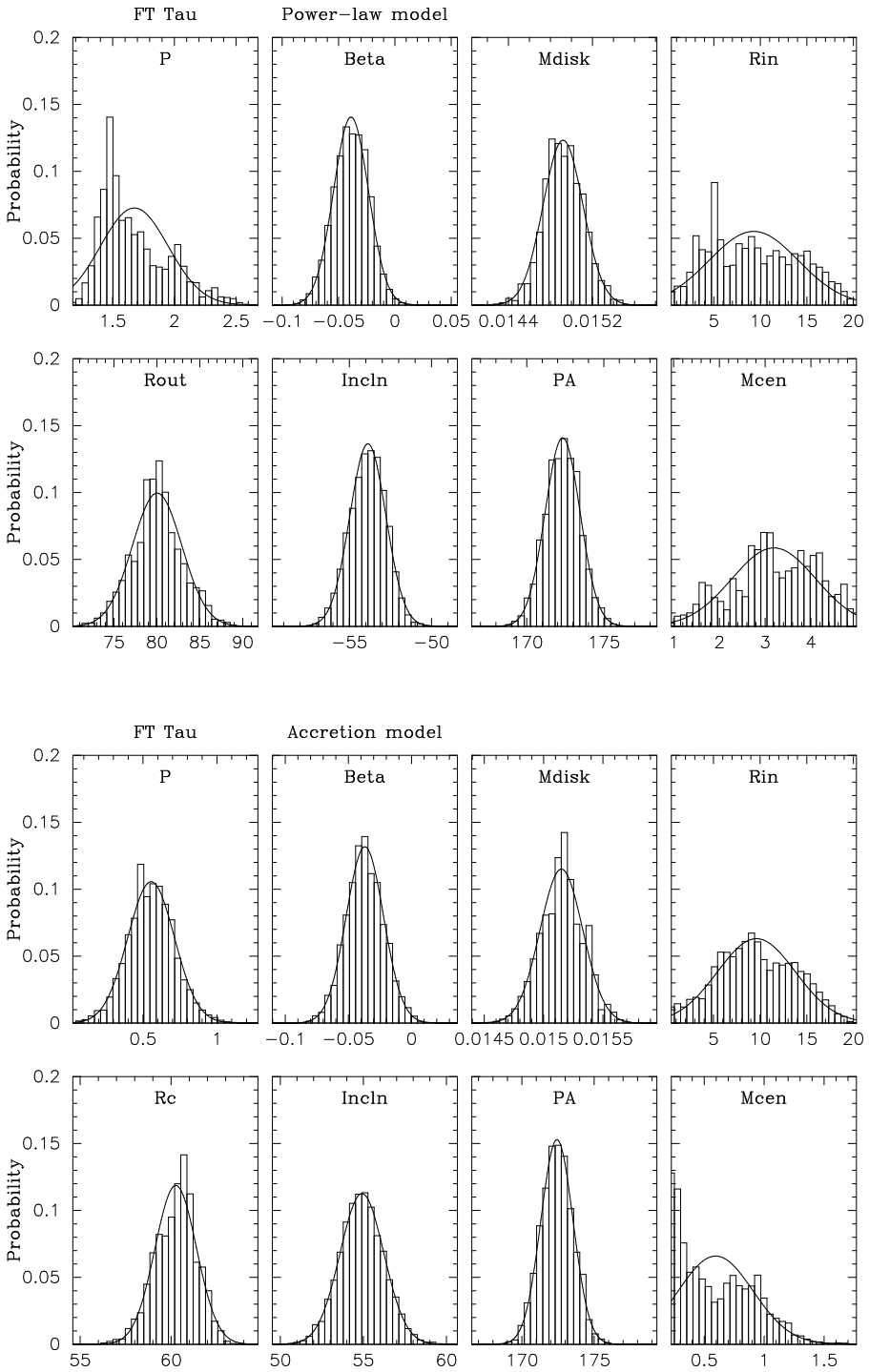

Figure 4.13 Posterior distribution of parameters in FT Tau.

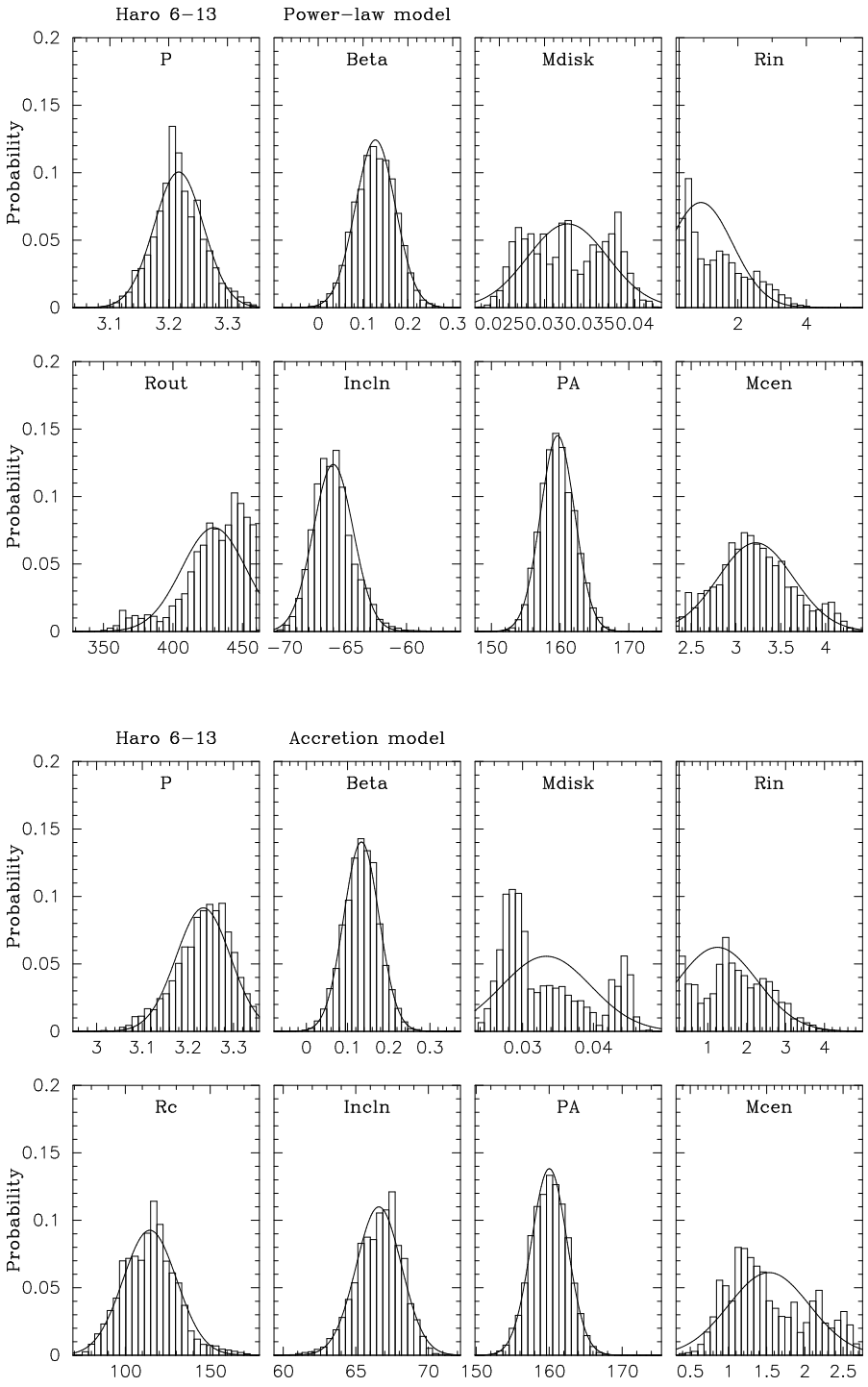

Figure 4.14 Posterior distribution of parameters in Haro 6-13.

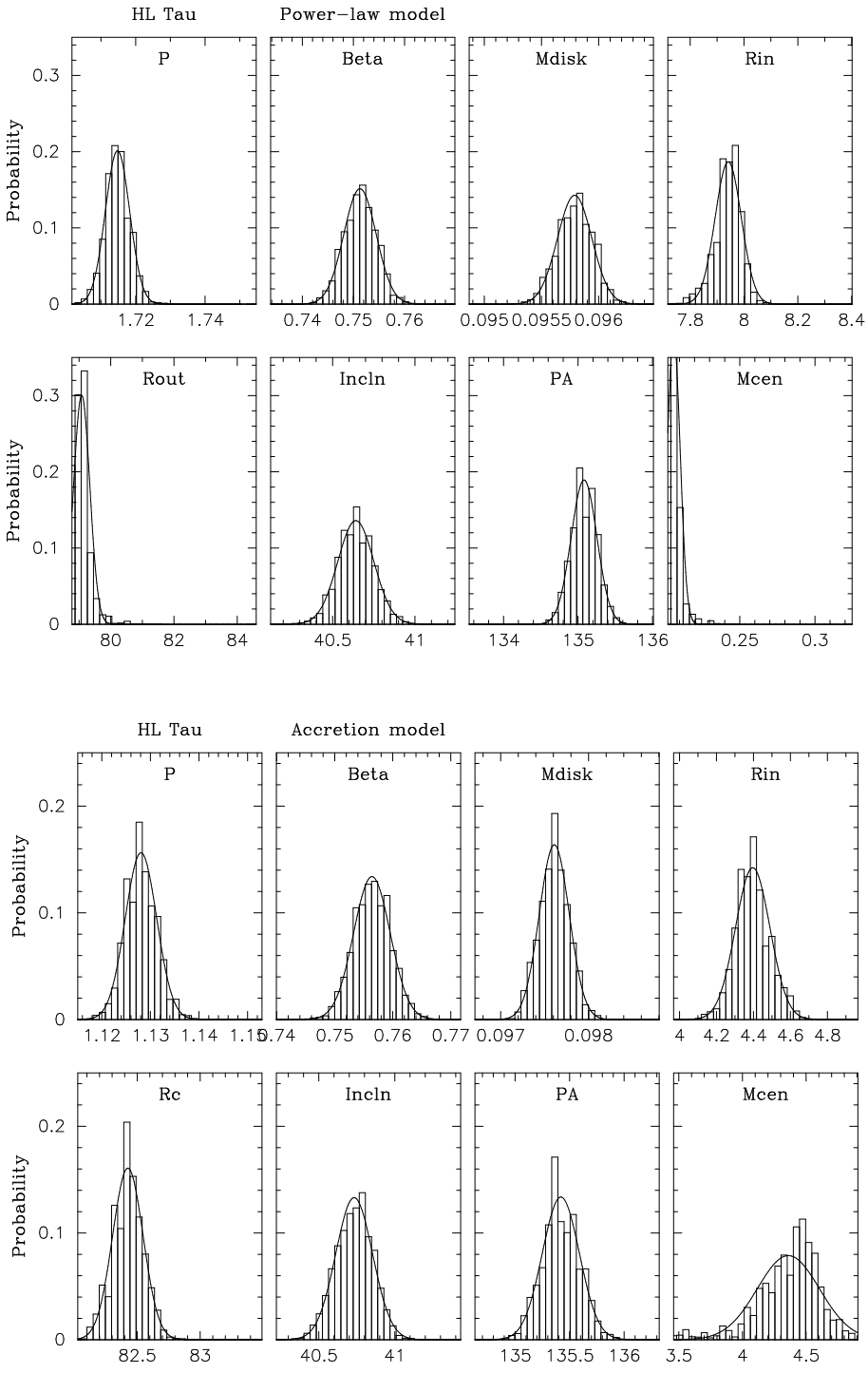

Figure 4.15 Posterior distribution of parameters in HL Tau.

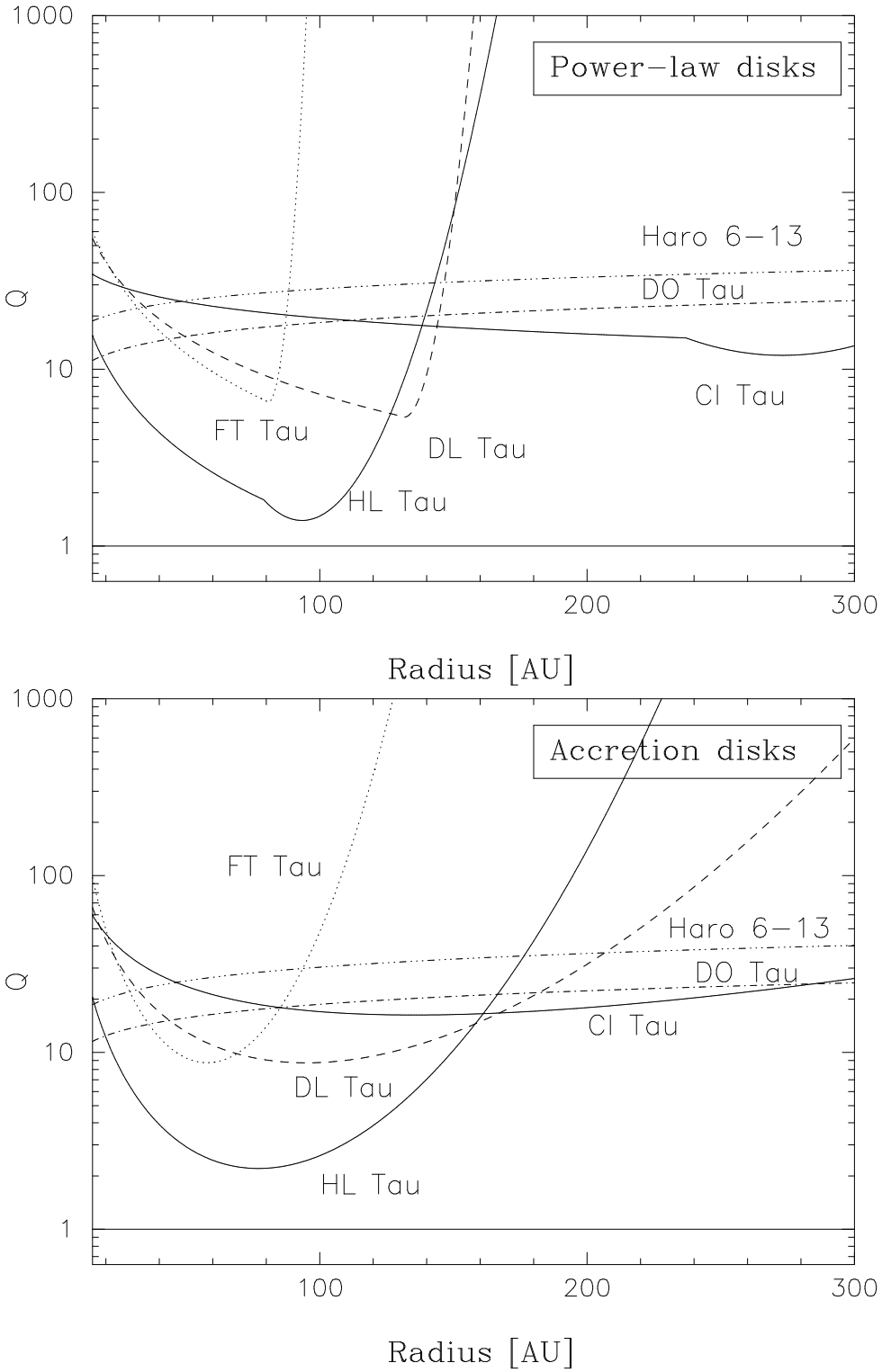

Figure 4.16 The Toomre Q parameter along radius in the power-law disk model and in the accretion disk model. The broken shapes in the power-law disk model are due to the Gaussian edges.

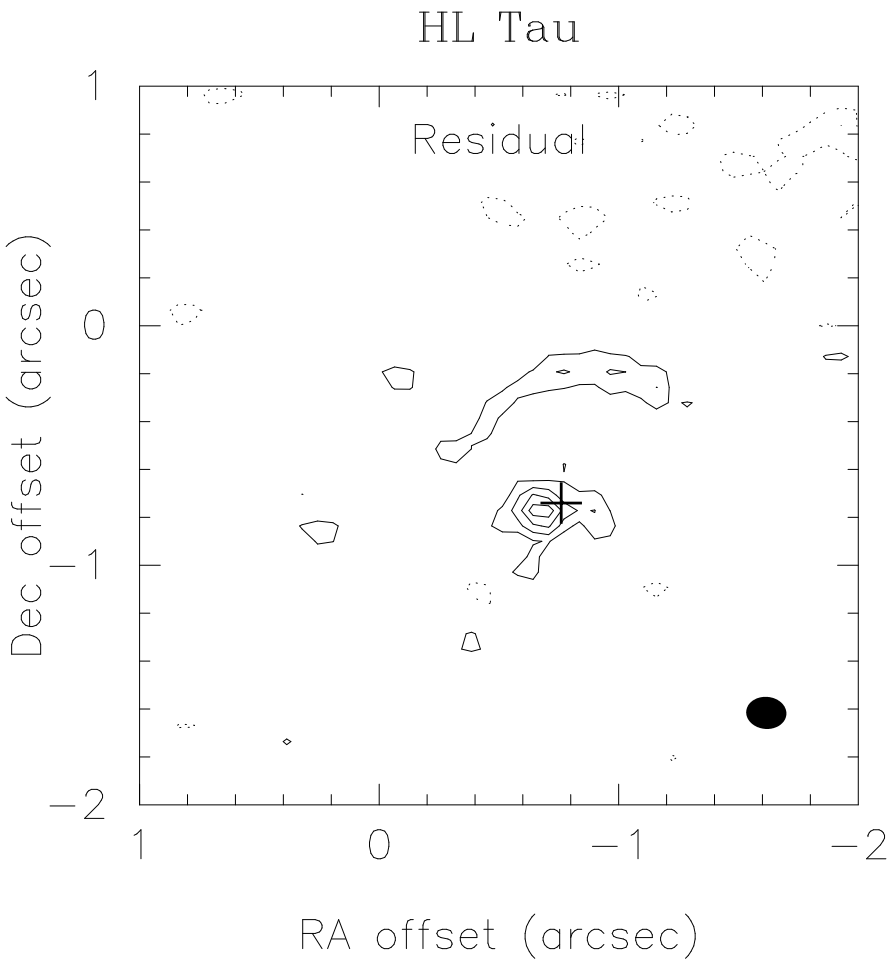

Figure 4.17 HL Tau residual map zoomed in at $\lambda = 1.3$ mm in the accretion disk model. The contour levels are 2, 3, 4, and 5 times $\sigma = 0.9$ mJy beam^{-1}.

5 Conclusion and Future Prospects

5.1 Summary and Conclusion

The three main structures of young stellar objects (YSOs) have been studied in this dissertation: envelopes, bipolar outflows, and circumstellar disks. The properties of these structures are the key to understand star and planet formation. For example, envelopes may keep the information of molecular cores as the initial conditions for star formation, while circumstellar disks provide the initial conditions for planet formation. In addition, bipolar outflows are at the center of YSOs interacting with their environments as a structure presumably generated by accretion and the most energetic phenomenon in YSO evolution.

To study envelope properties, three Class 0 YSOs (the youngest protostellar systems, L1448 IRS 2, L1448 IRS 3, and L1157) have been observed at $\lambda = 1.3$ mm and 2.7 mm continuum using CARMA, which provides the best image fidelity. Utilizing visibility modeling for two wavelengths simultaneously, we constrained the dust opacity spectral index β as well as the density power-law index p. First, we found that β of Class 0 YSOs is around unity, which implies that dust grains have significantly grown already at the earliest stage. This may lead to an earlier planetesimal formation. Second, there are two "groups" of YSOs with different density distribution. While L1448 IRS 2 and L1157 have $p \sim 1.8$ and 1.7, respectively, L1448 IRS 3B has $p \sim 2.6$. Based on the binarity and the less-extended bipolar outflow of L1448 IRS 3B, we suggested that "binary system" YSOs and/or younger YSOs in terms of the bipolar outflow time scale would have steeper density distributions. Third, a radial dependence of β has been detected in L1448 IRS 3B clearly. It was verified by models with β as a function of radius. In addition, we discussed that the grain growth causing the dependence can be achieved in a time scale of 10^4 years, corresponding to the kinematic time scale of bipolar outflows of Class 0 YSOs. On the other hand, we pointed out that dust segregation predicted by the ambipolar diffusion model of star formation could enhance the dependence. The density distribution of $p \sim 1.7$, which is detected in L1448 IRS 2 and L1157, is also predicted by the ambipolar diffusion model, although we did not attempt to constrain star formation models using the small number sample.

For understanding the binary system and the bipolar outflow of L14448 IRS 3, we have carried out polarimetric observations in $\lambda = 1.3$ mm continuum and CO $J = 2 \rightarrow 1$ and spectral line observations in ^{13}CO $J = 1 \rightarrow 0$ and C^{18}O $J = 1 \rightarrow 0$, using BIMA. Three

Class 0 YSOs are detected at $\lambda = 1.3$ mm in the region: L1448 IRS 3A, 3B, and 3C. First, based on the velocity difference along the line of sight between L1448 IRS 3A and 3B, we found that they can actually be a gravitationally bound binary system and we also estimated the specific angular momentum of the system as $\sim 3 \times 10^{20}$ cm^2 s^{-1}, similar to the upper limit of binary stars in Taurus and to the lower limit of molecular cloud cores. Second, we clearly identified two bipolar outflows, one from L1448 IRS 3A and the other from L1448 IRS 3B, and they appear to interact with each other where the redshifted lobe of the 3B bipolar outflow and the blueshifted lobe of the L1448 IRS 3A bipolar outflow are overlapped, based on their kinetic energy distribution. The linear polarization detected mainly in L1448 IRS 3B also supports the position enabling the interaction: L1448 IRS 3B closer to us. Third, we detected features implying that the L1448 IRS 3B bipolar outflow is precessing or has a "trumpet" shape. In addition, assuming the "trumpet" shape, we constrain the bipolar outflow properties such as the velocity, inclination angle, and opening angle, using Bayesian inference. Note that due to the spherical shape of envelopes obtaining the basic properties is not always straight forward but we could constrain the bipolar outflow properties successfully by Bayesian inference. Fourth, we marginally detected linear polarization in both $\lambda = 1.3$ mm continuum and CO $J = 2 \rightarrow 1$. The linear polarization in continuum is detected at the L1448 IRS 3B center and the direction implies a magnetic field perpendicular to the bipolar outflow, which may be a toroidal magnetic field component on the circumstellar disk. On the other hand, the spectral line polarization suggests either a perpendicular or a parallel magnetic fields to the bipolar outflow. More sensitive polarimetric observations are needed for better understanding about the relationship between magnetic fields and bipolar outflow generation.

To investigate the initial conditions of planet formation, we have initiated a T Tauri disk (Class II YSO) survey using CARMA. So far 6 target data have been "completed": CI Tau, DL Tau, DO Tau, FT Tau, Haro 6-13, and HL Tau. They consist of multi-configuration (A, B, C, and/or D array) and multi-wavelength data at $\lambda = 1.3$ mm and 2.7 mm, to cover a large range of scales and to better constrain the dust opacity spectral index (β). In addition to the quality data with a high angular resolution up to $0.13''$, we carried out visibility modeling of the power-law disk with a Gaussian edge and of the viscous accretion disk in Bayesian inference, in order to constrain their physical properties such as density distribution, dust opacity spectral index, disk mass, disk inner radius, disk outer radius (characteristic radius for the accretion disk model), inclination, position angle, and disk thickness (scale height factor). First, we found that HL Tau has a dust lane at about 100 AU, which is gravitationally unstable and where fragmentation is possible. On the other hand, CI Tau and DL Tau appear to have a spiral-like pattern in both wavelength maps and FT Tau shows a feature of a binary system or a single edge-on disk with a hole. Second, we found that the more evolved disks have the shallower density gradient along radius and

the less massive disks have a smaller β. The latter one may imply that non-detectable mass in the cold midplane and/or in large grains. In addition, the accretion rate per unit disk mass appears to decrease with protostellar age. Finally, we found that a disk model cannot explain all disks. While the power-law disk model with a Gaussian edge is preferred by DL Tau, which is the oldest in our sample and has a low mass accretion rate, the accretion disk model is preferred by HL Tau, which has a strong bipolar outflow and accretion. This implies that the accretion disk model can be applied to disks only in a very limited time scale and more evolved disks are better explained by the power-law disk model.

These results of the three main structures may be interpreted for a large picture of star and planet formation. For example, although grains appear to have significantly grown at the earliest stage of Class 0 already, they are even larger at Class II: β getting smaller or around 0 at T Tauri disks. Thus grains definitely keep growing between Class 0 and Class II. However, while β is about unity at Class 0 YSOs, it appears to distribute in a large range (0–0.75) at Class II YSOs. Although our samples are small (three YSOs in Class 0 and six in Class II), it may imply that there is a mechanism to significantly affect grain growth. Since we have detected a distinct radial dependence in one of our Class 0 YSOs and Class II disk size corresponds to the inner region experiencing more grain growth in the case, the mechanism can exist before the earliest Class 0 stage: e.g., grain segregation by magnetic fields. It is an example of exciting questions coming out through these studies. Probably a larger number of exciting questions have been raised than the number of interesting results.

5.2 Future Prospects

The topic of star and planet formation is one of the most active fields in astronomy today. Recently Spitzer Space Telescope opened a new window of near to far infrared wavelengths and Herschel for imaging and spectrographing at mid to far infrared (even up to submillimeter) wavelengths has been launched and started observations (commissioning phase) already. The infrared observations are essential to study the cold and dusty environment of star forming regions and they are also complimentary to radio observations.

At the same time, radio interferometers are expected to improve greatly. CARMA will have much broader bandwidth by more than a factor of two and polarimetric ability in a year. These improvements will allow us to carry out any survey observations very quickly. For example, a survey of many Class 0 YSOs is requested to obtain decisive results about the questions raised in this study: e.g., what caused the two groups of density distributions and which properties are relevant to the radial β dependence. In addition, the polarimetric observations of CARMA will provide the precious magnetic field information for the study. This magnetic field information is crucial to constrain star formation theories. On other hand, the Paired Antenna Calibration System of CARMA improves the quality

of data in the most extended A and B configurations. As shown, the quality data with high angular resolution will provide a direct method to study the structures of circumstellar disks. Moreover, in two years radio interferometry will face a new era with the Atacama Large Millimeter Array (ALMA).

The Bayesian inference, which has been used here, will keep providing the best way to understand the future high quality data. With the current knowledge as a prior, it can be applied for the future data quite easily. However, it is noteworthy that a better radiative transfer code is needed for a better data analysis with the Bayesian inference, in particular, to obtain a better temperature distribution.

Finally, the potential of astrochemistry should be noted; "Chemistry in space" sharpens our knowledge of physical properties as well. One of most difficult problems in star formation is to estimate the ages of YSOs at various stages. Utilizing some molecules with a well-defined time scale ("chemical clock") will be a unique means to determine ages. For some other instances, the ortho-to-para ratio of hydrogen molecules has been used to successfully reveal thermal history of shocked gas (e.g., Neufeld et al., 2006) and cosmic ionization rate has been reset by H_3^+ observations (McCall et al., 2003; Indriolo et al., 2007). In addition , ionization fraction of circumstellar disks, which can be estimated by observations of molecules and ions, will allow us to reveal the accretion mechanism of circumstellar disks. Most importantly, detection of water and "bio"-molecules and understanding of their formation particularly in star forming regions are another main pillar next to the one of star and planet formation to answer the ultimate question "Why are we here?" The observational facilities of today (Herschel and CARMA with 8 bands) and the near future (ALMA) will produce enormous data of chemistry in space.

References

Adams, F. C. 1991, ApJ, 382, 544

Adams, F. C., Lada, C. J., & Shu, F. H. 1987, ApJ, 312, 788

Andre, P. & Montmerle, T. 1994, ApJ, 420, 837

Andre, P., Ward-Thompson, D., & Barsony, M. 1993, ApJ, 406, 122

Andrews, S. M. & Williams, J. P. 2005, ApJ, 631, 1134

—. 2007, ApJ, 659, 705

Andrews, S. M., Wilner, D. J., Hughes, A. M., Qi, C., & Dullemond, C. P. 2009, ApJ, 700, 1502

Arce, H. G. & Sargent, A. I. 2006, ApJ, 646, 1070

Archibald, E. N., Dunlop, J. S., Jimenez, R., Friaça, A. C. S., McLure, R. J., & Hughes, D. H. 2002, MNRAS, 336, 353

Ayliffe, B. A. & Bate, M. R. 2009, MNRAS, 397, 657

Bachiller, R. & Cernicharo, J. 1986, A&A, 168, 262

Bachiller, R., Guilloteau, S., Dutrey, A., Planesas, P., & Martin-Pintado, J. 1995, A&A, 299, 857

Bachiller, R., Martin-Pintado, J., Tafalla, M., Cernicharo, J., & Lazareff, B. 1990, A&A, 231, 174

Bachiller, R., Pérez Gutiérrez, M., Kumar, M. S. N., & Tafalla, M. 2001, A&A, 372, 899

Balbus, S. A. 2003, ARA&A, 41, 555

Bally, J., Devine, D., Alten, V., & Sutherland, R. S. 1997, ApJ, 478, 603

Barsony, M., Ward-Thompson, D., André, P., & O'Linger, J. 1998, ApJ, 509, 733

Beckwith, S., Sargent, A. I., Scoville, N. Z., Masson, C. R., Zuckerman, B., & Phillips, T. G. 1986, ApJ, 309, 755

Beckwith, S. V. W. & Sargent, A. I. 1991, ApJ, 381, 250

Beckwith, S. V. W., Sargent, A. I., Chini, R. S., & Guesten, R. 1990, AJ, 99, 924

Beltrán, M. T., Gueth, F., Guilloteau, S., & Dutrey, A. 2004, A&A, 416, 631

Bergin, E. A. 2009, The Chemical Evolution of Protoplanetary Disks

Bertout, C., Robichon, N., & Arenou, F. 1999, A&A, 352, 574

Blum, J. 2000, Space Science Reviews, 92, 265

Bontemps, S., Andre, P., Terebey, S., & Cabrit, S. 1996, A&A, 311, 858

Briggs, D. S. 1995, PhD thesis, New Mexico Institute of Mining and Technology

Carrasco-González, C., Rodríguez, L. F., Anglada, G., & Curiel, S. 2009, ApJ, 693, L86

Chandler, C. J. & Richer, J. S. 2000, ApJ, 530, 851

Chandrasekhar, S. & Fermi, E. 1953, ApJ, 118, 113

Chiang, H.-F., Looney, L. W., Tassis, K., Mundy, L. G., & Mouschovias, T. C. 2008, ApJ, 680, 474

Chokshi, A., Tielens, A. G. G. M., & Hollenbach, D. 1993, ApJ, 407, 806

Ciardi, D. R., Telesco, C. M., Williams, J. P., Fisher, R. S., Packham, C., Piña, R., & Radomski, J. 2003, ApJ, 585, 392

Ciolek, G. E. & Mouschovias, T. C. 1996, ApJ, 468, 749

Crutcher, R. M. 1999, ApJ, 520, 706

Crutcher, R. M., Hakobian, N., & Troland, T. H. 2009, ApJ, 692, 844

Crutcher, R. M., Nutter, D. J., Ward-Thompson, D., & Kirk, J. M. 2004, ApJ, 600, 279

Curiel, S., Raymond, J. C., Moran, J. M., Rodriguez, L. F., & Canto, J. 1990, ApJ, 365, L85

Curiel, S., Torrelles, J. M., Rodríguez, L. F., Gómez, J. F., & Anglada, G. 1999, ApJ, 527, 310

Dartois, E., Dutrey, A., & Guilloteau, S. 2003, A&A, 399, 773

Davis, C. J. & Smith, M. D. 1995, ApJ, 443, L41

Draine, B. T. 1985, in Protostars and Planets II, ed. D. C. Black & M. S. Matthews, 621–640

Draine, B. T. 2006, ApJ, 636, 1114

Dutrey, A., Guilloteau, S., Duvert, G., Prato, L., Simon, M., Schuster, K., & Menard, F. 1996, A&A, 309, 493

Dutrey, A., Guilloteau, S., & Ho, P. 2007, in Protostars and Planets V, B. Reipurth, D. Jewitt, and K. Keil (eds.), University of Arizona Press, Tucson, 951 pp., 2007., p.495-506, ed. B. Reipurth, D. Jewitt, & K. Keil, 495–506

Dutrey, A., Guilloteau, S., Prato, L., Simon, M., Duvert, G., Schuster, K., & Menard, F. 1998, A&A, 338, L63

Dutrey, A., Guilloteau, S., & Simon, M. 1994, A&A, 286, 149

Dutrey, A., Henning, T., Guilloteau, S., Semenov, D., Pietu, V., Schreyer, K., Bacmann, A., Launhardt, R., Pety, J., & Gueth, F. 2006, Chemistry in disks I - Deep search for N2H+ in the protoplanetary disks around LkCa 15, MWC 480, and DM Tau

Eislöffel, J. 2000, A&A, 354, 236

Enoch, M. L., Young, K. E., Glenn, J., Evans, II, N. J., Golwala, S., Sargent, A. I., Harvey, P., Aguirre, J., Goldin, A., Haig, D., Huard, T. L., Lange, A., Laurent, G., Maloney, P., Mauskopf, P., Rossinot, P., & Sayers, J. 2006, ApJ, 638, 293

Fiedler, R. A. & Mouschovias, T. C. 1993, ApJ, 415, 680

Finkbeiner, D. P., Davis, M., & Schlegel, D. J. 1999, ApJ, 524, 867

Flower, D. R., Pineau Des Forêts, G., & Walmsley, C. M. 2005, A&A, 436, 933

Furlan, E., Watson, D. M., McClure, M. K., Manoj, P., Espaillat, C., D'Alessio, P., Calvet, N., Kim, K. H., Sargent, B. A., Forrest, W. J., & Hartmann, L. 2009, ApJ, 703, 1964

Gammie, C. F. 1996, ApJ, 457, 355

Gilks, W. R., Richardson, S., & Spiegelharlter, D. J. 1996, Markov Chain Monte Carlo in Practice (Chapman and Hall)

Girart, J. M. & Acord, J. M. P. 2001, ApJ, 552, L63

Girart, J. M., Crutcher, R. M., & Rao, R. 1999, ApJ, 525, L109

Girart, J. M., Rao, R., & Marrone, D. P. 2006, Science, 313, 812

Goodman, A. A., Benson, P. J., Fuller, G. A., & Myers, P. C. 1993, ApJ, 406, 528

Greaves, J. S., Holland, W. S., Jenness, T., Chrysostomou, A., Berry, D. S., Murray, A. G., Tamura, M., Robson, E. I., Ade, P. A. R., Nartallo, R., Stevens, J. A., Momose, M., Morino, J.-I., Moriarty-Schieven, G., Gannaway, F., & Haynes, C. V. 2003, MNRAS, 340, 353

Greaves, J. S., Richards, A. M. S., Rice, W. K. M., & Muxlow, T. W. B. 2008, MNRAS, 391, L74

Gueth, F., Bachiller, R., & Tafalla, M. 2003, A&A, 401, L5

Guilloteau, S. & Dutrey, A. 1994, A&A, 291, L23

—. 1998, A&A, 339, 467

Hartmann, L. 2001, Accretion Processes in Star Formation, ed. L. Hartmann

Hartmann, L., Ballesteros-Paredes, J., & Bergin, E. A. 2001, ApJ, 562, 852

Hartmann, L., Calvet, N., Gullbring, E., & D'Alessio, P. 1998, ApJ, 495, 385

Harvey, D. W. A., Wilner, D. J., Myers, P. C., Tafalla, M., & Mardones, D. 2003, ApJ, 583, 809

Hatchell, J., Richer, J. S., Fuller, G. A., Qualtrough, C. J., Ladd, E. F., & Chandler, C. J. 2005, A&A, 440, 151

Hayashi, C. 1981, Progress of Theoretical Physics Supplement, 70, 35

Hildebrand, R. H. 1983, QJRAS, 24, 267

Hogerheijde, M. R. & Sandell, G. 2000, ApJ, 534, 880

Holland, W. S., Robson, E. I., Gear, W. K., Cunningham, C. R., Lightfoot, J. F., Jenness, T., Ivison, R. J., Stevens, J. A., Ade, P. A. R., Griffin, M. J., Duncan, W. D., Murphy, J. A., & Naylor, D. A. 1999, MNRAS, 303, 659

Hughes, A. M., Wilner, D. J., Qi, C., & Hogerheijde, M. R. 2008, ApJ, 678, 1119

Indriolo, N., Geballe, T. R., Oka, T., & McCall, B. J. 2007, ApJ, 671, 1736

Isella, A., Carpenter, J. M., & Sargent, A. I. 2009, ApJ, 701, 260

Kenyon, S. J., Dobrzycka, D., & Hartmann, L. 1994, AJ, 108, 1872

Kenyon, S. J. & Hartmann, L. 1995, ApJS, 101, 117

Kim, K.-T. & Kurtz, S. E. 2006, ApJ, 643, 978

Kitamura, Y., Momose, M., Yokogawa, S., Kawabe, R., Tamura, M., & Ida, S. 2002, ApJ, 581, 357

Koerner, D. W. & Sargent, A. I. 1995, AJ, 109, 2138

Kwon, W., Looney, L. W., Crutcher, R. M., & Kirk, J. M. 2006, ApJ, 653, 1358

Kwon, W., Looney, L. W., Mundy, L. G., Chiang, H., & Kemball, A. J. 2009, ApJ, 696, 841

Kylafis, N. D. 1983, ApJ, 275, 135

Lada, C. J. 1985, ARA&A, 23, 267

Lada, C. J. & Wilking, B. A. 1984, ApJ, 287, 610

Lamb, J., Woody, D., Bock, D., Bolatto, A., Teuben, P., Zauderer, A., Leitch, E., Peréz, L., Plambeck, R., & Wright, M. 2009, in SPIE Newsroom

Lay, O. P., Carlstrom, J. E., & Hills, R. E. 1997, ApJ, 489, 917

Li, A. & Draine, B. T. 2001, ApJ, 554, 778

Looney, L. W., Mundy, L. G., & Welch, W. J. 2000, ApJ, 529, 477

—. 2003, ApJ, 592, 255

Looney, L. W., Tobin, J. J., & Kwon, W. 2007, ApJ, 670, L131

MacKay, D. J. C. 2003, Information Theory, Inference, and Learning Algorithms (Cambridge, UK: Cambridge University Press)

Mathis, J. S., Rumpl, W., & Nordsieck, K. H. 1977, ApJ, 217, 425

McCall, B. J., Huneycutt, A. J., Saykally, R. J., Geballe, T. R., Djuric, N., Dunn, G. H., Semaniak, J., Novotny, O., Al-Khalili, A., Ehlerding, A., Hellberg, F., Kalhori, S., Neau, A., Thomas, R., Österdahl, F., & Larsson, M. 2003, Nature, 422, 500

McCuskey, S. W. 1938, ApJ, 88, 209

McKee, C. F. & Ostriker, E. C. 2007, ARA&A, 45, 565

Mouschovias, T. C. 1991, ApJ, 373, 169

Mundt, R., Buehrke, T., Solf, J., Ray, T. P., & Raga, A. C. 1990, A&A, 232, 37

Mundy, L. G., Looney, L. W., Erickson, W., Grossman, A., Welch, W. J., Forster, J. R., Wright, M. C. H., Plambeck, R. L., Lugten, J., & Thornton, D. D. 1996, ApJ, 464, L169+

Natta, A., Testi, L., Calvet, N., Henning, T., Waters, R., & Wilner, D. 2007, in Protostars and Planets V, ed. B. Reipurth, D. Jewitt, & K. Keil, 767–781

Nero, D. & Bjorkman, J. E. 2009, ApJ, 702, L163

Neufeld, D. A., Melnick, G. J., Sonnentrucker, P., Bergin, E. A., Green, J. D., Kim, K. H., Watson, D. M., Forrest, W. J., & Pipher, J. L. 2006, ApJ, 649, 816

O'Linger, J., Wolf-Chase, G., Barsony, M., & Ward-Thompson, D. 1999, ApJ, 515, 696

Ossenkopf, V. & Henning, T. 1994, A&A, 291, 943

Ostriker, E. C. 1997, ApJ, 486, 291

Piétu, V., Guilloteau, S., & Dutrey, A. 2005, A&A, 443, 945

Pollack, J. B., Hollenbach, D., Beckwith, S., Simonelli, D. P., Roush, T., & Fong, W. 1994, ApJ, 421, 615

Poppe, T., Blum, J., & Henning, T. 2000, ApJ, 533, 454

Preibisch, T. & Smith, M. D. 1997, A&A, 322, 825

Press, W. H., Teukolsky, S. A., Vetterling, W. T., & Flannery, B. F. 1996, Numerical Recipes in Fortran 77 (2nd ed. New York : the Press Syndicate of the University of Cambridge. ISBN : 052143064X)

Pringle, J. E. 1981, ARA&A, 19, 137

Qi, C., Ho, P. T. P., Wilner, D. J., Takakuwa, S., Hirano, N., Ohashi, N., Bourke, T. L., Zhang, Q., Blake, G. A., Hogerheijde, M., Saito, M., Choi, M., & Yang, J. 2004, ApJ, 616, L11

Qi, C., Kessler, J. E., Koerner, D. W., Sargent, A. I., & Blake, G. A. 2003, ApJ, 597, 986

Qi, C., Wilner, D. J., Calvet, N., Bourke, T. L., Blake, G. A., Hogerheijde, M. R., Ho, P. T. P., & Bergin, E. 2006, ApJ, 636, L157

Rao, R., Crutcher, R. M., Plambeck, R. L., & Wright, M. C. H. 1998, ApJ, 502, L75

Rao, R. P. 1999, Ph.D. Thesis

Rebull, L. M., Wolff, S. C., & Strom, S. E. 2004, AJ, 127, 1029

Reynolds, S. P. 1986, ApJ, 304, 713

Robitaille, T. P., Whitney, B. A., Indebetouw, R., & Wood, K. 2007, ApJS, 169, 328

Rohlfs, K. & Wilson, T. L. 2004, Tools of Radio Astronomy, 4th Edition (Springer, 2004, ISBN : 3540403876)

Sault, R. J., Teuben, P. J., & Wright, M. C. H. 1995, in Astronomical Society of the Pacific Conference Series, Vol. 77, Astronomical Data Analysis Software and Systems IV, ed. R. A. Shaw, H. E. Payne, & J. J. E. Hayes, 433–+

Schaefer, G. H., Dutrey, A., Guilloteau, S., Simon, M., & White, R. J. 2009, ApJ, 701, 698

Seale, J. P. & Looney, L. W. 2008, ApJ, 675, 427

Shakura, N. I. & Sunyaev, R. A. 1973, A&A, 24, 337

Shirley, Y. L., Evans, II, N. J., Rawlings, J. M. C., & Gregersen, E. M. 2000, ApJS, 131, 249

Shu, F. H. 1977, ApJ, 214, 488

Siess, L., Dufour, E., & Forestini, M. 2000, A&A, 358, 593

Simon, M., Dutrey, A., & Guilloteau, S. 2000, ApJ, 545, 1034

Simon, M., Ghez, A. M., Leinert, C., Cassar, L., Chen, W. P., Howell, R. R., Jameson, R. F., Matthews, K., Neugebauer, G., & Richichi, A. 1995, ApJ, 443, 625

Smith, K. W., Lewis, G. F., Bonnell, I. A., Bunclark, P. S., & Emerson, J. P. 1999, MNRAS, 304, 367

Spitzer, L. 1978, Physical processes in the interstellar medium (New York Wiley-Interscience, 1978. 333 p.)

Sutton, E. C. & Wandelt, B. D. 2006, ApJS, 162, 401

Tassis, K. & Mouschovias, T. C. 2005, ApJ, 618, 783

Taylor, G. B., Carilli, C. L., & Perley, R. A., eds. 1999, Astronomical Society of the Pacific Conference Series, Vol. 180, Synthesis Imaging in Radio Astronomy II

Terebey, S. & Padgett, D. L. 1997, in IAU Symp. 182: Herbig-Haro Flows and the Birth of Stars, 507–514

Thompson, A. R., Moran, J. M., & Swenson, Jr., G. W. 2001, Interferometry and Synthesis in Radio Astronomy, 2nd Edition (Interferometry and synthesis in radio astronomy by A. Richard Thompson, James M. Moran, and George W. Swenson, Jr. 2nd ed. New York : Wiley, c2001.xxiii, 692 p. : ill. ; 25 cm. "A Wiley-Interscience publication." Includes bibliographical references and indexes. ISBN : 0471254924)

Tobin, J. J., Looney, L. W., Mundy, L. G., Kwon, W., & Hamidouche, M. 2007, ApJ, 659, 1404

Toomre, A. 1964, ApJ, 139, 1217

Visser, A. E., Richer, J. S., Chandler, C. J., & Padman, R. 1998, MNRAS, 301, 585

Weidenschilling, S. J. 1977, Ap&SS, 51, 153

Weintraub, D. A., Sandell, G., & Duncan, W. D. 1989, ApJ, 340, L69

Welch, W. J., Thornton, D. D., Plambeck, R. L., Wright, M. C. H., Lugten, J., Urry, L., Fleming, M., Hoffman, W., Hudson, J., Lum, W. T., Forster, J. . R., Thatte, N., Zhang, X., Zivanovic, S., Snyder, L., Crutcher, R., Lo, K. Y., Wakker, B., Stupar, M., Sault, R., Miao, Y., Rao, R., Wan, K., Dickel, H. R., Blitz, L., Vogel, S. N., Mundy, L., Erickson, W., Teuben, P. J., Morgan, J., Helfer, T., Looney, L., de Gues, E., Grossman, A., Howe, J. E., Pound, M., & Regan, M. 1996, PASP, 108, 93

Wilner, D. J., Ho, P. T. P., & Rodriguez, L. F. 1996, ApJ, 470, L117+

Wolf-Chase, G. A., Barsony, M., & O'Linger, J. 2000, AJ, 120, 1467

Wolfire, M. G. & Cassinelli, J. P. 1986, ApJ, 310, 207

Woody, D. P., Beasley, A. J., Bolatto, A. D., Carlstrom, J. E., Harris, A., Hawkins, D. W., Lamb, J., Looney, L., Mundy, L. G., Plambeck, R. L., Scott, S., & Wright, M. 2004, in Presented at the Society of Photo-Optical Instrumentation Engineers (SPIE) Conference, Vol. 5498, Millimeter and Submillimeter Detectors for Astronomy II. Edited by Jonas Zmuidzinas, Wayne S. Holland and Stafford Withington Proceedings of the SPIE, Volume 5498, pp. 30-41 (2004)., ed. C. M. Bradford, P. A. R. Ade, J. E. Aguirre, J. J. Bock, M. Dragovan, L. Duband, L. Earle, J. Glenn, H. Matsuhara, B. J. Naylor, H. T. Nguyen, M. Yun, & J. Zmuidzinas, 30–41

Wu, Y., Wei, Y., Zhao, M., Shi, Y., Yu, W., Qin, S., & Huang, M. 2004, A&A, 426, 503

Yan, H., Lazarian, A., & Draine, B. T. 2004, ApJ, 616, 895